Modelling for Fuel Optimal Control of a Variable Compression Engine

Ylva Nilsson

Linköping 2007

**Modelling for Fuel Optimal Control
of a Variable Compression Engine**

ABSTRACT

Variable compression engines are a mean to meet the demand on lower fuel consumption. A high compression ratio results in high engine efficiency, but also increases the knock tendency. On conventional engines with fixed compression ratio, knock is avoided by retarding the ignition angle. The variable compression engine offers an extra dimension in knock control, since both ignition angle and compression ratio can be adjusted. The central question is thus for what combination of compression ratio and ignition angle the maximum efficiency is achieved, considering the set of compression ratios and ignition angles that give a sufficiently low knock intensity.

Four knock detection methods are proposed, compared and evaluated with respect to robustness for noise and choices of parameter values. Three of the knock detectors are categorised as on-line, and are designed for giving feedback about knock occurrence to the engine control unit. The methods can determine both whether or not knock is present and the crank angle at knock onset.

A study of the relationship between knock oscillation properties and knock-onset is performed. It is concluded that the logarithm of the normalised knock energy depends almost linearly on the rate of knock occurrence.

A new formulation of multi-zone engine models is presented. The formulation makes it easy to increase or decrease the number of zones during the simulation. One of many possible applications is the investigation of engine efficiency.

An analysis of experimental data shows how the engine efficiency changes with compression ratio and ignition angle. An engine torque model is developed and validated, from which the optimal choice of compression ratio and ignition angle can be calculated with high accuracy.

Modellering för bränsleoptimal reglering av en tändstiftsmotor med variabel kompression

Nästan varje dag när vi slår upp morgontidningen möts vi av energirelaterade larmrapporter. Vissa morgnar kan vi läsa att oljeresevoarerna långt nere under jordytan är på väg att sina, men på senare tid har larmrapporterna mest handlat om den globala uppvärmningen. Uppvärmningen förklaras med att det uppstår växthusgaser när vi förbränner fossila bränslen.

En ofta utpekad bov i sammanhanget är personbilen. Under motorhuven finns en bränsleslukande förbränningsmotor som släpper ut avgaser. De senaste decennierna har motorerna blivit allt renare. Emissionsnivåerna i nya bilar under varmkörning är nu lägre än vad vi någonsin hade kunnat drömma om för 20 år sedan—detta tack vara katalysatorn och effektiva regleralgoritmer. Det här gäller dock inte koldioxiden. Koldioxid räknas inte som en emission, och faktum är att ju effektivare en katalysator arbetar desto mera koldioxid bildas det. Det vi kan göra för att minska koldioxidutsläppen är att öka motorernas verkningsgrad eller att byta till ett förnyelsebart bränsle.

Denna avhandling behandlar frågor som rör just förbränningsmotorns effektivitet. Huvudmålet är att finna den kombination av styrsignaler som ger högst verkningsgrad hos en tändstiftsmotor med variabel kompression, men som samtidigt inte orsakar skadligt eller störande motorknack.

Tändning, knack och variabel kompression

En motor får hjulen på bilen att röra sig genom att kolvarna inne i motorn driver på en vevaxel så att den roterar, och eftersom vevaxeln är sammanlänkad med hjulen via växlar och kopplingar påverkas även de. Det som i sin tur får kolven

att röra sig är att det inne i motorcylindrarna förbränns en blandning av bränsle och luft. Den förbrända gasen tar större plats än den oförbrända gasen och kräver därmed större utrymme. Kolven skjuts därför nedåt. Varje arbetscykel består av att ny gas sugs in i cylindern, gasen komprimeras, tändstiftet ger ifrån sig en gnista som antänder gasen, gasen förbränns och pressar ner kolven, avgasventilen öppnas och gasen föses sedan ut av kolven ut i avgasröret.

Gasen i cylindern förbränns inte på en gång, utan det tar en liten stund för flamman att gå från tändstiftet till väggarna. Tändningsregleringens mål är att placera denna tidsperiod i förhållande till kolvens rörelse så att det blir en så effektiv knuff på kolven som möjligt. Den optimala placeringen påminner ganska mycket om när man föser på ett litet barn i en gunga. Förbränningen startar strax innan kolven vänder i sitt övre läge så att den hinner ta ordentlig fart och kan skjuta på kolven med högt tryck på nervägen.

Det gäller dock att trycket inte blir för högt. Blir trycket högt så blir temperaturen också hög, och då kan det hända att en förbränning startar av sig själv bland de ännu oförbrända gaserna. Sker detta går förbränningen i regel så snabbt att det skapas tryckvågor inne i cylindern. Det ljud som då uppstår kallas knack. Knack är något man vill undvika, för ljudet är störande och tryckvågorna kan skada motorn om de är alltför kraftiga. Ett sätt att undvika knack är att tända senare, för då blir trycket inte lika högt i cylindern.

Kompressionsförhållandet är kvoten mellan cylinderns största och minsta volym, dvs förhållandet mellan cylindervolymen i kolvens ändlägen. I de flesta fall gäller att ju högre kompressionsförhållande desto bättre knuff på kolven, eftersom trycket blir högre. Verkningsgraden ökar med andra ord med kompressionsförhållandet. Tyvärr gäller samtidigt att risken för knack ökar. Förutom att vara störande och eventuellt skadligt kan knack göra så att verkningsgraden sjunker, för tryckvågorna ökar energiförlusten via värmeöverföring.

Avhandlingens innehåll och kunskapsbidrag

Avhandlingen består av två delar. Den första delen behandlar knack. Metoder föreslås och undersöks, där syftet med metoderna är att bestämma om, och i så fall när, ett knack uppstod. Den metod av de föreslagna som bedöms som mest lämplig används sedan i en analys av knackuppkomst och egenskaper hos tryckoscillationerna.

Den andra delen av avhandlingen fokuserar på förbränningsmodellering. Beroende på hur tändtidpunkten och kompressionsförhållandet kombineras fås olika verkningsgrad och olika mycket knack. Avhandlingen behandlar hur dessa ska väljas vid olika motorvarvtal och olika krav på motormoment. Utöver detta beskrivs en fysikalisk modell[1] avsedd för att simulera trycket under motorns arbetscykel.

Studierna i avhandlingen baseras på mätningar från en SVC-motor, som vår forskningsgrupp har haft förmånen att få ha i vårt forskningslaboratorium. SVC

---

[1]Med modell avses inte en fysisk modell, utan en matematisk beskrivning.

står för SAAB Variable Compression och är en motor som var mycket omtalad i början av decenniet. Det finns andra motortillverkare som också har konstruerat motorer med variabelt kompressionsförhållande utifrån många olika innovativa lösningar på hur kompressionen ska kunna ändras.

Det kunskapsbidrag som denna avhandling ger är i huvudsak:

- Nya metoder för att upptäcka om och när det knackar.

- Kunskap om egenskaper hos knack, framför allt svaga knack. Det har gjorts många studier på knack och dess egenskaper, men dessa har fokuserat på kraftigare knack. Kunskap om svaga knack är viktigt, eftersom en knackregulator bör reglera mot inget eller så svaga knack att de inte uppfattas genom motorbullret.

- En ny formulering för en termodynamisk modell av motorns arbetscykel. Formuleringen gör det smidigt att simulera det som händer i cylindern och att under simuleringen dela in cylindern och dess omgivning i fler eller färre zoner.

- Kunskap om hur verkningsgraden beror av tändtidpunkten och kompressionsförhållandet, samt dess relation till knackgränsen.

- En motormodell som gör det möjligt att beräkna vilken kombination av tändtidpunkt och kompressionsförhållande som ger högst verkningsgrad under lätta knack.

ACKNOWLEDGEMENTS

First of all, I would like to thank my supervisors Dr. Lars Eriksson and Professor Lars Nielsen for their guidance into the world of science and for many interesting discussions. I would also like to thank them for letting me join the research group of Vehicular Systems at the Department of Electrical Engineering.

Dr. Erik Frisk deserves a place in this acknowledgement for proofreading parts of this thesis, for being my co-author and for answering innumerable questions about LaTeX and other computer problems. But most of all I would like to thank Erik for his friendship, support and encouragement throughout these years.

I would like to thank all of my colleagues at Vehicular Systems for creating a nice research atmosphere and many amusing coffee breaks. Dr. Ingemar Andersson, Dr. Per Andersson, Martin Gunnarsson, Marcus Klein, Per Öberg and many others have contributed to my research by interesting discussions, problem solving by mutual effort and knowledge in the field. I am also very grateful to Martin Gunnarsson for taking good care of our research laboratory. Carolina Fröberg and Susana Högne have always been helpful when it comes to administrative and practical problems, and deserve much gratitude.

I would also like to thank all of my friends. Being a PhD student is not always easy, and your support have been invaluable. I am especially thankful to Johan Andersson and Åsa Sjöblom who are always there when I need them.

Finally, I would like to thank Martin and our daughter Elsa for all their love, support and patience, and most of all for making me happy.

Contents

Control by compression ratio and ignition timing

Cheshire Puss, she began, rather timidly, as she did not at all know whether it would like the name: however, it only grinned a little wider. Come, it's pleased so far, thought Alice, and she went on: Would you tell me, please, which way I ought to go from here?

That depends a good deal on where you want to get to, said the Cat.

I don't much care where—, said Alice.

Then it doesn't matter which way you go, said the Cat.

— so long as I get SOMEWHERE, Alice added as an explanation.

Oh, you're sure to do that, said the Cat, if you only walk long enough. (Carroll, 1865)

The first essential question to ask yourself when aiming to control something is where you want to go, that is: WHAT do you want to accomplish? Then you can ask WHERE you can find it. Finally, you can figure out HOW to get there. The first two questions may seem trivial at first sight, but often comprise many difficult issues. As a matter of fact, these two questions are the subject of this thesis.

There are several different, sometimes conflicting, demands on an internal combustion spark ignited engine used for propulsion. It should be strong, fuel efficient, reliable, produce as low emissions as possible, be as snug that it fits into the very narrow and crowded engine compartment of a car, and have a long life-time. At the same time, it should not become too expensive. The focus in this thesis is on fuel efficiency, and on engine life-time by limiting the knock intensity. The aim to accomplish is thus:

> Finding the combination of compression ratio and ignition angle that gives the highest fuel efficiency, considering the region with sufficiently low knock intensity.

The driver of the automobile expect the vehicle to move at a certain speed, which puts requirements on the output torque from the engine. Another condition is therefore that the output torque should remain constant when the compression ratio and ignition angle is adjusted.

1.1   Why fuel efficiency is important

There are three main reasons why fuel efficiency is important: A limited supply of crude oil, economical reasons, and environmental issues. Petrol comes from crude oil, which is a natural resource with limited supplies. Increasing the efficiency makes the supplies last longer. For the owner of a car, it is of course an advantage if the car consumes less fuel. To travel a certain distance becomes less expensive, and there will be less stops at the petrol stations.

Burning a mixture of petrol and air produces water, carbon dioxide, carbon monoxide, nitrogen oxides, unburned hydrocarbons, ozone, and a range of other kinds of molecules. The increasing use of the three-way catalyst has reduced the concentration of many harmful molecules, but carbon dioxide and water remains. As a paradox, the cleaner the exhaust, the more carbon dioxide is produced. The only way to reduce the amount of carbon dioxide added to the environment by a combustion engine is to either increase the efficiency or to use fuels from renewable sources.

In this thesis, petrol is used in the investigations. However, the same chemical and thermodynamic principles that govern the combustion of petrol are also valid for other hydrocarbon fuels. The differences are for example how easily they ignite, their density and energy contents, and how easily they mix with air.

1.2 Knock in spark-ignited engines

Knock is the name for the sound of an auto-ignition initiated pressure wave inside the engine cylinder. The sound resembles a ping or crackle. It can be observed by the human ear, except for weak knock, and is also visible in e.g. cylinder pressure traces. Knock is something that should be avoided or at least be kept at a very low level. If the knock is severe, it can cause engine failure and even engine break down (Fitton and Nates, 1996). But even when being more modest, the knock can be potentially harmful since it is distracting the driver.

Due to economical and environmental concerns it is desirable to have an internal combustion engine with as high efficiency as possible. However, in many operating points, high efficiency operation increases the top temperature in the cylinder, and thereby the risk of auto-ignition (Stone, 1999).

Knock tendency is reduced by the engine control unit by retarding the ignition angle after a knock has been detected. The ignition angle is then slowly moved back towards its optimum, as long as no new knocks are detected (Kiencke and Nielsen, 2000). Weak knock is not harmful to the engine. If the engine can be controlled towards a harmless knock intensity level instead of zero knock, efficiency can be increased in many cases.

1.3 The variable compression engine

A spark-ignited engine is often said to behave like an ideal Otto cycle. This is of course far from the truth, but it gives a tool for rough estimates. The efficiency of an ideal Otto cycle is

$$\eta = 1 - \frac{1}{r_{\mathrm{c}}^{1-\gamma}} \tag{1.1}$$

where r_c is the compression ratio and γ the ratio between specific heats. This means that the higher the compression, the higher the efficiency. The maximum efficiency is thus achieved at an infinite compression ratio. In a real engine cycle, energy is lost to heat transfer. The rate of heat transfer increases with compression, and therefore the maximum efficiency is found at a limited compression ratio. Caris and Nelson (1959), cited in Blackmore and Thomas (1977), found that increasing the compression ratio above 16:1 or 17:1 causes a decrease in engine efficiency.

A problem with a high compression ratio is that raising the compression leads to higher peak temperatures and pressures during the engine cycle. The risk of knock is thereby increased. Because of this, conventional spark ignited engines often have a compression ratio around $r_{\mathrm{c}} = 10$, even though low and modest inlet pressures allows higher compression. A variable compression ratio makes it possible to increase the overall engine efficiency, by choosing high compression ratios at low loads to maximise the efficiency, and low compression ratios at high loads to avoid knock.

The benefit of having a variable compression ratio is more significant combined with the concept of downsizing. By keeping the engine small, pump losses and friction are reduced (Soltic, 2000). The drawback is that the engine is less powerful, since the displaced volume is smaller. This is solved by adding a supercharger, that increases the density of the air-fuel mixture when needed, thereby allowing for more fuel to be injected each cycle. But since the inlet manifold pressure is increased, the knock tendency is also increased. If the super-charged engine lacks the possibility to change the compression, it will therefore need to have a even lower compression ratio than a naturally aspirated.

Maybe the most famous variable compression engine is the SVC engine, shown in Figure 1.1. The name stands for SAAB Variable Compression engine. The engine is a down-sized super-charged variable compression engine of 1.6 litre and maximum 305 Nm (SAAB Automobile AB, 2000).

The idea behind the SVC engine is to make the size of the clearance volume variable. Thereby the compression ratio r_c is changed, as

$$r_c = \frac{V_{\text{max}}}{V_{\text{min}}} = \frac{V_{\text{disp}} + V_{\text{clear}}}{V_{\text{clear}}}$$

The size of the clearance volume is increased by tilting the mono-head, which consists of the cylinders and cylinder head. The mono-head is tilted relative to the crank case and the cylinder head is thereby moved away from the crankshaft. The consequence is that the piston does not reach as close to the cylinder head at TDC as it had done in upright position, which leaves a greater clearance volume (Drangel and Reinmann, 2002). The tilting of the engine top has consequences for the calculation of cylinder volume as function of crank angle, as well as the position of top dead centre (TDC). This will be analysed in Appendix A.

1.3.1   Other VCR engine concepts

The measurements in this thesis is from an SVC engine, but there exist several other VCR engine concepts. Following are examples of some categories of VCR engines:

Secondary piston The combustion chamber has a small secondary piston that is used to change the compression ratio. On an Alvar engine, the secondary piston moves continuously at half crankshaft speed. The compression ratio depends on the phase shift between the primary and secondary piston (Erlandsson et al., 1998). On a Ford VCR engine, the piston is directly connected to a controller. When the engine runs at high loads, the piston is recessed to allow a greater clearance volume (Clarke and Tabaczynski, 2000).

Con rod linkages The conventional con rod is replaced with a 2 piece design in which an upper member connects with the piston while a lower member connects with the crankshaft. By constraining the freedom of the point

Figure 1.1: The SVC engine.

at which the two members join, the effective height of the con rod can be controlled and thereby the compression ratio. The concept is investigated in Moteki et al. (2003), and the patents Bollig et al. (1997) and Ma (1998) are for such VCR engines.

Another example of an engine in this category is the MCE-5 engine. The engine is shown in Figure 1.2, and its operating principle is illustrated in Figure 1.3. The motion of the piston is guided by a synchronised roller and a gear-wheel, thereby reducing the side-thrust on the piston to a minimum. The compression ratio depends on the position of the control-rack. The compression ratio can be controlled individually for the different cylinders (MCE-5, 2004).
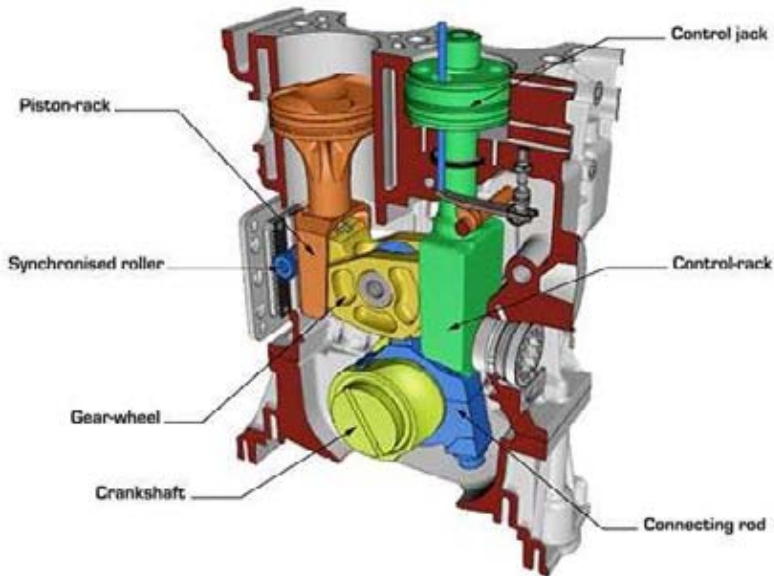
Figure 1.2: The MCE-5 engine concept. The picture is from the MCE-5 engine homepage at http://www.mce-5.fr. Printed with permission from MCE-5 Development SA.

Movement of crankshaft or crank-pins The crankshaft position is moved with respect to the cylinder head, or the crank-pins are moved eccentrically. An example is the GoEngine, shown in Figure 1.4. The GoEngine has an eccentric between the crankpin and the big end of each con-rod. This eccentric is driven in a specific path by a gear. With the crank in bottom dead centre position, the eccentric will be on the lower side of the crankpin giving an increased expansion stroke or on the higher side of the crankpin giving a reduced intake stroke. This means that, beside
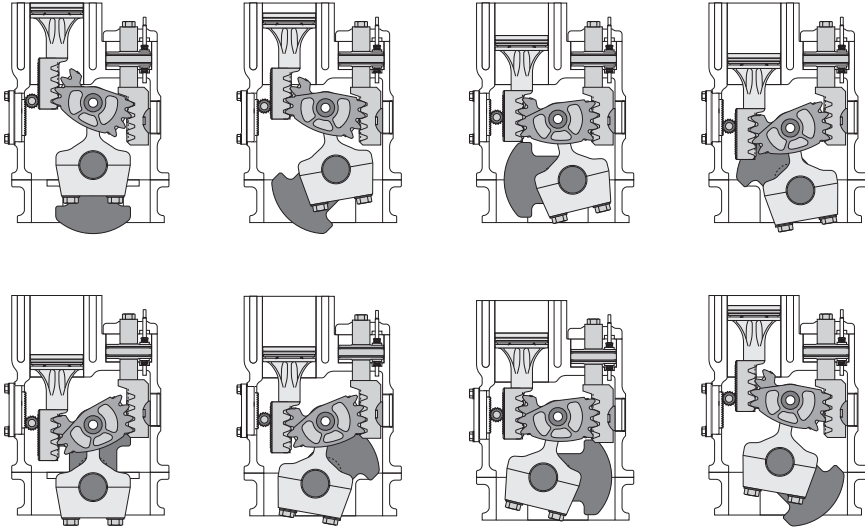
Figure 1.3: Operating principle of the MCE-5 engine. The illustration is from the MCE-5 engine homepage at http://www.mce-5.fr. Printed with permission from MCE-5 Development SA.

the advantage of having a variable compression ratio, the engine operates according to the more efficient Atkinson cycle than the Otto cycle.

Variable piston height The compression ratio can be increased by increasing the height of the piston. If the top of the piston head is not fixed to the rest of the piston, the height of the piston can be controlled by the supply of engine lubrication oil. Ford and Daimler-Benz have proposed VCR engines in this category (Roberts, 2003).

Variable valve timing The main purpose of using variable valve timing is not to change the compression ratio, but to decrease the pumping losses at part load; see for example Kreuter et al. (1998). However, a side effect of varying the crank angle at inlet valve closing and/or exhaust valve opening, is that the effective compression ratio also changes.

1.4 Fuel optimal control of a variable compression engine

We now turn back to the central question of this work. During driving the engine speed is given by the vehicle speed and gear ratio, and the driver requests a desired engine torque M_{des}, that is used to achieve the desired vehicle speed.
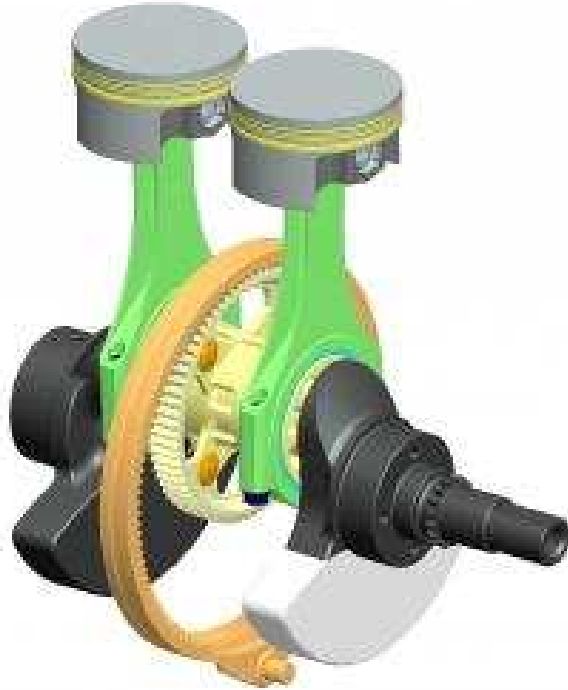
Figure 1.4: The GoEngine concept. The picture is from the GoEngine homepage at http://www.gomecsys.com. Printed with permission from Gomecsys BV.

The controller then has to select the air mass flow $\dot{m}_{\mathrm{air}}$, fuel mass flow $\dot{m}_{\mathrm{fuel}}$, ignition timing θ_{ign}, and compression ratio r_{c}, that fulfils the desired torque requirement for the current conditions. Strictly speaking, the control signal is not the air mass flow but the throttle angle. However, the air mass controller is assumed to be fully operative and its behaviour is not taken into account.

Beside the requested engine torque there are two additional requirements: Firstly, the knock intensity should be kept low to ensure that there is no distressing or harmful knock. Secondly, the engine is equipped with a three way catalyst and should therefore always be run with stoichiometric air/fuel ratio. This is expressed as $\lambda = \frac{\dot{m}_{\mathrm{air}}}{\dot{m}_{\mathrm{fuel}}}/(A/F)_{\mathrm{S}} = 1$, where λ is the normalised air/fuel ratio and $(A/F)_{\mathrm{S}}$ is the stoichiometric air/fuel ratio. There are many possible choices of control signals that fulfils the requirements. The engine control unit should choose the combination that results in the highest engine efficiency η, since this minimises the fuel consumption. The resulting optimisation problem

can be written

$$\mathbf{x} = \underset{r_c, \theta_{ign}, \dot{m}_{air}, \dot{m}_{fuel}}{\arg\max} \quad \eta(r_c, \theta_{ign}, \dot{m}_{air}, \dot{m}_{fuel})$$

$$\text{subject to} \left\{ \begin{array}{l} M(r_c, \theta_{ign}, \dot{m}_{air}, \dot{m}_{fuel}) = M_{des} \\ I_{knock}(r_c, \theta_{ign}, \dot{m}_{air}, \dot{m}_{fuel}) \leq I_{limit} \\ \frac{\dot{m}_{air}}{\dot{m}_{fuel}} = (A/F)_S \end{array} \right. \tag{1.2}$$

where the I_{limit} defines the highest allowed knock intensity.

1.4.1 A closer look at the optimisation problem

As a first step it is beneficial to eliminate the air/fuel ratio constraint, which couples the fuel mass flow $\dot{m}_{fuel}$ directly to the air mass flow $\dot{m}_{air}$. It is eliminated from the optimisation by substitution, i.e. the fuel mass flow is directly substituted by the following $\dot{m}_{fuel} = \dot{m}_{air}/(A/F)_S$. This reduces the number of free variables to three.

In the next step the engine efficiency is studied. It is defined as the ratio between the produced work and the supplied energy:

$$\eta = \frac{W}{Q_{supplied}} = \frac{2\pi n_r \, M}{q_{HV} \, m_{fuel}} \tag{1.3}$$

where q_{HV} is the heating value of the fuel, and n_r the number of crank revolutions per engine cycle. The fuel injected during an engine cycle is

$$m_{fuel} = \frac{n_r}{N} \cdot \dot{m}_{fuel} = \frac{n_r}{N} \cdot \frac{1}{(A/F)_s} \cdot \dot{m}_{air} \tag{1.4}$$

That is, the supplied energy is proportional to the air mass flow, and independent of compression ratio and ignition angle. This can be expressed as:

$$Q_{supplied} = f(N, \lambda) \cdot \dot{m}_{air}$$

where $f(N, \lambda) > 0$. As a consequence of the constraint on the torque in (1.2), the numerator of (1.3) should remain constant during changes in the control signals. It can thus be concluded that the following optimisation problem

$$\mathbf{x} = \underset{\dot{m}_{air}, r_c, \theta_{ign}}{\arg\min} \quad \dot{m}_{air}$$

$$\text{subject to} \left\{ \begin{array}{l} M(r_c, \theta_{ign}, \dot{m}_{air}) = M_{des} \\ I_{knock}(r_c, \theta_{ign}, \dot{m}_{air}) \leq I_{limit} \end{array} \right. \tag{1.5}$$

has the same solution as (1.2), and is a simpler problem to solve. This formulation is also natural since the maximum efficiency corresponds to minimum air and fuel consumption.

Due to that the engine torque increases with increasing air mass flow, the compression ratio and ignition angle should be chosen such that the torque

increases as much as possible, since this allows the greatest reduction in air mass flow. In other words, if $\widehat{\dot{m}_{\text{air}}}$ is the solution to (1.5) for the air mass flow, the compression ratio $\widehat{r_{\text{c}}}$ and ignition angle $\widehat{\theta_{\text{ign}}}$ that solves (1.5) will also fulfil

$$
\begin{aligned}
\{\widehat{r_{\text{c}}}, \widehat{\theta_{\text{ign}}}\} =& \arg\max_{r_{\text{c}}, \theta_{\text{ign}}} M(r_{\text{c}}, \theta_{\text{ign}}, \widehat{\dot{m}_{\text{air}}}) \\
& \text{subject to } I_{\text{knock}}(r_{\text{c}}, \theta_{\text{ign}}, \widehat{\dot{m}_{\text{air}}}) \leq I_{\text{limit}}
\end{aligned}
\tag{1.6}
$$

The condition on the knock intensity divides the sets of $\{r_{\text{c}}, \theta_{\text{ign}}\}$ in two; a feasible and a non-feasible region. If the maximum efficiency is found in the feasible region, these coordinates are also the solution to (1.2). But if the maximum efficiency is in the non-feasible region, the solution is found on the border between the two regions, assuming that $\eta(r_{\text{c}}, \theta_{\text{ign}})$ is smooth and concave. The optimisation problem is illustrated in Figure 1.5.

The formulation (1.6) shows that the central components for fuel optimal control of a variable compression engine are the knocking limitation and the torque model. Accordingly the main themes of this thesis is the determination of the knock intensity, which is the subject of the first part, and modelling of the engine torque which is the subject of the second part.
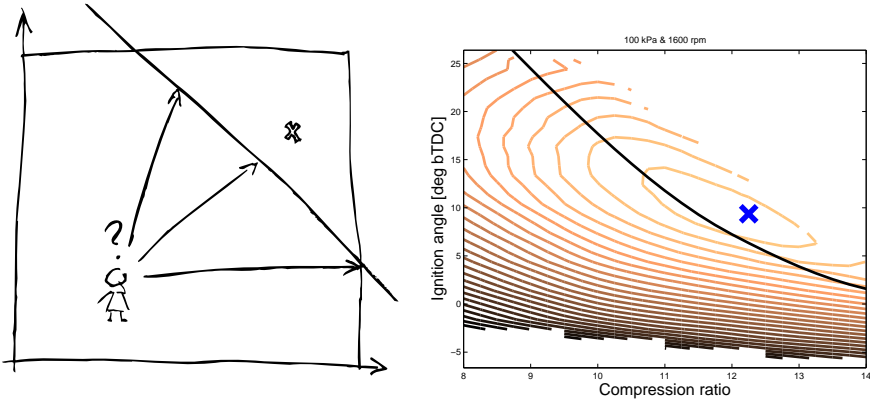
Figure 1.5: The fuel optimal combination of compression ratio and ignition angle is in the non-feasible region. This transforms the problem into finding the optimal combination $\{r_{\text{c}}, \theta_{\text{ign}}\}$ on the border between the regions. In the right-most figure is shown engine efficiency contours and the knock intensity limit based on measurements from the SVC engine. The dark solid line is the knock intensity limit that should not be trespassed.

1.5 Limitations and assumptions

From here on, the word *engine* is used for a spark ignited (SI) engine run on petrol. The investigations are based on measurements from an SVC engine and the measurement set-up and measured data sets are described in Appendix B.

Experimental equipment is precious for projects that run over long periods of time. In particular the SVC engine is a rare prototype, and to ensure the necessary long term fault-free operation the allowed engine speeds were limited to the range from 1200 to 3000 rpm. The lower limit of 1200 rpm was chosen due to that the engine had an irregular run for lower speeds. Recommendations were given from SAAB that the engine should not be run during long periods above 3500 rpm. As a consequence 3000 rpm was chosen as upper limit, leaving a small safety margin.

There are many questions that have to be answered if the aim is to make up a complete engine management system with control of compression ratio, ignition timing, air, and fuel. Covering all necessary issues is not possible within a thesis. Therefore this thesis focuses its attention on the engine operating range where the engine control system has to control both the compression ratio and spark timing to achieve the lowest fuel consumption. Examples of other interesting topics are: At low loads, where the optimal choice of compression ratio is the maximum possible irrespectively of ignition angle, a conventional maximum brake torque controller can be used. At very high loads, where the knock intensity forces the choice of compression ratio to its minimum, the controller may be obliged to use air/fuel ratio as an additional control signal. The same is the case for speed and load points where the high temperature of the exhaust gases dangers the catalyst. However these are not the topics of this thesis.

1.6 Outline

Four methods for knock detection are presented in Chapter 2. Three of these are categorised as on-line methods, and can be used by an engine control unit to continuously monitor occurrence of knock. The chapter is based on Nilsson and Frisk (2005).

The relationships between signal properties of the knock trace and knock occurrence are investigated in Chapter 3. The motive for this study is to see how the outcome of knock models that predict the angle at knock-onset should be translated into knock intensity, which is a measure used by knock controllers.

A new formulation of multi-zone engine models is presented in Chapter 4. The formulation makes it easy to increase or decrease the number of zones during the simulation. One of many possible applications is simulations of engine efficiency. The chapter is a revised version of Nilsson and Eriksson (2001).

Chapter 5 contains an investigation of how the engine torque is affected by the choice of compression ratio and ignition angle. A torque model is developed, with which the fuel optimal choice of compression ratio and ignition angle can

be determined. The chapter is a combined version of the publications Nilsson et al. (2008), Nilsson et al. (2006b), and Nilsson et al. (2006a).

The unconventional geometry of the SVC engine makes it necessary to derive a new expression for the volume. This is done in Appendix A. Beside giving the volume for the SVC engine, the function also describes conventional engines with piston pin offset. The chapter is a revised version of Nilsson (2001). The result have also been used in Klein et al. (2003).

The measurement set-up and measured data sets are described in Appendix B.

1.7   Contributions

- New knock detection methods are proposed and evaluated on cylinder pressure. The knock detectors are capable of both determining whether or not knock is present and estimating the angle at knock-onset.

- Knowledge about knock characteristics in the intensity region that is interesting for knock control. Many cycles in this region show signs of multiple knock-onset and/or a gradual build-up in knock intensity.

- Knowledge about the relation between the occurrence of knock and the intensity of the knock oscillations. The results show that there is an almost linear relation between the rate of (detected) knock occurrence and the logarithm of the normalised knock energy.

- A new formulation of a multi-zone combustion engine models. The underlying structure of the model is not new in itself—it is the formulation that is new. The formulation makes it easy to add new zones and remove zones that are not needed any longer. The formulation has already been successfully used for various applications in a number of scientific works.

- Analysis of experimental data from a variable compression engine, where engine maps show how the gross indicated work and the overall engine efficiency depends on compression ratio and ignition angle.

- A torque model for a variable compression engine. The model is developed and validated on experimental data.

Part I

Engine knock

Detection of knock and knock-onset
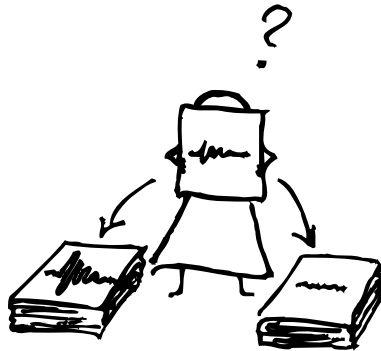
This is an extended version of Detecting knock in Spark ignited engines (Nilsson and Frisk, 2005).

There are many published algorithms for knock detection. However, their main focus is on determining whether a knock is present or not, not on the identification of crank angle at knock onset. Four different knock detection methods are therefore here presented. The aim of these algorithms are both on detecting knock at intensities just above borderline knock, as well as determining the crank angle at knock onset with high accuracy.

The four methods are divided into two groups. One method is computationally demanding, and therefore categorised as an off-line method. The other three methods are classified as on-line methods. The off-line method is based on a knock signal model consisting of damped oscillations with constant frequency. One of the on-line methods is a simplification of this method, where the oscillation amplitude is set constant. The two remaining methods detect changes in signal variance. The methods capability to detect knock and estimate the time of knock onset are evaluated on measured cylinder pressure signals. The robustness to changes in the noise variance and parameter values are also investigated.

A problem arises in the evaluation. To be able to estimate the accuracy of the methods, the true knock onset must be known. Visual inspection of cylinder pressure traces highlights that it is in many cases a question of definition at what time instant the knock is initiated, and at borderline knock intensities it is difficult to judge whether knock is present or if there are some disturbances. The deviation of the measured knock traces from the ideal knock signal model is here illustrated and discussed.

2.1   Engine knock

It is generally agreed upon that knock originates in the extremely rapid release of much of the energy contained in the end-gas ahead of the propagating turbulent flame, resulting in high local pressures (Heywood, 1988). There are two main explanations to knock origin: The auto-ignition theory and the detonation theory. Both these theories are valid, since these phenomena interact, and also because auto-ignition is a precondition for detonation initiation (Gogan, 2002).

2.1.1   Detonation theory

In some cases, the origin of the knock oscillation is a shock wave caused by detonation. Glassman (1996) explains detonation as follows:

> The burned gas products from the initial deflagration have a specific volume of the order of 5–15 times that of the unburned gases ahead of the flame. Since each preceding compression wave that results from this expansion tends to heat the unburned gas mixture somewhat, the sound velocity increases and the succeeding waves catch up with the initial one. Furthermore, the preheating tends to

increase the flame speed, which then accelerates the unburned gas mixture even further to a point where turbulence is developed in the unburned gases. Then, a still greater velocity and acceleration of the unburned gases and compression waves are obtained. This sequence of events forms a shock that is strong enough to ignite the gas mixture ahead of the front. The reaction zone behind the shock sends forth a continuous compression wave that keeps the shock front from decaying, and so a detonation is obtained.

2.1.2 Auto-ignition theory

Knock is initiated by the rapid burn of fuel after auto-ignition. Since an amount of fuel is combusted almost momentarily, the pressure in the cylinder becomes inhomogeneous and a pressure wave is thereby created. The pressure wave is the source of the characteristic sound that is called knock. Three main principles governs the occurrence of knock:

Chemical equilibrium The chemical equilibrium governs the direction at which a reaction occurs. The composition at chemical equilibrium depends on temperature and pressure (Finn, 1998).

Activation energy Even if a gas is not in equilibrium, there may not be any reactions. This can be the case even when the reaction path is exothermic, that is when more energy is released than consumed in the reactions. A gas consisting of a stoichiometric mixture of iso-heptane and oxygen, produces carbon dioxide, water and excess energy when combusted:

$$C_7H_{16} + 11\,O_2 \rightarrow 7\,CO_2 + 8\,H_2O + \text{energy} \qquad (2.1)$$
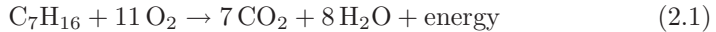
But hidden in the expression (2.1) are the many steps of the total reaction path. To get from the reactants to the final products an energy barrier has to be overcome, see Figure 2.1. The barrier is called the activation energy E_a (Atkins, 2000). Therefore, even though the chemical equilibrium at room temperature and pressure favours the right side of (2.1), the combustion does not start until extra energy is added to the molecules. This can be achieved by a spark from a spark plug. The spark increases the energy locally, but the energy released by the combustion of the first molecules is enough to initiate the combustion of other molecules in the neighbourhood. In this way, a flame front is created that travels from the spark plug to the walls.

Energy can also be added to the molecules by adiabatically compressing the gas, and thereby raising the temperature. This is a side effect of the combustion in an engine cylinder. The combustion products demand greater space, and the molecules of the unburned zone, called the end-gas, are thus compressed and the temperature is increased. Ignition created in this way is called auto-ignition. The unburned fuel is combusted rapidly after an auto-ignition, since
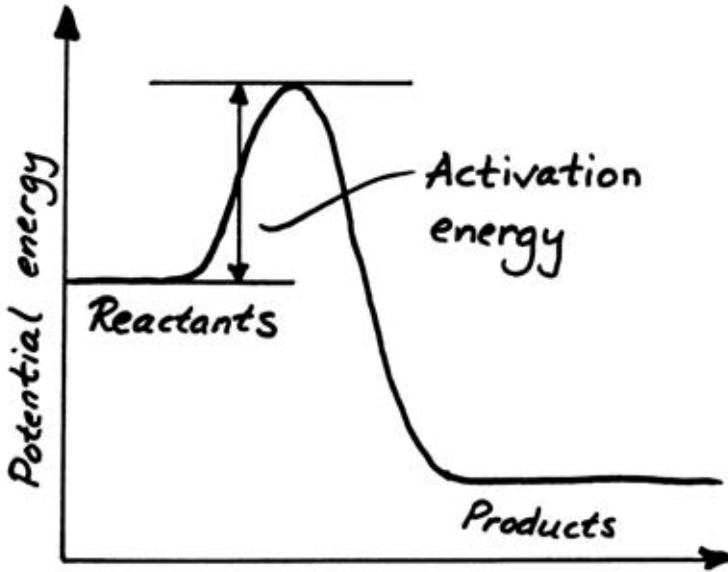
Figure 2.1: Phases of a chemical reaction.

the molecules in the neighbourhood also have received energy in the compression.

Reaction rates   Even though there is enough energy to cross the energy barrier, the gas may not be in chemical equilibrium. It takes some time for the reactions to occur. The reaction speed increases with temperature, pressure, and concentration. For the reaction

$$A + B \rightarrow C \tag{2.2}$$

the reaction rate is

$$-\frac{d[A]}{dt} = -\frac{d[B]}{dt} = \frac{d[C]}{dt} = k_{rr}[A][B] \tag{2.3}$$

where $[\cdot]$ denotes the concentration of a molecule, and k_{rr} the reaction rate constant. The rate constant is determined by the Arrhenius equation

$$k_{rr} = A_{rr}e^{-E_a/\tilde{R}T} \tag{2.4}$$

The factor A_{rr} is the constant of proportionality between the concentrations of the reactants and the rate at which the reactant molecules collide (Atkins, 2000).
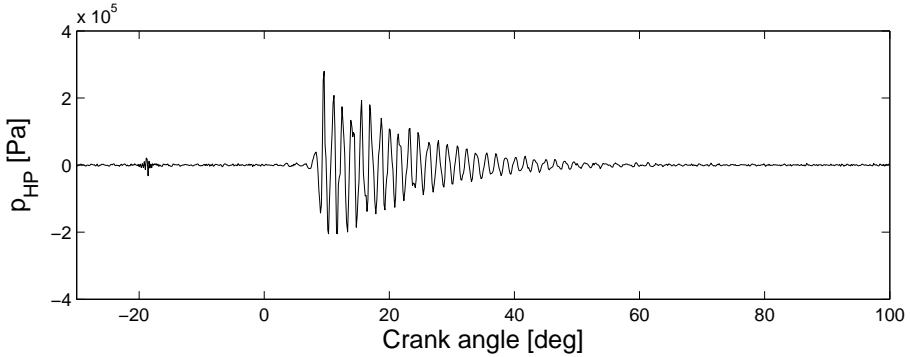
Figure 2.2: High pass filtered cylinder pressure. The knock induced oscillation is clearly visible.

From this can be understood that to cause auto-ignition, high temperature during sufficiently long time is needed. The knock intensity increases with inlet manifold pressure, compression and charge temperature, but decreases with engine speed. Knock is most likely to occur in the part of the engine cycle with the highest pressure. Under normal conditions, auto-ignition arises after the spark is delivered from the spark-plug, and before all the gas has been combusted. If there is auto-ignition even though there is no spark, it is called run-away knock (Stone, 1999). It is a very harmful condition, and is not considered here since the knock control should aim at far lower knock intensities.

2.1.3   Knock signature

Ideally, the rapid burning of fuel that initiates knock has the same effect on the cylinder pressure as hitting a drum has on the drumhead. An impulse caused by the instantaneous combustion, is followed by a damped oscillation. The oscillation is visible in the cylinder pressure, as shown in Figure 2.2.

The frequency of the oscillation is determined by the geometry of the combustion chamber, where the fundamental oscillatory mode is a wave travelling from one side of the combustion chamber to the opposite side (Carstens-Behrens et al., 2002). Using a well tuned high pass filter, the oscillating knock signal can then be detected. Depending on the placement of the sensor, it is sometimes easier to observe the harmonics than the fundamental mode (Sawamoto et al., 1987). This is often the case when the cylinder pressure sensor is combined with the spark plug.

The wave travels with the speed of sound c, that is

$$c = \sqrt{\frac{\gamma R T}{M}} \qquad (2.5)$$

where γ is the ratio between specific heats, R the universal gas constant, T cylinder gas temperature, and M molar weight. The knock frequency can be calculated from the Bessel number (Blunsdon and Dent, 1994) and (2.5). For the SVC engine, the frequency is approximately 8 kHz. The frequency changes noticeably during the oscillation (Härle and Böhme, 1987). For the pressure signal shown in Figure 2.2, it changes from approximately 7920 Hz in the region $\theta \in [9°, 28°]$ to 7440 Hz in the region $\theta \in [35°, 65°]$ which is a reduction of 6%.

2.2   Knock detection methods and sensors

A lot of time and effort has been put into finding efficient knock detection methods throughout the years. Burgdorf and Denbratt (1997) outlines some of the methods and evaluates them on cylinder pressure. These methods can be divided into two different groups: Time based and frequency based methods. In most of the time-based methods the cylinder pressure is filtered through a high-pass or band-pass filter before any further calculation steps are applied to it. In that way the oscillations are distinguished. One example is the method *Maximum amplitude of the filtered pressure* (Gao et al., 1993). The maximum amplitude of the filtered pressure is denoted the knock intensity and is used as the test quantity in the detection. A variation of this method is to take the difference between the maximum and minimum filtered pressure (Dimpelfield and Foster, 1984). The knock intensity can also be defined as the integral of the squared filtered cylinder pressure, which is the average signal energy. In *Integral of the bandpass filtered pressure* (Arrigoni et al., 1972; Leppard, 1982), the integration is over the whole length of the knock trace, while in *KI20* (König and Sheppard, 1990) only the first 20 degrees after knock onset is included. After auto-ignition some amount of end-gas is burned almost momentarily, which causes a pressure increase superimposed on the normal pressure curve. Some methods use this for knock detection. Two examples are *Peak rates of pressure rise*, which uses the 1st derivative (Barton et al., 1970; Lyon, 1986; Cowart et al., 1990; Valtadoros et al., 1991), and *Third time derivative of the cylinder pressure signal* (Checkel and Dale, 1986, 1989). The other group of detection methods, the frequency based, contains methods that uses Discrete Fourier Transform for estimating the energy contained in a band around the knock frequency, and time-frequency methods that uses wavelets to also capture the variations in knock frequency (Burgdorf and Karlström, 1997; Strang and Nguyen, 1996).

There are several other time-based methods than the ones investigated in Burgdorf and Denbratt (1997). Brecq et al. (2003) uses the ratio between modulus of pressure oscillation and maximum amplitude of pressure. The auto-ignition gives rise to a superimposed pressure increase, and this in turn effects the heat release trace. The knock test quantity in the method by Corti and Moro (2007) is based on this sudden increase in burn rate. Also Worret et al. (2002) uses the heat release for knock detection, but in a totally different way. The heat release trace is high-pass filtered to isolate the oscillations, which are

also visible in the heat release since it is estimated from the cylinder pressure. It was found that high-pass filtered heat release has a better signal to noise ratio than high-pass filtered cylinder pressure. More work has also been done in the area of knock detection in frequency or time-frequency domain. Some examples are the works by Carstens-Behrens and Bohme (2001), Samimy and Rizzoni (1996), and Lazarescu et al. (2005).

In recent years many researchers have been focusing on knock detection based on the signal from a cylinder pressure sensor. But in an ordinary production engine of today there is no such sensor. Instead, it is common to use an accelerometer that is mounted on the engine block. The pressure oscillation causes the engine block to vibrate, and this oscillation is captured by the accelerometer. An alternative way to observe knock is by measuring the ion current. The pressure fluctuations effect the density of the ions, causing the ion current trace to oscillate with the same frequency as the cylinder pressure (Auzins et al., 1995; Kinoshita et al., 2000). Other kinds of knock sensors have been suggested and evaluated. Excluding highly advanced equipment like photo-optical techniques that will probably never be used on a production engine, there are still some other possibilities. The light intensity and colour can be observed via an optical fibre (Kiencke and Nielsen, 2000), and the increased amount of heat transfer at knock can be detected by supervision of the coolant temperature (Loubar et al., 2005).

2.3 Investigated knock detection methods

As the previous section shows, there are already many methods to chose between for knock detection. But the main focus for the methods above are on judging whether a cycle contains knock or not, and not on the estimation of angle at knock onset. The common way to determine the angle at knock-onset is by directly comparing the high-pass filtered cylinder pressure with a threshold, where the knock angle is defined as the angle at which the signal exceeds the threshold for the first time. Looking through a number of borderline knock makes it obvious that this test quantity is not a good choice since an electrical or mechanical disturbance may be misinterpreted as the knock onset (see for example Figure 2.12). The method by Worret et al. (2002) stands out from the rest of the methods in the previous section, in that it has a thorough way of determining knock onset. This method is not investigated here due to its use of the time derivative of the pressure signal in the heat release calculation. This is not desirable since differentiating a noisy measured signal amplifies its high frequency noise components.

2.3.1 Overview of the methods

Four different knock detection methods, all defined in the time domain, are here proposed and evaluated. The aim of the four methods is to detect knock as well

as to identify the crank angle at knock onset. The methods put requirements
on both intensity and time extension of the oscillation to avoid being deluded
by short disturbances.

Three of the methods are classified as on-line methods and one as off-line.
Normally, on-line requires a casual filter, which means that at time t only sam-
ples $t - k$, $k \geq 0$ are to be used. But since the cylinder pressure data is divided
in sequences of 2 crank angle revolutions length, future time samples can be
used as long as it is in the same sequence. What distinguishes these on-line
methods from the off-line method is that they do not demand any major calcu-
lation effort, and they are therefore expected to be possible to use in an engine
control unit.

The off-line (OFF) method is based on a model of the ideal knock signature,
described in Section 2.1.3. The model takes the signal amplitude and damping
into consideration, but not the frequency shifts. As discussed in section 2.1.3,
the knock frequency changes noticeable during the same oscillation, and it may
therefore seem natural to include variable frequency in the model. However,
the shift in frequency is modest, and it will be evident in the evaluation that
follows that the method suffers more severely of other discrepancies from the
ideal knock signature. Introducing variable frequency would make the method
even more computationally demanding and is therefore avoided.

The first on-line method (ONI) is based on the change in signal variance
after knock-onset. The signal variance is estimated with recursive least square,
and if it changes fast at some time instant, knock is detected. The second
method (ONII) is a simplification of the off-line method. Finally, the third on-
line method (ONIII) uses the signal energy in a time window as detection test
quantity. There are clear resemblances between ONI and ONIII. Both methods
are based on an estimate of the signal variance, as the cylinder pressure is first
passed through a high-pass filter. An important difference is that knock is
detected by ONI only if the signal variance changes sufficiently fast, while there
is no such time aspect in ONIII.

2.3.2   Algorithm components

The design and calibration of the detection methods include the following com-
ponents:

HP filter   The cylinder pressure is first filtered through a zero-phase high pass
filter. The filter is a 4:th order butterworth filter. The cut-off frequency is set
to 6 kHz, since the frequency of the fundamental mode is approximately 8 kHz.

Test quantity   The core of the algorithms are test quantities that are com-
pared with thresholds to determine whether there is knock or not, and at what
crank angle knock is initiated. The test quantities are presented in Section 2.3.3–
2.3.6.
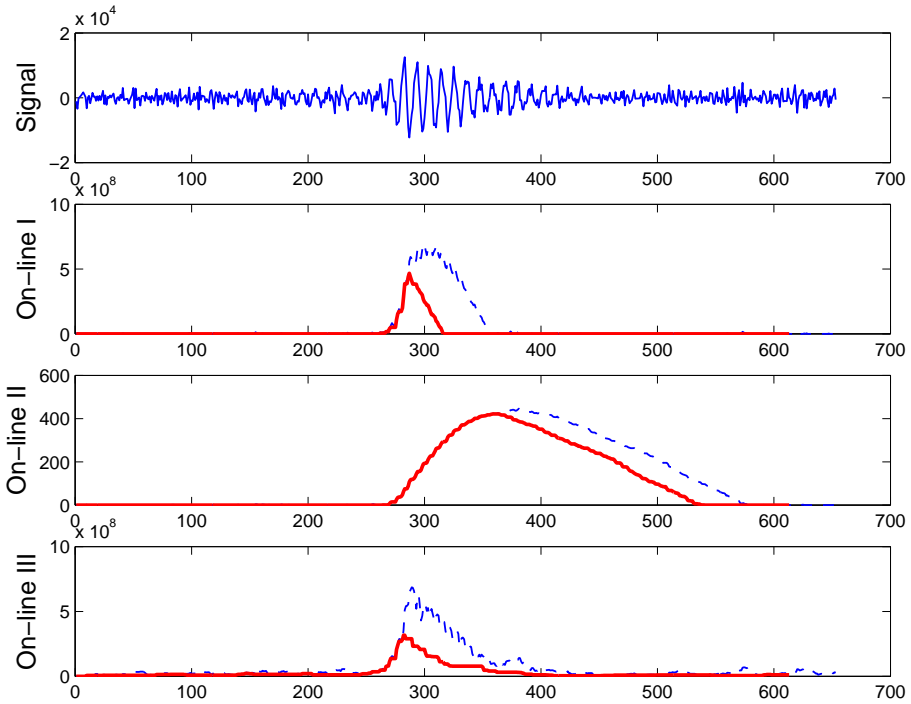
Figure 2.3: Top figure shows the high pass filtered cylinder pressure trace for a cycle with knock. The remaining three figures show the on-line test quantities applied to the same knock trace. The dashed line is the test quantity g and the thick line the effective test quantity g_e.

Requirement on time extension   To avoid the risk that a short, but strong, disturbance causes the tests to alarm, an additional requirement on the alarm is added. Knock is said to be present only if the test quantity g is higher than the threshold for at least 40 samples in succession, corresponding to approximately 4 periods of the fundamental mode. The *effective test quantity* is thus defined as

$$g_e(t) = \min\{g(t), \ldots, g(t+40)\} \tag{2.6}$$

see Figure 2.3. Pressure traces with short disturbances were used to determine that 40 samples is a proper value of the time extension. The choice is based on the observation that the strongest disturbances in the measured data set remained visible in the test quantities for less than 40 samples.

The time extension requirement is only put on the on-line methods, since the off-line method is based on a point-estimate.

Test quantity parameters The on-line test quantities contain parameters and these are chosen in Section 2.3.7. All the test quantities, except ONIII, include the noise level. The noise level is determined individually for each operating point in Section 2.4.

Thresholds Values of the thresholds are chosen in Section 2.3.8.

In the methods below the following nomenclature is used: y denotes HP filtered cylinder pressure, σ_{noise} the noise level of the operating point, h the threshold, t_{det} the time instant at which knock is detected, and t_{knock} the estimated time of knock-onset.

2.3.3   Off-line test quantity (OFF)

Ideally, the knock signature consists of a damped oscillation and white Gaussian noise. The amplitude of the oscillation changes from cycle to cycle, and the damping is also unknown. The off-line method uses a statistical method to estimate the time of knock-onset, by simultaneously determining the most likely initial oscillation amplitude, damping, and time instant at which the oscillation starts.

The signal model for the ideal knock signature in y is assumed to be the impulse response of a second order linear system with complex poles within the unit circle. Let $\alpha = (t_{\mathrm{knock}}, A, r)$ be a vector of the signal parameters where r is the damping coefficient, A the maximum amplitude of the knock, and t_{knock} is the time of knock onset. The ideal knock signature is then

$$\xi(t; \alpha) = A r^{t-2-t_{\mathrm{knock}}} \sin(\Omega(t - 1 - t_{\mathrm{knock}})) h(t - 1 - t_{\mathrm{knock}}) \qquad (2.7)$$

where Ω is the normalised frequency and $h(t)$ the unit step function. The model for the measured signal is

$$y(t) = \xi(t; \alpha) + e(t) \qquad (2.8)$$

where $e(t)$ is an independent sequence of $N(0, \sigma_{\mathrm{noise}}^2)$ distributed, uncorrelated, stochastic variables.

The knock detection test based on L data samples can then be stated as an hypothesis test where the null hypothesis is that no knock occurs within the L data samples, i.e. that $t_{\mathrm{knock}} > L$. Each instantiation of the parameter vector α corresponds to a specific knock trace. The set of all traces without knock is characterised by the set

$$\Theta_0 = \{(t_{\mathrm{knock}}, A, r) : t_{\mathrm{knock}} > L\}$$

With this notation, the hypothesis test can formally be written as

$$H_0: \ \alpha \in \Theta_0 \qquad (2.9a)$$
$$H_1: \ \alpha \in \Theta_0^c = \Theta_1 \qquad (2.9b)$$

If hypothesis H_1 were simple, i.e. Θ_1 consisted of a single element, the Neyman-Pearson Lemma states that the likelihood ratio is a uniformly optimal detector (Casella and Berger, 1990). In this case, where H_1 is not a simple hypothesis, it is therefore natural (Basseville and Nikiforov, 1993) to compute a test based on the window-limited maximum-likelihood ratio

$$g = \max_{\alpha \in \Theta_1} \ln \frac{P_\alpha(y)}{P_{\alpha_0}(y)}$$

where α_0 corresponds to no knock conditions. Such a detector has some asymptotic optimality properties, see for example Lai (1995) and Lorden (1971) for details, that makes this an attractive proposal for a knock detector. Thus, for a given α, $P_\alpha(y)$ is the multi-dimensional probability density function for the measured data. Using the ideal model (2.8) and the independence assumption, the following expression for the test quantity is obtained

$$g = \max_{\alpha_1 \in \Theta_1} \ln \prod_{i=1}^{L} \frac{P_{\alpha_1}(y(i))}{P_{\alpha_0}(y(i))} = \max_{\alpha_1 \in \Theta_1} \sum_{i=t_{\text{knock}}}^{L} s(i)$$

where

$$s(i) = \ln \frac{P_{\alpha_1}(y(i))}{P_{\alpha_0}(y(i))} = -\frac{(y(i) - \xi(i))^2}{2\sigma_{\text{noise}}^2} + \frac{y(i)^2}{2\sigma_{\text{noise}}^2}$$

Knock is detected if

$$g \cdot \sigma_{\text{noise}}^2 > h$$

Then $\quad t_{\text{knock}} = \arg_{t_{\text{knock}}} \left(\max_{\alpha_1 \in \Theta_1} \ln \prod_{i=1}^{L} \frac{P_{\alpha_1}(y(i))}{P_{\alpha_0}(y(i))} \right)$

2.3.4 On-line test quantity I (ONI)

The variation of the high-pass filtered signal is increased after a knock-onset. Knock detection can thus be performed by monitoring the signal variance. Assuming that the expected signal value is 0 for all t, a change detection test can then be written as (Gustafsson, 2000):

$$\begin{aligned} s(t) &= y^2(t) - \hat{\sigma}_y^2(t-1) \\ g(t) &= \max(g(t-1) + s(t) - v, 0) \end{aligned}$$

Knock is detected if $g_e(t) > h$. As a rule of thumb, the drift v should be chosen as one half of the expected magnitude of change. The signal variance is estimated recursively using:

$$\hat{\sigma}_y^2(t) = \lambda \, \hat{\sigma}_y^2(t-1) + (1 - \lambda) \, y^2(t), \quad \lambda \in [0, 1]$$

where the forgetting factor λ should be chosen in the range $0 < \lambda < 1$.

Knock is detected if there exists a time $t = t_{\mathrm{det}}$ such that

$$g_e(t) = \min\{g(t), \ldots, g(t+40)\} > h$$

Then $t_{\mathrm{knock}} = \min_t(t \leq t_{\mathrm{det}})$ satisfying $g(t) \geq h$

2.3.5   On-line quantity II (ONII)

One problem with the off-line approach in Section 2.3.3 is that it is computationally expensive. It may be the case that there are few advantages using a complicated knock model, especially as it deviates significantly from measured traces. A significant reduction in computational effort is achieved by setting the amplitude of a knock oscillation to a constant and known value.

$$\xi(t) = \begin{cases} \xi_0(t) = 0, & t < t_{knock} \\ \xi_1(t) = A\sin(2\pi f(t - t_0)), & t \geq t_{knock} \end{cases}$$

The amplitude A is set to $\beta \in [0,1]$ times the highest value of the HP filtered signal, where β is a design parameter. To avoid the influence of outliers, the signal is filtered with a median filter. The time phasing t_0 is chosen in the range $[0, \frac{1}{f}]$, so that the highest correlation between y and ξ_1 is achieved.

The hypotheses are the same as in (2.9), but with A and $r = 1$ fixed. Knock is detected using CUSUM and log-likelihood (Basseville and Nikiforov, 1993). Compute

$$s(t) = \frac{\xi_1(t)}{\sigma_{\mathrm{noise}}^2}\left(y(t) - \frac{\xi_1(t)}{2}\right), \quad S_1^j = \sum_{i=1}^{j} s(i)$$

Knock is detected if there exists a time $t = t_{\mathrm{det}}$ such as

$$S_1^t - \min_{1 \leq j \leq t} S_1^j > h/\sigma_{\mathrm{noise}}^2$$

The time of knock onset is set to the maximum $t < t_{\mathrm{det}}$ that fulfils

$$\left(S(t) - \min_{1 \leq j \leq t} S_1^j\right) = 0.$$

Knock is detected if there exists a time $t = t_{\mathrm{det}}$ such that

$$g_e(t) = \min\{g(t), \ldots, g(t+40)\} > h/\sigma_{\mathrm{noise}}^2$$

Then $t_{\mathrm{knock}} = \max_t(t < t_{\mathrm{det}})$
satisfying $\left(S(t) - \min_{1 \leq j \leq t} S_1^j\right) \geq 0$

2.3.6 On-line quantity III (ONIII)

The last test quantity is similar to KI20 (König and Sheppard, 1990) that was mentioned in Section 2.2. The test quantity is the signal energy over a limited time interval of L samples, that is

$$g(t) = \int_t^{t+L} y^2(t)dt \approx \frac{1}{f_s} \sum_{k=k_t}^{k_t+L} y^2(k) = g(t)$$

Unlike KI20 the time interval is not fixed to 20°. Instead it is to be calibrated by the user.

> Knock is detected if there exists a time $t = t_{\text{det}}$ such that
>
> $$g_e(t) = \min\{g(t), \dots, g(t+40)\} > h$$
>
> Then $\quad t_{\text{knock}} = \min_t(t \leq t_{\text{det}}) \quad$ satisfying $\quad g(t) \leq h$

2.3.7 Parameters of detection test quantities

The performances of the methods depends heavily on the choice of test quantity parameters. The parameters are here set to eligible values, that make it possible to evaluate the methods—to identify their weaknesses and strengths. Probably, it is possible to improve the performances of the knock detection even further with a carefully prepared calibration of the parameters and thresholds.

ONI The forgetting factor λ is set to 0.95, as a compromise between adaptivity and sensitivity to noise. The expected change magnitude is set to the 99 percentile of the noise distribution. This choice allows knock with lower intensity to be detected if the noise level decreases, at the same time as the risk of false alarm is avoided at high noise levels.

ONII The design parameter β is set to 0.5. A too small β has the disadvantage of making the test quantity sensitive to noise while a β close to 1 is not representative since the amplitude of the oscillation decreases. The frequency of the model signal ξ is set to the dominating frequency of the investigated crank angle region.

ONIII The window length of ONIII is set to 10 samples, which is about one knock oscillation period. This choice results in a rather smooth but distinct trace of the test quantity.

Table 2.1: Measured operating points (OP), where p_{im} is inlet manifold pressure [kPa], N engine speed [rpm], r_c compression ratio, and θ_{ign} the ignition angle [deg bTDC].

OP	p_{im}	N	r_c	θ_{ign}
1	70	1200	9	10°
2	70	1200	9	28°
3	70	1200	14	11°
4	70	1200	14	23°
5	70	2000	14	27°
6	70	3000	9	10°
7	70	3000	14	11°
8	100	1200	10	28°
9	100	1200	14	3°
10	100	2000	10	33°
11	100	2000	14	8°
12	100	3000	9	10°
13	100	3000	10	33°
14	100	3000	14	14°
15	130	2000	9	10°
16	130	2000	10	15°

2.3.8   Thresholds

Finally, the thresholds of the different methods have to be chosen. This is done by calibration on measured knock. The measurements were performed according to the procedure described in Section B.1, and the investigated engine operating points are specified in Table 2.3.8. Visual inspection of OP9 gives that 3 out of 99 cycles contain distinct knock traces, with oscillation magnitudes several times the noise level, and 1 cycle with border-line knock. The thresholds are set just above the border-line knock level, in an attempt to make the methods equally sensitive and thereby facilitating a comparison between them. This means that knock is detected in exactly 3 cycles out of 99 in OP9.

2.4   Pressure noise characteristic

The test quantities of the OFF and ONII methods and the expected change magnitude of ONI include the noise level. Knowledge about the noise characteristic is therefore required. But, to know the characteristics during knocking condition, the noise has to be separated from the knock oscillations. However, a method for this separation is not readily available.

A crank angle region that do not contain any knock is the compression phase. An interesting question is if noise in this phase has similar characteristic as noise in the phase where knock appears, i.e. during combustion. The standard

Table 2.2: Standard deviation of the noise in the compression phase.

OP	σ_{noise} [kPa]	OP	σ_{noise} [kPa]
1	1.61	9	1.61
2	1.55	10	1.87
3	1.60	11	1.81
4	1.64	12	1.62
5	1.62	13	1.61
6	1.69	14	1.64
7	1.67	15	2.24
8	1.63	16	2.17

deviation and auto-correlation of the noise in the compression phase is compared to noise in the crank angle region 10°–40° after top dead centre (TDC), for operating points with no or a low risk of knock. The HP filter used in the compression phase has a lower cut-off frequency (2 kHz) than the one used in the combustion phase, since possible pressure waves travels slower in colder conditions according to (2.5). The result is that the standard deviation differs less than 10% between the phases in all the measured operating points. It is therefore assumed that the noise of the cylinder pressure in the compression phase is equivalent to the noise during combustion.

The standard deviation of the noise in the compression phase is shown in Table 2.2. It is in the same order of magnitude for all investigated operating points, but slightly higher for 2000 rpm. A map of the standard deviations is thus used in the investigation to follow.

Figure 2.4 shows the noise distribution for two representative operating point and it is concluded that the noise is Gaussian distributed. The auto-correlation curve is almost flat for engine speeds of 1000 and 3000 rpm, but at 2000 rpm it has clear oscillations, indicating that the noise is not completely white. In spite of this fact, the noise is forthwith assumed to be white and Gaussian in coherence with (2.8).

2.5   Evaluation on cylinder pressure

The methods from Section 2.3 are evaluated and compared based on measured cylinder pressure. However, it is difficult to make a fair comparison since the outcome of the methods relies heavily on the choices of thresholds and test quantity parameters. The values of the number of detected knocks and the crank angle at knock onset should therefore be regarded as qualitative and not quantitative measures.
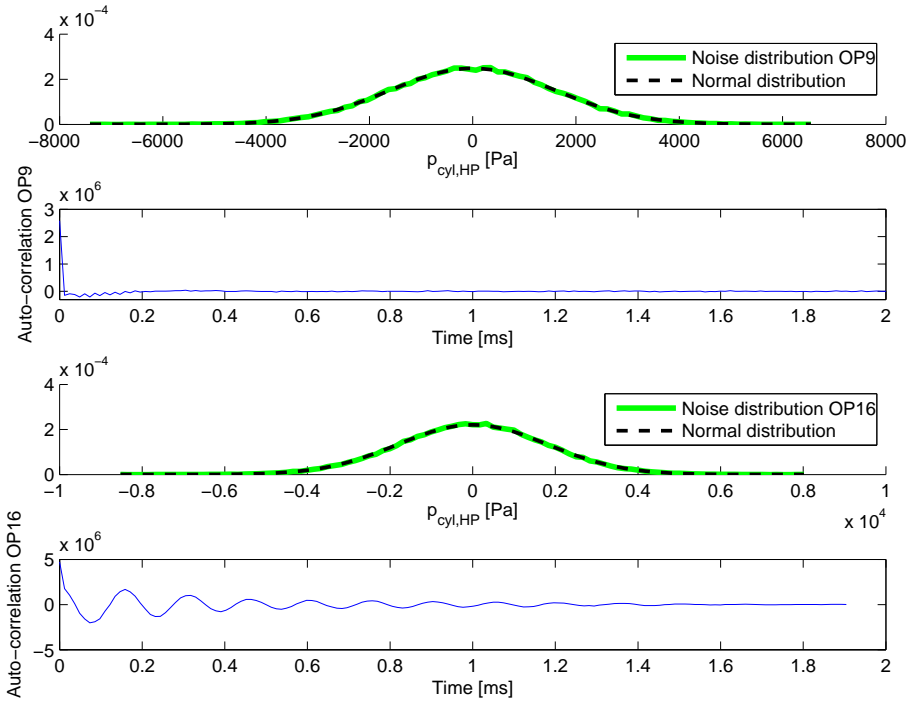
Figure 2.4: Noise distribution and auto-correlation for the noise in OP9 are shown in the two top plots, and for OP16 in the lower two plots.

2.5.1   Knowing the true knock on-set

A problem in the evaluation is that there are no non-disputable answers to the questions whether a cycle contains knock or not, and at what angle the knock is initiated. Figure 2.5–2.8 show 11 measured knock traces. They are all from the same operating point but have various appearances. In Figure 2.5 the trace is distinct. Not many would argue against that there is a knock present and that the knock on-set is at 15° approximately. This kind of knock trace is very common in knock literature. The traces in Figure 2.6 have a much worse signal to noise ratio. If there is knock, the oscillations are so modest that they can be mistaken for noise.

Figure 2.7 illustrates another problem. The signal to noise ratio is not as low as in the previous figure, but the beginning of the oscillations is unclear. The cycles contains knock, but at what angle is it initiated? In Chomiak and Sköld (1995) these traces are categorised as *weak* knock, while traces consistent with the ideal knock signature are named *strong* knock. The explanation given to the weak knock behaviour is that only a small fraction of the end gas auto-ignites
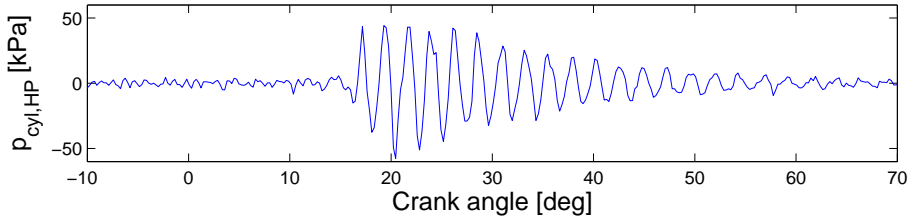
Figure 2.5: A knock trace similar to the ideal knock signature. The cycle is measured at 3000 rpm, inlet manifold pressure 100 kPa, compression ratio 14 and ignition angle at 11° bTDC.

initially, generating a moderate blast wave. The remaining part of the end-gas is ignited later on, either randomly in sequential explosions or by the reflected wave.

Yet another problem is illustrated in Figure 2.8. The traces show evidence of two separate knock onsets. Looking at the left figure, one may estimate the knock onset to either 5° or 15°, since at both time instants a damped oscillation is initiated. The fact that there can be more than one auto-ignition centre was shown already by König and Sheppard (1990), by studying photographs from inside the combustion chamber, and is also discussed in Burgdorf and Chomiak (1998). If only one knock onset should be detected each cycle, it is a question of definition which onset is the correct one.

Visual inspection of the cylinder pressure traces from the operating points in Table 2.3.8 indicates that the problem with knowing the true knock angle increases with engine speed. At 3000 rpm many cycles have traces with the same problems as the ones in Figure 2.7 or 2.8. Figure 2.9 shows a measure of non-ideality of the knock traces, which illustrates how the deviation from the ideal knock signature depends on operating point. The measure takes into account the sudden appearance of a pressure oscillation with an amplitude which decreased with time, and it is defined as the mean angular distance between detected knock onset and the angle at maximum absolute value of the filtered cylinder pressure

$$\theta_{\text{max amp}} = \arg \max_{\theta} |p_{\text{cyl,HP}}(\theta)|$$

Knock is here detected with the ONI algorithm. The measure should be considered qualitative, and its purpose is to indicate at what operating points the problem is most prominent.

The largest values are achieved for OP13 and OP14. At these operating points the engine speed is 3000 rpm. The engine speed is 3000 rpm in the operating points 6, 7 and 12 as well, but these operating points contain no detected knock. The conclusion is that estimation of the knock onset is uncertain for many cycles and a question of definition. The operating points at 3000 rpm are therefore excluded in the evaluation of the detection algorithms.
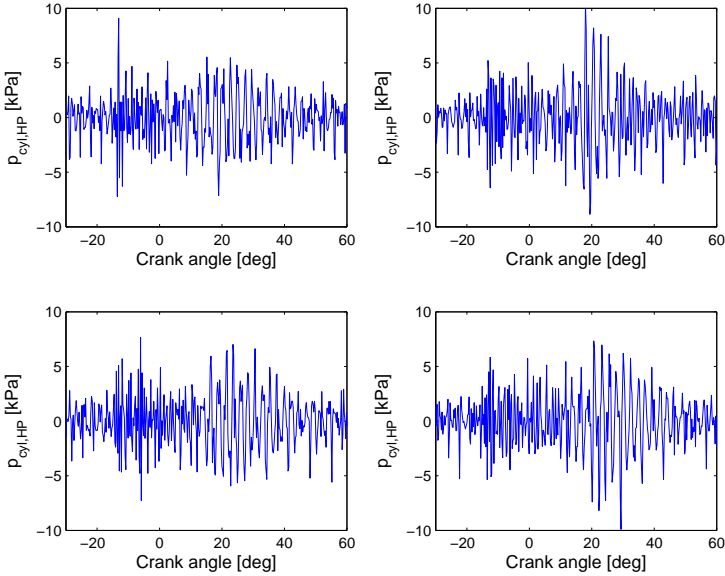
Figure 2.6: Traces of border-line knock. It is difficult to decide whether or not knock is present.
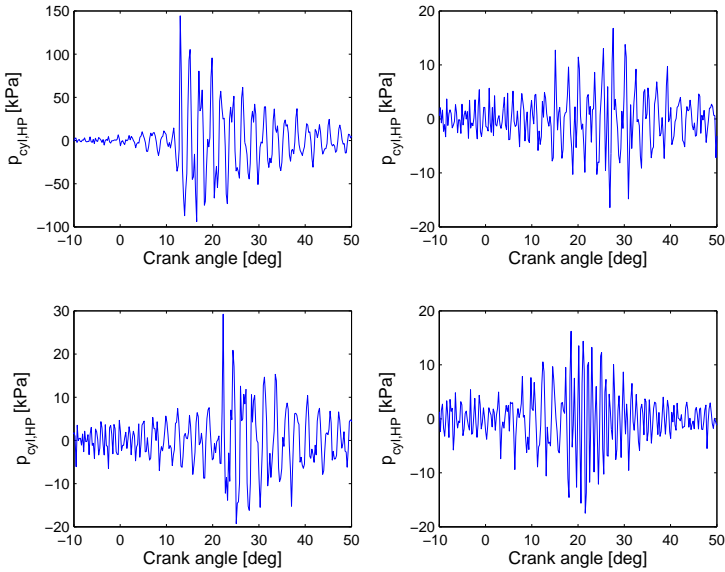
Figure 2.7: Oscillations with indistinct beginning. In the upper left figure the strong oscillations at 15° dominate the appearance, but already at 5° there is a oscillation of the same magnitude as in the other 3 figures.
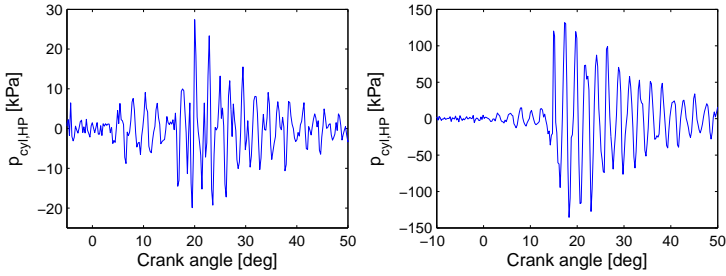
Figure 2.8: The traces indicates that there are more than one auto-ignition centers. The phenomena is clearly visible in the left figure. Looking at the right figure, it may at first sight be obvious that the angle at knock onset is $\approx 15°$. But there is a distinct pressure oscillation already before $10°$, and its amplitude is about the same size as for 3 of the knock traces in Figure 2.7.
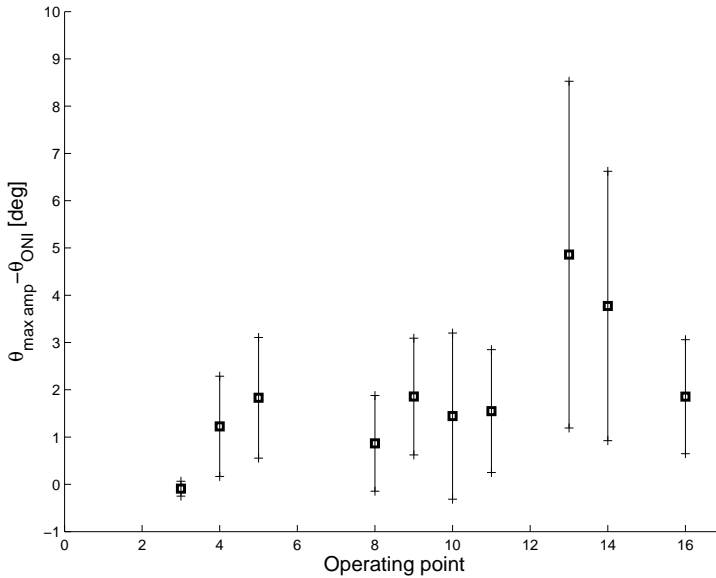
Figure 2.9: Illustration of how the deviation from the ideal knock model depends on the operating point. The squares are the mean value of the non-ideality measure and the horizontal lines its standard deviation.
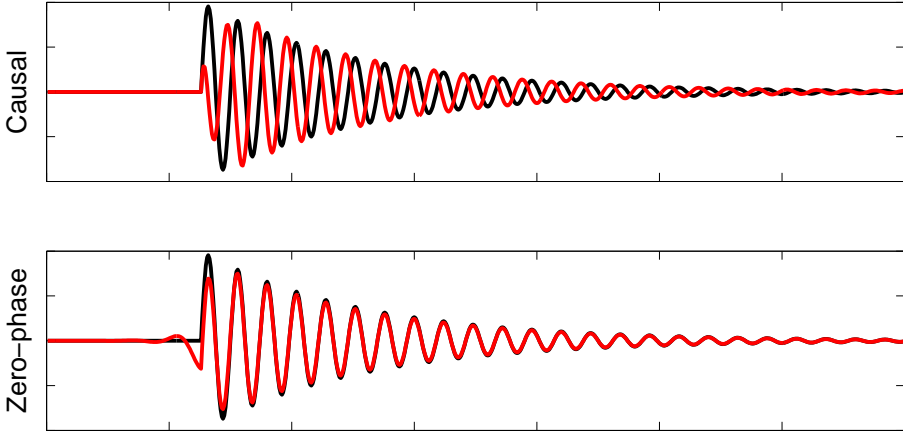
Figure 2.10: High-pass filtered ideal knock signal. At 2000 rpm the oscillation period is about 1.5 CA. **Top:** The filter is a causal 4:th order butterworth. **Bottom:** The filter is a zero-phase 4:th order butterworth.

The high pass filter does not only make the knock oscillations more visible, it also causes a signal distortion. This can be understood from Figure 2.10 where the ideal knock signal (2.8), has been filtered with a causal and a zero-phase filter. As can be seen, if a causal filter is used the first oscillation period is substantially damped and a phase-shift is introduced. On the other hand, if a zero-phase filter is chosen, small oscillations are created in the filtered signal before the time of auto-ignition.

2.5.2   Detected knock and estimated knock angle

The detection algorithms are evaluated on the 11 remaining operating points; the operating points at engine speeds of 1200 or 2000 rpm. The "true" knock onset $\theta_{\mathrm{ref},ci}$ and whether a cycle contains knock is estimated by visual inspection. Cycles where the knock signature is too unclear are here excluded. Signatures that are judged too unclear involve borderline knocks, like the ones in Figure 2.6, and signatures where the uncertainty of knock onset angle is about 5° or more.

The number of detected knocks and the knock angle estimation performance are shown in Table 2.3 and 2.4 respectively. The angle estimation performance measure is the root mean square error (RMSE)

$$\mathrm{RMSE} = \sqrt{\frac{1}{|\mathcal{K}|} \sum_{i \in \mathcal{K}} \left(\theta_{\mathrm{knock},ci} - \theta_{\mathrm{ref},ci} \right)^2}$$

where $\theta_{\mathrm{knock},ci}$ is the detected auto-ignition angle for cycle ci using one of the methods in Section 2.3, $\mathcal{K}$ is the set of cycles where knock have been detected

Table 2.3: Number of cycles with detected knock. The right-most column shows the number of knocks given by the visual inspection and the number of cycles used in the operating point. The number of measured cycles is 99 in all the operating points, but due to indistinct knock traces some of the cycles have been excluded.

OP	OFF	ONI	ONII	ONIII	ref/n_{cycles}
1	0	0	0	0	0/99
2	0	0	0	0	0/99
3	3	3	3	3	4/94
4	90	83	83	87	91/93
5	82	81	79	82	83/83
8	30	44	48	45	66/89
9	82	81	83	83	91/95
10	17	38	36	45	57/73
11	56	49	49	52	64/82
15	0	0	2	1	7/87
16	71	80	74	79	80/80

Table 2.4: Estimated knock angle RMSE. Only operating points with more than 25 cycles with correctly detected knocks, are shown in the table.

OP	OFF	ONI	ONII	ONIII
4	0.66°	0.86°	0.59°	0.50°
5	1.08°	0.69°	1.56°	1.11°
8	1.43°	0.57°	0.49°	0.29°
9	0.98°	0.73°	0.56°	0.43°
10	4.99°	2.33°	3.60°	1.69°
11	1.19°	0.93°	1.31°	1.57°
16	2.96°	0.82°	1.40°	1.62°

by both the method and by visual inspection, and $|\mathcal{K}|$ the number of cycles in $\mathcal{K}$.

The result is good for all methods except in OP 10 and OP 16, since the RMSE for the estimated crank angle at knock onset is between 0.5° and 2°. This is about the same accuracy as the estimated precision of the visual inspection.

ONI has the best performance with RMSE $< 1°$ for all the operating points except in OP10. OP10 has many borderline knocks, which is one explanation to the low numbers of detected knocks and the RMSE of 1.7°–5.0°. More knocks will be detected if the thresholds are set lower or if the window length of g_e is reduced, but this will also increase the risk of false alarm. Both the off-line method and ONII fails to detect several knocks in OP 10, even though some of these are not borderline knocks, and the knock angle estimation is poor. The problem is caused by the model signal consisting of a single oscillatory frequency, while in many of the cycles of OP 10, the knock has not one domi-
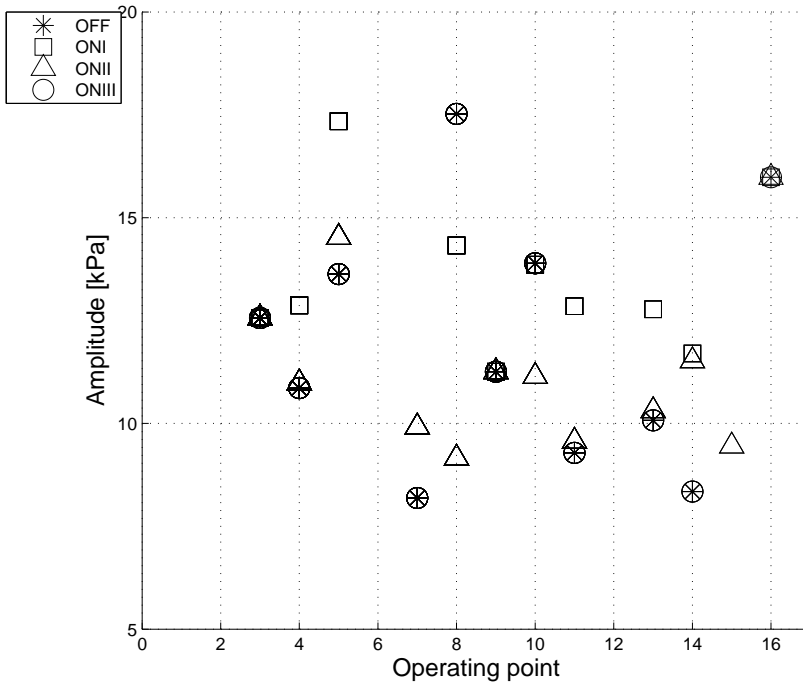
Figure 2.11: The smallest detected knock, considering the maximum amplitude of the knock trace. The values are in the range 5–20 kPa for all four methods in all the operating points where knock is detected.

nating frequency but 2 or 3. The performance of ONII is evidently better and more uniform over the operating points than OFF. The assumption of a single damped oscillations in the OFF method is apparently a weakness.

Using the algorithms, with the choices of parameter values in Section 2.3.7, it is possible to detect knock with as small maximum amplitude as 15 kPa approximately. Figure 2.11 shows the smallest maximum amplitude of the detected knocks in each operating point. The smallest maximum amplitude is

$$\min_{\mathcal{K}} \left(\max_t |\, p_{\text{cyl,HP}}(t)| \right)$$

where $\mathcal{K}$ is the set of cycles with detected knock. Figure 2.12 shows the knock traces of the four cycles with the smallest amplitudes of the ones shown in Figure 2.11, all four with maximum amplitudes less than 10 kPa. It is evident that knock is present in all four traces, which means that the detection is correct.
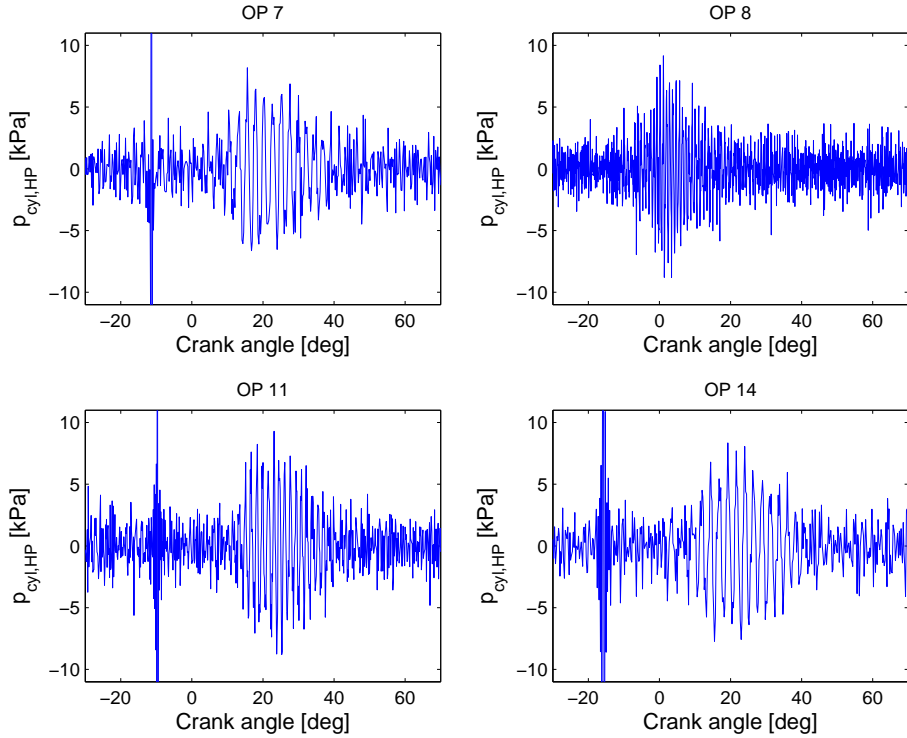
Figure 2.12: The cylinder pressure traces that correspond to the four smallest amplitudes in Figure 2.12. The knock is close to the borderline of knock.

2.5.3 Robustness

In the previous section, the knock detection methods were evaluated on the prevailing conditions. But the conditions might change. For example, measuring cylinder pressure with another equipment may result in an increased or decreased noise level, and another designer may chose other values on the thresholds. It is important to be aware of how these changes affect the outcome of the methods. Therefore, robustness to changes in noise level, window length, and thresholds on knock detection and knock onset estimation are investigated. These properties are common to all methods, except for window length which is common to all the on-line methods but not the off-line method.

Operating point 9 is used in the evaluation since it contains many knocks in a wide range of intensities and for most of its cycles the knock signatures are distinct. All 99 measured cycles are here included.

Noise Noise sensitivity is analysed by adding a vector with random numbers equally distributed as the measurement noise, but with higher variance. There

are two possible situations; the algorithms are aware of the increased noise level and can therefore adjust parameters and thresholds, or they lack this information and can therefore not adapt to the current conditions. Algorithm performance in these two situations are shown in Figure 2.13 and Figure 2.14 respectively, where the measured signal has been modified from the original

$$y = p_{\text{cyl,HP}} + e_{\text{orig}}, \quad e_{\text{orig}} \sim N(0, \sigma_{\text{orig}})$$

where σ_{orig} is given by Table 2.2, to the more noisy signal

$$y = p_{\text{cyl,HP}} + e_{\text{orig}} + e_{\text{add}}, \quad e_{\text{add}} \sim N\left(0, \sigma_{\text{orig}}\sqrt{k^2 - 1}\right)$$

That is, Gaussian distributed noise has been added to the measured signal and the resulting total variance of the noise is k^2.

ONIII has problems with high noise levels. The signal energy in a time window increases when the noise level increases. More and more knocks are therefore detected by ONIII, until the number of cycles of detected knock reaches its maximum 99. At the same time, the estimated knock onset approaches the beginning of the investigated crank angle interval. As the mean crank angle at knock onset according to the visual inspection is $20°$ after the beginning of this interval, the angular deviation between detected and reference angle ends up at $20°$. Since the parameter and threshold of ONIII do not include the noise level, there is no difference in behaviour between these two figures. Also ONI is affected. In Figure 2.13 it is seen that the number of knocks detected by ONI decreases, and this is explained by that the expected change magnitude is increased. However, the estimation becomes unreliable if the change magnitude is not adjusted, as can be seen in Figure 2.14

Window length   The influence of varying the window length of the effective test value g_e in (2.6) is shown in Figure 2.15. ONII is completely unaffected by changes in this range. This can be explained by the flat appearance of test quantity ONII in Figure 2.3. The outcome of the other two on-line methods varies with window size, but none of the methods have a deviation higher than 6% in the number of detected knocks, compared to at the original window size of 40 samples. The changes in estimated knock angle deviations are less than $0.2°$.

Threshold   Increasing the threshold obviously decreases the number of detected knocks and vice versa, as shown in Figure 2.16. The rate of decrease is the same for all methods. The change in thresholds h ranges from a factor $1/4$ to 4. Still the change in mean estimated knock angle deviation is $0.5°$ at most.
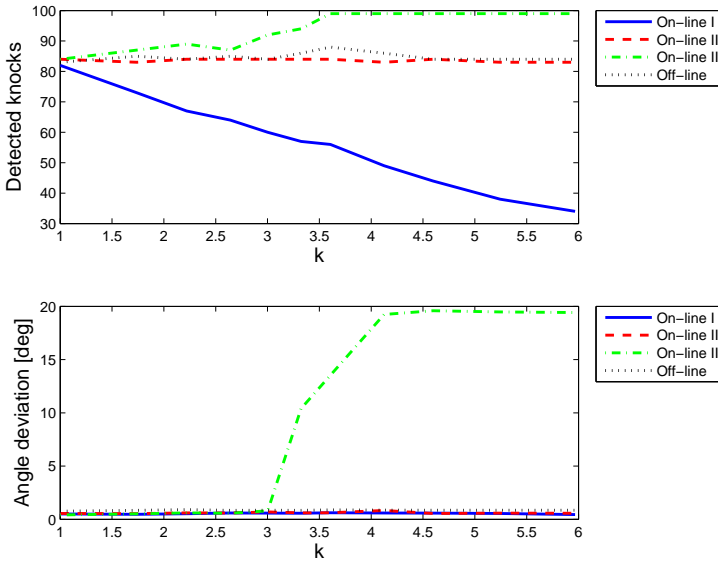
Figure 2.13: Results of methods when noise is added to the cylinder pressure (OP 9). The design parameters are adjusted with the new noise level.
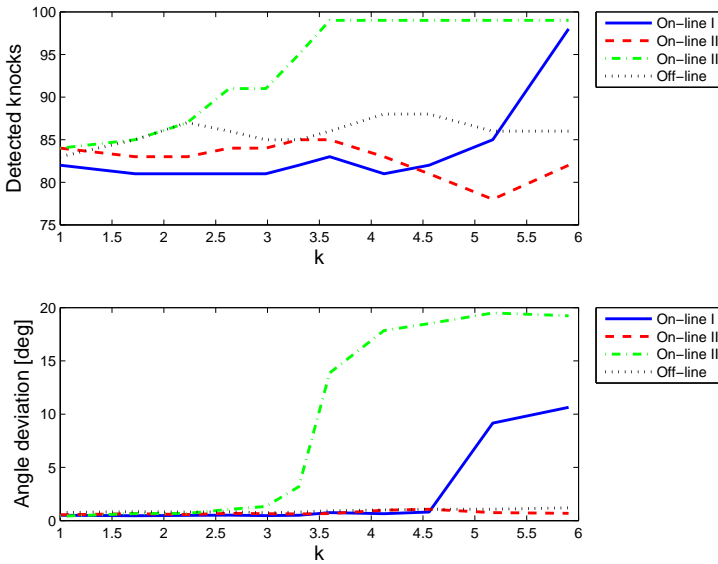
Figure 2.14: Results of the methods when noise is added to the cylinder pressure (OP 9), without adjusting the design parameters.
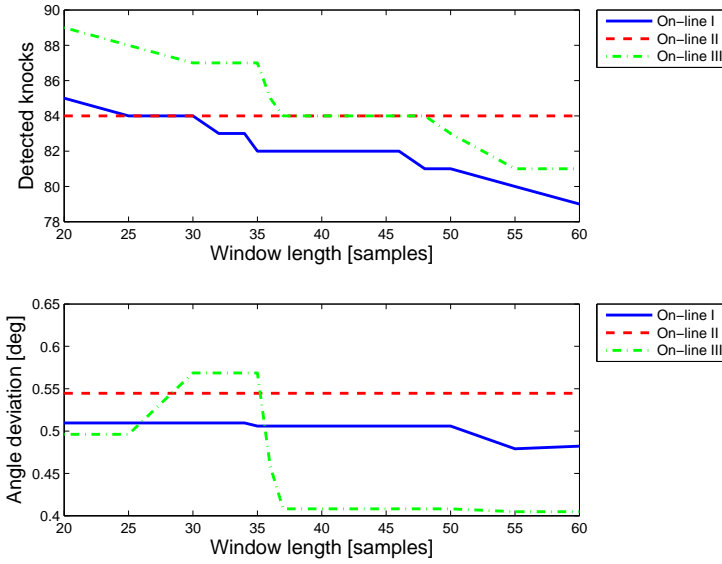
Figure 2.15: Results of methods on OP 9 when the window size of the effective test (2.6) is changed.
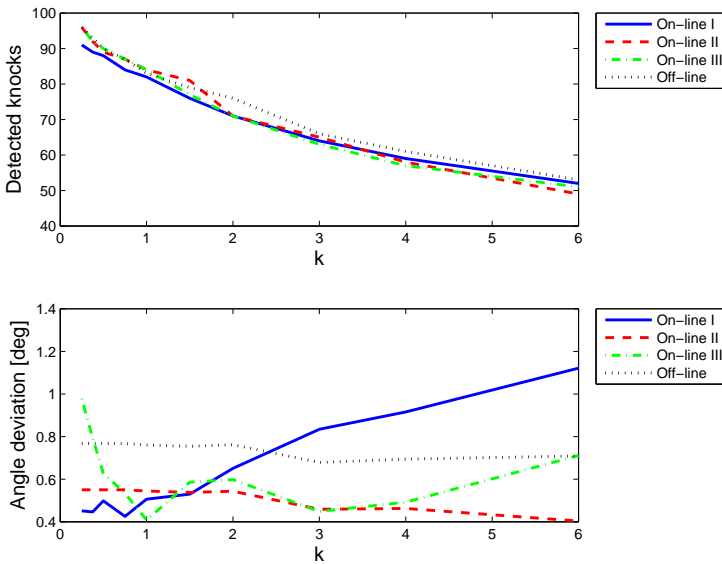
Figure 2.16: Results of methods for different values of thresholds on OP 9, where $h_{\mathrm{new}} = k \cdot h$.

2.6 Conclusions

Four different methods for detecting knock and estimating crank angle at knock onset from cylinder pressure are investigated and compared. The outcome of the investigation depends on the choice of test quantity parameters and thresholds, and should therefore be considered as qualitative measures.

With the choice of the property values used here, the methods are able to detect knock with maximum amplitude as small as approximately 15 kPa. The RMSE of estimated angle compared to the reference is 1.7° or less, except for two operating points. ONI has the smallest RMSE with less than 1°. The exceptions are OP 10 and 16, where several of the measured cycles contain knock with a fundamental oscillatory mode that is not dominant. This is something that the off-line method and ONII have problems to handle. Besides this, many of the cycles of operating point 10 have borderline knock, which the methods fail to detect if they are too small.

Knock detection using the off-line method is the most computationally demanding. However, the performance of the method is no better than for the other methods. The reason for this is that the off-line method relies heavily on the accuracy of the knock signal model (2.8) and that the model has been shown to be unreliable.

A weakness of ONI and ONIII is that they are sensitive to noise, while for OFF and ONII neither the estimation of angle at knock onset or the number of detected knock were influenced by the increased noise level. The conclusion is thus that if there is a high signal to noise ratio, ONI is an appropriate choice of knock detection method. In a noisy environment ONII is a better choice.

At modest knock intensity levels, a significant fraction of the knock traces do not resemble the ideal knock signature, with a distinct start of oscillation followed by a continuous decrease in amplitude. Some of the traces show signs of multiple auto-ignition centres, and many traces have distinguishable oscillations already 5–10° before the maximum amplitude occurs. The deviation from the ideal knock signature increases with engine speed. The non-ideality of the knock traces makes it difficult, or even impossible, to identify the true knock onset in the cylinder pressure. Yet another problem is the signal distortion caused by the high pass filter.

Correlation between knock intensity measures

The focus of this chapter is to find correlations between different knock properties. The aim is to translate the crank angle at knock-onset, which is the outcome of a many knock predictive models, into signal characteristics of the cylinder pressure.

The role of a knock controller is to control the engine into a knock-free region—but why should knock be avoided? There are two main reasons: Firstly, knock can damage the engine. Secondly, the pinging noise originating from the knock induced pressure oscillation inside the combustion chamber distracts and troubles the driver. There are different opinions about how engine knock can cause damage to the engine. In Maly et al. (1990) it is concluded that erosion may be caused by excessive surface stresses due to large local heat fluxes and/or by high peak pressures in positively interfering reflected shock waves. Another example is Fitton and Nates (1996), in which the results showed that the erosion was correlated to the cylinder pressure at the point of auto-ignition, while no correlation was found between erosion and the peak-to-peak pressure amplitude. However, a knock controller should not aim towards the borderline of engine destructive knocks, but towards no or inaudible and harmless knock. It is therefore natural to use feed-back on the oscillation intensity in the control algorithm.

In the pursuit of understanding the knock phenomena and facilitating the design of new engines and knock controllers, a lot of research have been done in the field of knock prediction. Based on the results in Li and Williams (1999), Li et al. (2000) presents a detailed mechanism for auto-ignition of methane, consisting of 128 elementary reactions of 31 species. The mechanism is then successfully reduced into 6 steps. Auto-ignition of n-heptane and iso-octane is even more complicated. Noda et al. (2004) simulates auto-ignition using a two-zone model, including a detailed chemical kinetic model of 462 reactions and 99 chemical species. Soyhan et al. (2000) describes how to automatically reduce a mechanism for auto-ignition of n-heptane and iso-octane, consisting of 510 reactions of 75 species, where the final result is a mechanism of 19 species.

As can be understood from these examples, using chemical kinetics for modelling auto-ignition results in highly complex models. Livengood and Wu (1955) suggests a different approach. All reactions are combined into a single Arrhenius-like function for the ignition delay τ

$$\tau = c\,e^{-\frac{b}{T_{\mathrm{cyl}}}}\,p_{\mathrm{cyl}}{}^{n} \qquad (3.1)$$

where c, b, and n are empirical constants. The time of auto-ignition is the time $t_{\mathrm{a.i.}}$ that fulfils

$$\int_{t_{\mathrm{IVC}}}^{t_{\mathrm{a.i.}}} \frac{1}{\tau}\,dt = 1 \qquad (3.2)$$

Douaud and Eyzat (1978) continues this work, and suggests the following ex-

Table 3.1: Symbols and shades used in the figures of this chapter.

Colour	Data set
Grey	OR95
Black	OR99

Symbol	Compression ratio
*	8
∘	10
□	12
△	14

pression for the ignition delay

$$\tau = 17.68 \cdot 10^{-3} \left(\frac{\text{ON}}{100} \right)^{3.402} p_{\text{cyl}}^{-1.7} e^{\frac{3800}{T_{\text{cyl}}}} \tag{3.3}$$

The cylinder pressure p_{cyl} is here in atmospheres, and ON is the octane number of the fuel. Yates et al. (2005) refines the approach by dividing the combustion process into two distinct regimes with different parameter settings; a two-stage, low-temperature regime and a single stage high temperature regime. The ignition delays are calculated separately for each stage, and are then combined to give the overall ignition delay. An example of an application of the ignition delay approach is Elmqvist et al. (2005), where the single stage ignition delay model is combined with a one-dimensional model of the engine for predicting knock.

These examples of publications contains only a small fraction of the many scientific works that have been done in the field of knock-onset prediction. The question that will be examined here is how to relate the predicted angle at knock-onset to the intensity of the knock oscillations.

3.1 Some notes about the correlation study

The data sets used in this study are the OR95 and OR99 data sets that are described in Appendix B.1. The results and figures are presented on a mean value basis if not stated otherwise. In most figures, each marker represents a single operating point, for which the mean value is calculated for 500 consecutive cycles. However, in some of the figures only cycles with detected knock are included in the mean value. This will be stated explicitly when this is the case. The symbols and shades used in the figures are explained in Table 3.1.

3.2   Knock intensity measures

Before any correlation with knock angle can be investigated, knock intensity
has to be defined. There exists many different definitions in the literature, and
all these can not be discussed here. This section will therefore only cover some
of the most common measures.

   Maybe the most common of all measures is the maximum amplitude of the
high pass (or band pass) filtered cylinder pressure. A variation of this measure
is to take difference between the maximum and minimum filtered pressure. The
maximum amplitude of the pressure oscillations is often called MAPO, but is
here denoted $p_{\mathrm{HP,max}}$.

   Another intensity measure is the knock energy. The energy of a signal y is
(Gustafsson et al., 2001)

$$E_{\mathrm{signal}} = \int_{-\infty}^{\infty} |y|^2 \, dt \tag{3.4}$$

Since knock is present only during the combustion phase, it is natural to define
knock energy of cycle i as the signal energy in a limited time window of length
T, starting at time t_0:

$$E_{\mathrm{knock}\,i} = \int_{t_0}^{t_0+T} |p_{\mathrm{cyl,HP}_i}(t)|^2 \, dt \tag{3.5}$$

This intensity measure was used in knock detection method ONIII in Chapter 2.
Another commonly used name for knock energy is IMPO, the Integral of Mod-
ulus of Pressure Oscillations. The window length T is often chosen such that it
includes the whole extension of the oscillation, but is sometimes set shorter.

   A disadvantage with $p_{\mathrm{HP,max}}$ is that there are knocks that include a strong
peak in amplitude which endures for only one oscillation. The measure is then
not representative for the rest of the knock trace. On the other hand, it captures
the oscillation-caused stresses and unbalances in the cylinder, where the knock
energy measure is more blunt. A middle way is to use I_{knock}, which is defined
as

$$I_{\mathrm{knock}\,i} = \max_t \frac{1}{L} \sum_{k=t-L+1}^{t} p_{\mathrm{cyl,HP}_i}^2[k] \tag{3.6}$$

This is the measure that is used in Chapter 5. The window length L is there
set to about 2.5 knock oscillation periods, which is the same length as in the
knock detection algorithm ONIII in Chapter 3.

3.2.1   Logarithmic normalised knock energy

The goal of this section is to propose a knock intensity measure that has nice
signal properties and is natural to relate to the energy release after an onset of
knock.

Energy is released unevenly in the combustion chamber in the rapid combustion of fuel that follows auto-ignition, and this gives rise to inhomogeneities in the cylinder pressure. It may therefore be expected that the released amount of energy at knock onset correlates with the intensity of the knock oscillations, and the proposed knock intensity measure will therefore be based on the knock energy measure (3.5).

Figure 3.1 shows the mean knock energy of 500 consecutive cycles, that is

$$E_{\text{knock}} = \frac{1}{N_{\text{cycles}}} \sum_{i=1}^{N_{\text{cycles}}} E_{\text{knock}\,i} \tag{3.7}$$

where N_{cycles} is the number of cycles. It can be seen that the knock energy increases with compression ratio and earlier ignition, and that the increase seems exponential—the increase is first hardly noticeable and then changes very rapidly. It is therefore practical to base the knock intensity measure on the logarithm of knock energy. The use of the logarithmic knock energy is not a new idea, although it is rarely seen in the literature compared to the use of knock energy. Hudson et al. (2001) uses logarithmic knock energy in a knock detector, and in Naber et al. (2006) it is concluded that cycle-to-cycle variations of the knock intensity defined as

$$\int_0^T |p_{\text{cyl,HP}}(t)|\, dt$$

is approximately log-normal distributed.

A problem with knock energy is that its value depends on the window length T. Ideally, the window length is chosen such that the window begins at the knock-onset and ends where the oscillations can no longer be seen. Unnecessary noise will otherwise be included and add to the value of knock intensity. Since the angle at knock-onset is normally not known, the window is set to a crank angle region where knock is likely to happen. If time-equidistant sampling is used and T is set to a constant number of samples, it follows that the included crank angle region at 3000 rpm is only a third of the length at 1000 rpm, which increases the risk of not capturing the oscillations. If the intensity measure is defined as the contribution of a knock to the signal energy, that is

$$E_{\text{knock}\,i} - T \cdot \sigma_{noise\,i}^2 \tag{3.8}$$

where $\sigma_{noise\,i}^2$ is the noise variance, the measure is insensitive to window length. This assumes that the window is chosen long enough to include the whole oscillation. Unfortunately, the logarithm of (3.8) is not an appropriate choice of knock intensity measure. For cycles without knock (3.8) is zero, and the logarithm is $-\infty$.

Based on this discussion, the following intensity measure is proposed, called the logarithmic normalised knock energy

$$G_{\text{knock}\,i} = \ln \left(\frac{E_{\text{knock}\,i} - \sigma_{\text{noise}\,i}^2 (T - L)}{\sigma_0^2 L} \right) \tag{3.9}$$
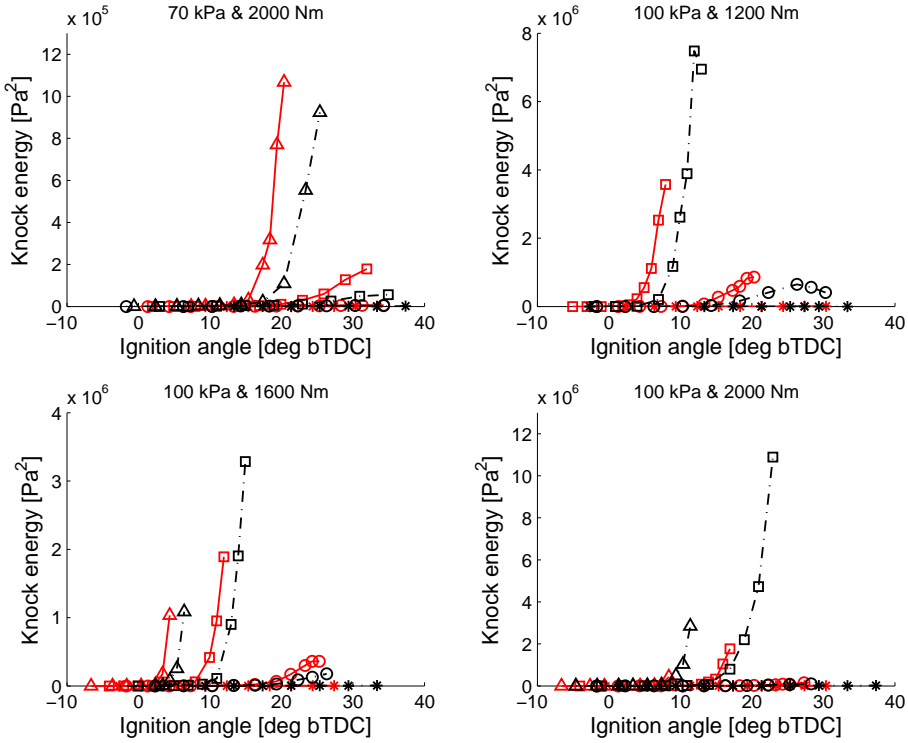
Figure 3.1: Mean knock energy of the 500 consecutive cycles in each measuring point. A guide to the symbols used in the figure is found in Table 3.1.

where L is constant for all operating points and set to approximately the time extension of a knock oscillation. The window length $T > L$ is set to the length of the crank angle region where knock is likely to be found. Note that L is a fixed number of samples, while the number of samples of T depends on engine speed.

If σ_0 is set to $\sigma_0 = \sigma_{\text{noise}i}$, the measure is insensitive to window length T, zero for cycles without knock, and > 0 for cycles with knock. However, the value of the intensity is then dependent on the noise variance, which obstructs comparisons between operating points with different noise levels. The noise parameter σ_0 is therefore set constant for all operating points, and to a value that is representative of the noise in the whole engine operating range. In the data sets used here, $\sigma_{\text{noise}i}^2$ does not change much from cycle to cycle, neither with ignition angle and compression ratio, and it is therefore not necessary to update its value each cycle. Its value is here set constant in each individual speed and load point.

In the calculations of G_{knock}, L is here set to 400 samples and the knock
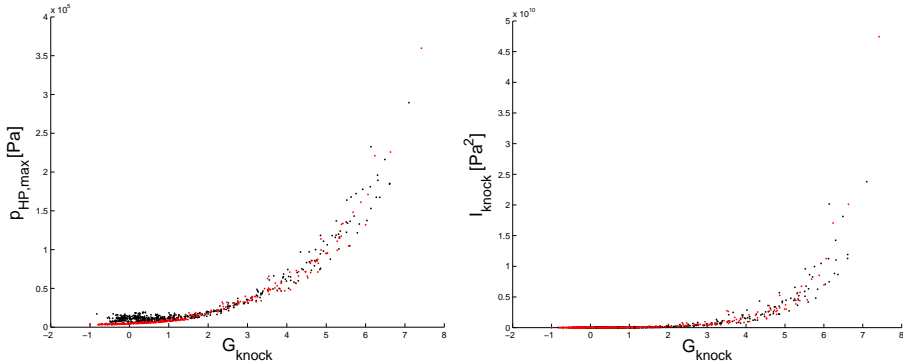
Figure 3.2: Comparison between G_{knock} and $p_{HP,max}$ and I_{knock}. Each dot is the mean value of the 500 cycles in each operating point. Both the OR95 and OR99 data sets are included in the two figures.

energy window to $[\theta_{ign} + 4°, \theta_{ign} + 100°]$. Figure 3.2 shows that G_{knock} is correlated with both $p_{HP,max}$ and E_{knock}. However, the characteristics of the cycle-to-cycle variations are nicer for G_{knock} since its values are more evenly distributed, as can be seen in Figure 3.3. Figure 3.4 shows the distribution for an operating point at low knock intensity, and one operating point with high knock intensity. It can be concluded from the figure that the distribution for the high knock intensity operating point is approximately Gaussian. At low knock intensity levels, the noise distribution interacts with the distribution of the knock oscillations, which makes the combined distribution oblique. This is something that has to be taken into account in a statistical analysis.

3.2.2 Unburned mass fraction at knock onset

The knock oscillations arise from the inhomogeneities in cylinder pressure that is caused by the rapid release of chemical energy after a knock-onset. The more mass that remains unburned at knock-onset, the higher amount of energy can be released. It may therefore be assumed that the unburned mass fraction at knock-onset correlates with the intensity of the knock oscillations. This relation will be investigated in the next section, Section 3.3, but first the unburned mass fraction has to be determined.

The unburned mass fraction at knock onset $x_{u,knock_i}(\theta_{knock})$ is estimated from the cylinder pressure in several steps. The first step is to derive a combustion profile by heat release analysis. A single-zone heat release model based on the Gatowski model (Gatowski et al., 1984) is used. Only an approximate profile is needed to examine whether there is a correlation between $x_{u,knock}$ and E_{knock}. The effects of heat transfer, crevice flows and blow-by are therefore
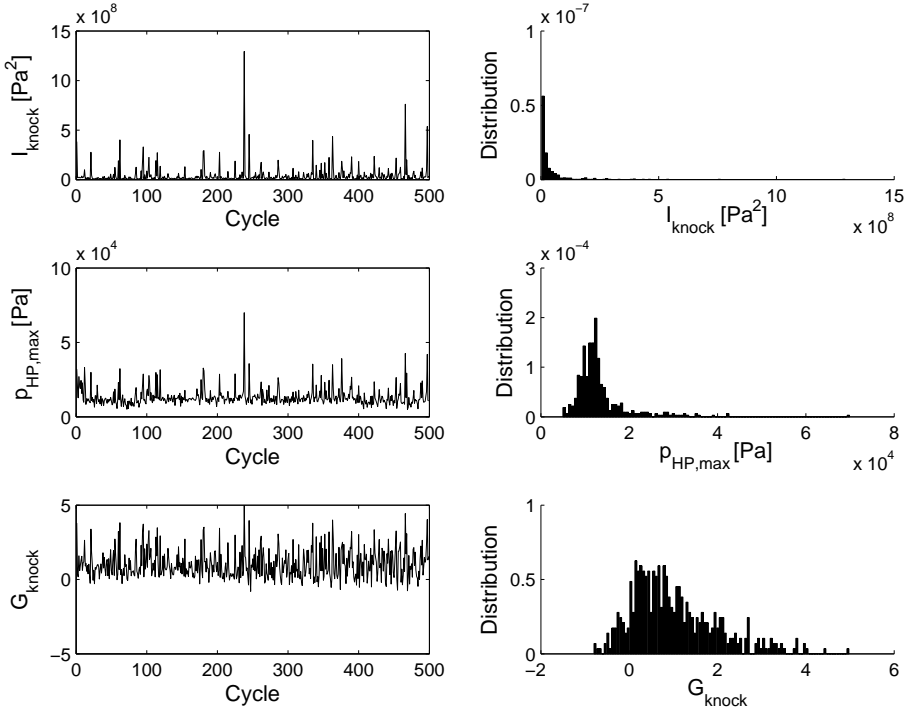
Figure 3.3: Signal characteristics of the knock intensity measures I_{knock}, $p_{\text{HP,max}}$, and G_{knock}, in a low-intensity operating point. Knock intensities for 500 consecutive cycles measured in a single operating point are shown. The knock intensity is evidently stochastic. The plots to the left show the cycle-to-cycle variations of the knock intensity measures, and the plots to the right show the distribution of the 500 cycles.

neglected. The chemical energy released in combustion at each instant is

$$\delta Q_{\text{chem}} = \frac{c_v}{R}\, V\, dp + \frac{c_v + R}{R}\, p\, dV \qquad (3.10)$$

Heat release calculated for a cycle with normal combustion is shown in Figure 3.5.

Due to the large data size of each measured operating point, it is very time consuming to first load and convert the data, and then calculate the heat release trace each time information about mass fraction burned is needed. Time can of course be saved by storing the calculated traces, but this requires a large storage capacity. An alternative is to use the Wiebe function. The Wiebe function provides a good approximation of the mass fraction burned x_b (Vibe,
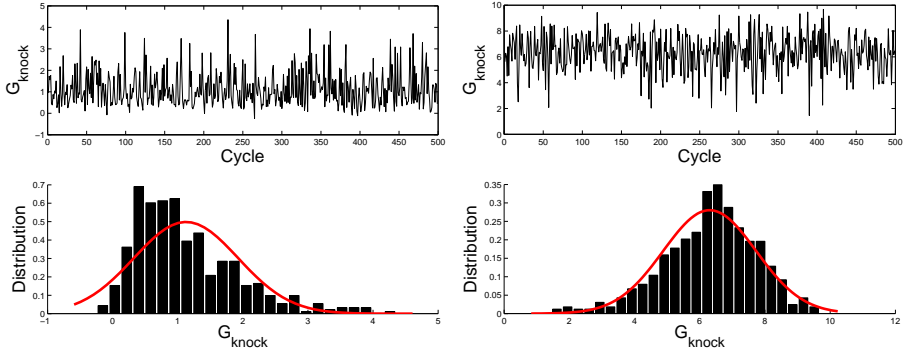
Figure 3.4: Cycle-to-cycle variations and distribution of the knock intensity measure G_{knock} in an operating point with low knock intensity (left), and high knock intensity (right). A Gaussian distribution has been fitted to the data (bottom figure).

1967)

$$x_{\text{b}}(\theta) = 1 - e^{-a\left(\frac{\theta - \theta_{\text{ign}}}{\Delta\theta_{\text{b}}}\right)^{m+1}} \tag{3.11}$$

where a, m and $\Delta\theta_b$ are parameters that are identified for each individual cycle. The values of the Wiebe parameters are saved, and the next time a heat release trace is required it is calculated from the Wiebe function using the stored parameter values.

The method used for identifying the Wiebe parameters is the one proposed in Eriksson (1999a):

$$m = \frac{\ln\left(\frac{\ln(1-0.1)}{\ln(1-0.85)}\right)}{\ln\Delta\theta_{\text{d}} - \ln(\Delta\theta_{\text{d}} + \Delta\theta_{\text{b}})} - 1 \tag{3.12}$$

$$a = -\ln(1-0.1)\left(\frac{\Delta\theta}{\Delta\theta_{\text{d}}}\right)^{m+1} \tag{3.13}$$

where $\Delta\theta$ is the combustion duration, $\Delta\theta_{\text{d}}$ is the flame development angle, and $\Delta\theta_{\text{b}}$ the rapid burning angle. The combustion duration is the angular distance between ignition and end of combustion. The flame development angle is the crank angle from ignition to 10% mass fraction burned, and the rapid burning angle is the crank angle from 10% to 85% mass fraction burned.

Finally, the unburned fuel fraction at knock onset is calculated by inserting the estimated knock angle in (3.11). The estimation of the crank angle at knock onset is done with detection method ONI, see Section 2.3.4. The parameter values of the method and its threshold are set to the same values as in Section 2.3.7–2.3.8.

The estimated unburned fuel fractions at knock-onset should be regarded as
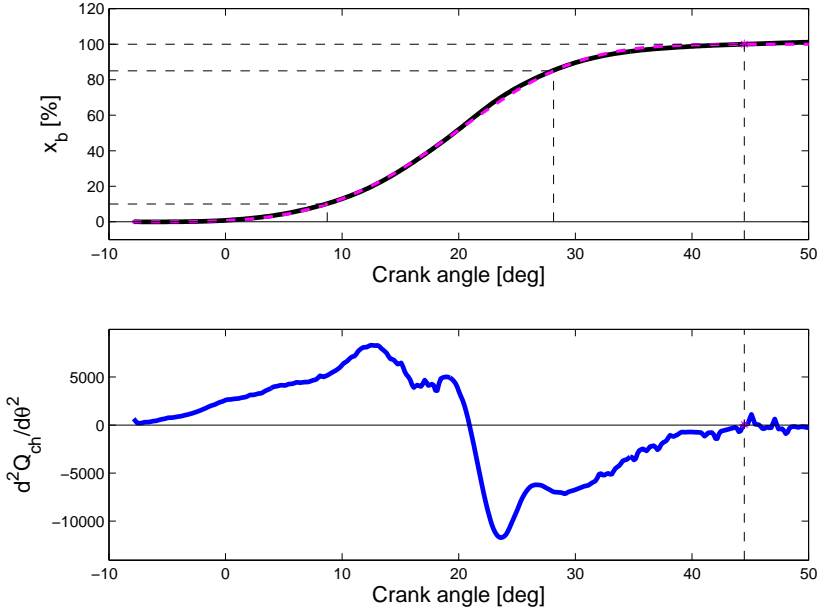
Figure 3.5: Top figure shows the heat release trace, calculated from a low-pass filtered cylinder pressure (solid line). The modelled heat release estimated with the Wiebe function (3.11) is also shown (grey dashed line). The black dashed lines represents 10%, 85%, and 100% mass fraction burned. The heat release accelerates in the beginning of the combustion, decelerates when the flame front reaches the walls, and stops when no or a small amount of unburned gas remains. End of combustion (100% mass fraction burned) is therefore identified to the crank angle where $\frac{d^2 Q_{\mathrm{ch}}}{d\theta^2}$ switches from negative to positive. This is illustrated in the bottom figure.

approximative values due to the simplifications and uncertainties in the calculations. These are:

- Knock at and beneath borderline intensities is not detected.

- Uncertainty in the detected knock angle. Many cycles show signs of multiple knock-onsets, see the discussion in Chapter 2.

- R and c_v are set constant in the heat release calculation.

- Heat transfer, crevices and blow-by are neglected in the heat release analysis. The burned mass fraction at end of combustion is set to 100%.

- The purpose of the Wiebe function is to describe normal combustion. When knock is present in a cycle chemical energy is released rapidly,

which might not be captured by the Wiebe function. Figure 3.6 shows the heat release trace from a cycle with strong knock. The fit of the Wiebe function is worse than for the cycle with normal combustion in Figure 3.5, but it is still an acceptable approximation.

3.3 Knock intensity and unburned fuel at knock onset

There is no or a weak correlation between unburned mass fraction at knock-onset and knock intensity, as can be seen in Figure 3.7. This is in agreement with the results in Chomiak and Sköld (1995) and Chun and Heywood (1989). The correlation is weak also for $G_{\mathrm{knock}i}$, shown in Figure 3.8.

It is a well known fact that there are severe cycle-to-cycle variations of the knock intensity (see for example Figure 3.3–3.4), and it is therefore interesting to investigate the correlation on mean value basis. To determine the knock intensity of an operating point requires cylinder pressure traces from multiple engine cycles. Brunt et al. (1998) concludes that at least 1000 engine cycles should be used when determining the knock intensity, and the same number of cycles is recommended by Hudson et al. (2001). Measurements with only 500 cycles from each operating point are used in this study, but for finding correlations it is assumed sufficient.

Let $\mathcal{K}$ be the set of cycles with detected knock, then the (mean) unburned mass fraction at knock onset is

$$x_{\mathrm{u,knock}} = \frac{1}{N_{\mathrm{cycles}}} \sum_{i=1}^{N_{\mathrm{cycles}}} \check{x}_{\mathrm{u,knock}_i}, \quad \check{x}_{\mathrm{u,knock}_i} = \begin{cases} x_{\mathrm{u,knock}_i}(\theta_{\mathrm{knock}}), & i \in \mathcal{K} \\ 0, & i \notin \mathcal{K} \end{cases}$$

(3.14)

where N_{cycles} is the number of cycles measured in the operating point. The definition of the mean unburned mass fraction takes into account that all the gas is burned at normal speed for knock-free cycles. Unburned mass fraction versus G_{knock} is shown in Figure 3.9. From the figure it can be concluded that there is a correlation between the two properties, since the knock intensity increases with unburned mass fraction in all the speed and load points.

However, no correlation is found when the mean values includes only cycles with detected knock:

$$x_{\mathrm{u,knock}_{\mathcal{K}}} = \frac{1}{|\mathcal{K}|} \sum_{i \in \mathcal{K}} x_{\mathrm{u,knock}_i}$$

(3.15)

$$G_{\mathrm{knock}_{\mathcal{K}}} = \frac{1}{|\mathcal{K}|} \sum_{i \in \mathcal{K}} G_{\mathrm{knock}i}$$

(3.16)

where $|\mathcal{K}|$ is the number of elements in $\mathcal{K}$. This is shown in Figure 3.10.
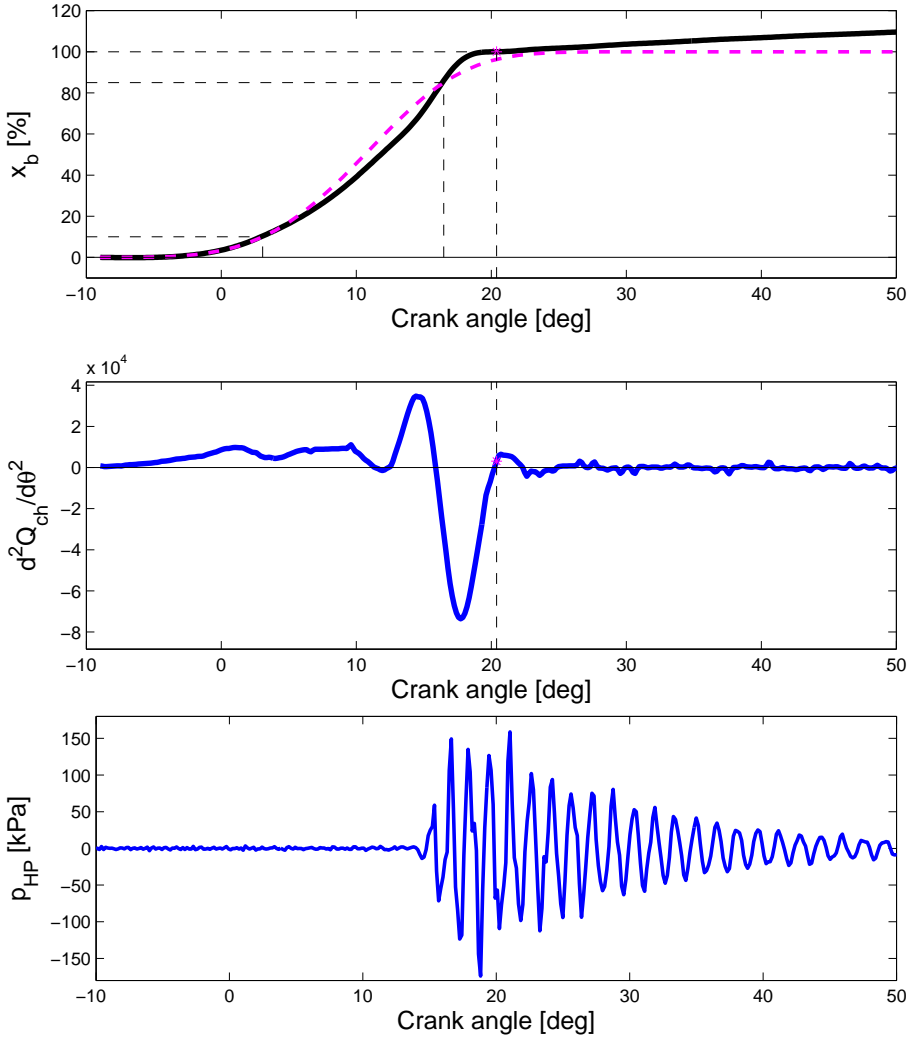
Figure 3.6: Heat release trace for a cycle with knock (compare with Figure 3.5). The bottom figure shows high pass filtered cylinder pressure. It is interesting to note that the burn rate increases after knock-onset, but even though this is a strong knock, the combustion continues for at least 5 crank angle degrees.
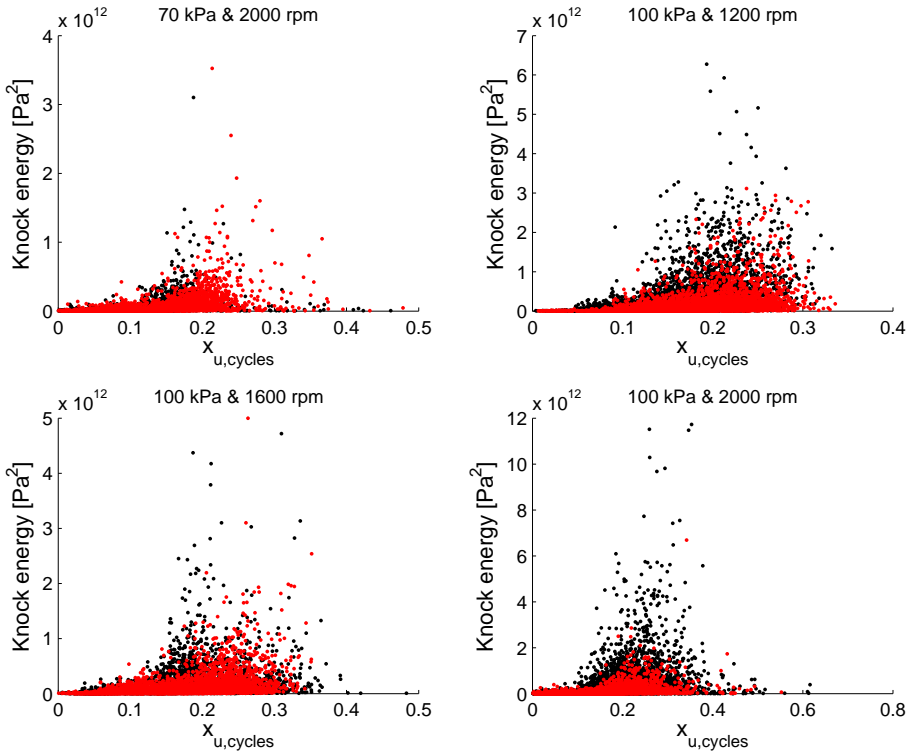
Figure 3.7: Knock energy versus unburned mass fraction at knock onset. Each dot represents a single cycle. The correlation coefficient, defined as $\rho(X,Y) = \frac{Cov(X,Y)}{\sigma(X)\sigma(Y)}$ where σ denotes standard deviation, is 0.3–0.4 for the operating points in the figure. There is no visible correlation, but the correlation coefficient indicates that there may be a weak correlation.

3.4   Knock intensity and rate of occurrence

The results in the previous section may seem contradicting. On one hand Figure 3.7–3.8 and 3.10 can be interpreted to that there is non or a poor correlation between knock intensity and unburned mass fraction at knock onset, on the other hand Figure 3.9 shows a clear correlation. The key to this puzzle is found in the definition of $x_{u,knock}$ in (3.14). By rewriting the definition the following expression is derived:

$$x_{u,knock} = \frac{|\mathcal{K}|}{N_{cycles}}\bar{x}_{u,knock}, \qquad \text{where} \quad \bar{x}_{u,knock} = \frac{1}{|\mathcal{K}|}\sum_{i\in\mathcal{K}} x_{u,knock_i} \qquad (3.17)$$

That is, the unburned mass fraction at knock onset depends on the number of cycles with knock. Figure 3.11 shows knock intensity versus rate of knock
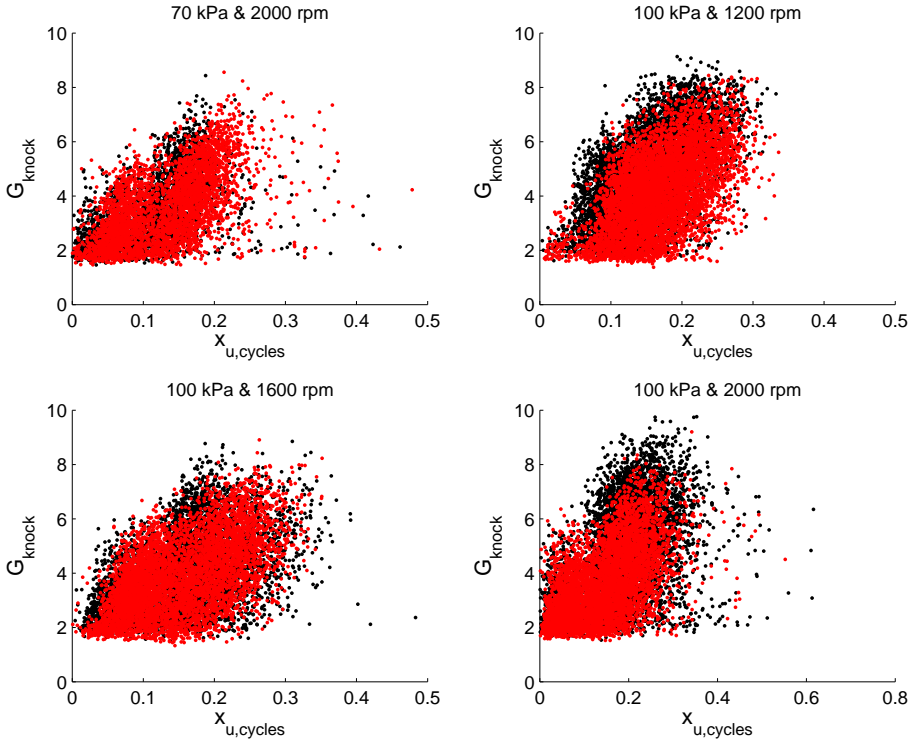
Figure 3.8: Logarithmic normalised knock energy versus unburned mass fraction at knock onset. The correlation coefficient $\rho(x_{\mathrm{u,knock}_i}, G_{\mathrm{knock}i})$ is 0.5–0.6. (The region $0 < G_{\mathrm{knock}} \lesssim 2$ is empty due to that the threshold of the knock detector is set such that knocks at or below borderline intensities are not detected.)

occurrence (rko), where

$$\mathrm{rko} = \frac{|\mathcal{K}|}{N_{\mathrm{cycles}}} \tag{3.18}$$

The knock intensity G_{knock} has an almost linear relationship with rko in the range $0.1 < \mathrm{rko} < 0.9$. The slope is approximately the same for all speed and load points, all compression ratios, and both fuels (octane rating 95 and 99). The curves have bended curve segments in their both ends, which is due to that the number of cycles with knock can neither be larger than the number of measured cycles nor lower than 0.

If only the cycles with detected knock are included in the value of G_{knock}, the slope is no longer constant between speed and load points and compression ratios, as can be seen in Figure 3.12. However, there is still an evident correlation between G_{knock} and rko.

A possible explanation to why the intensity increases with the rate of knock
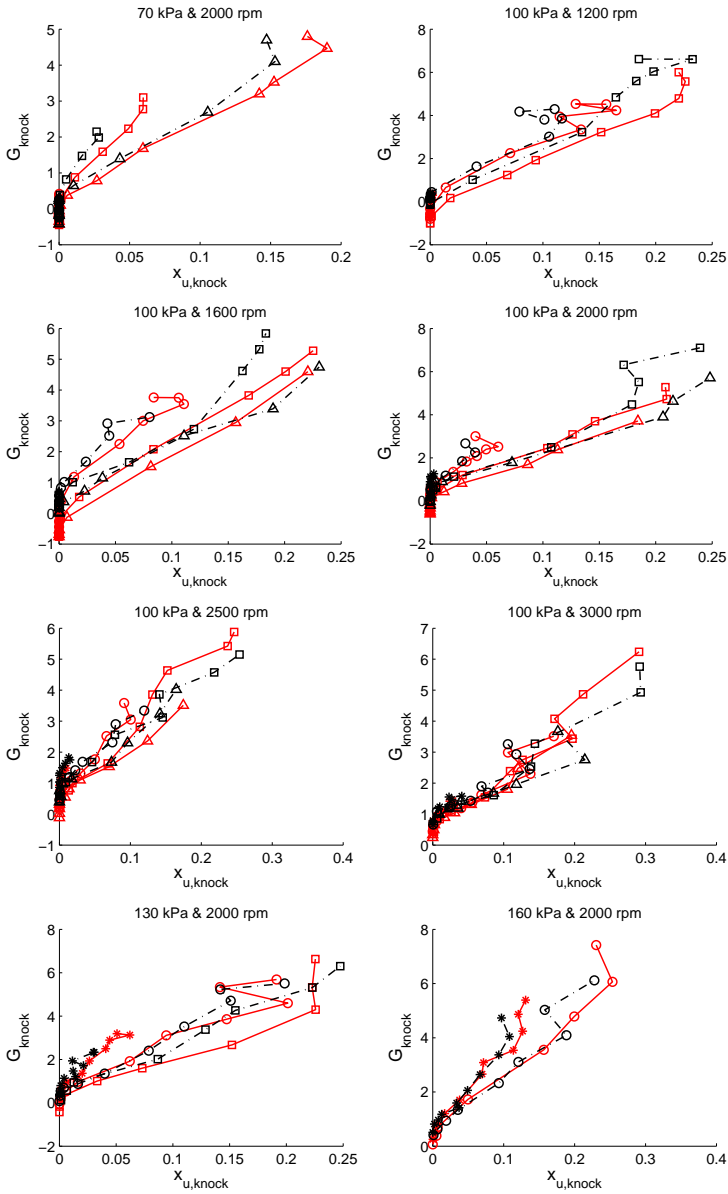
Figure 3.9: Knock intensity G_{knock} versus unburned mass fraction at knock-onset. Each marker represents the mean value of 500 cycles in a single operating point. The correlation coefficient is between 0.88 and 0.98. There is an evident correlation between the two properties.
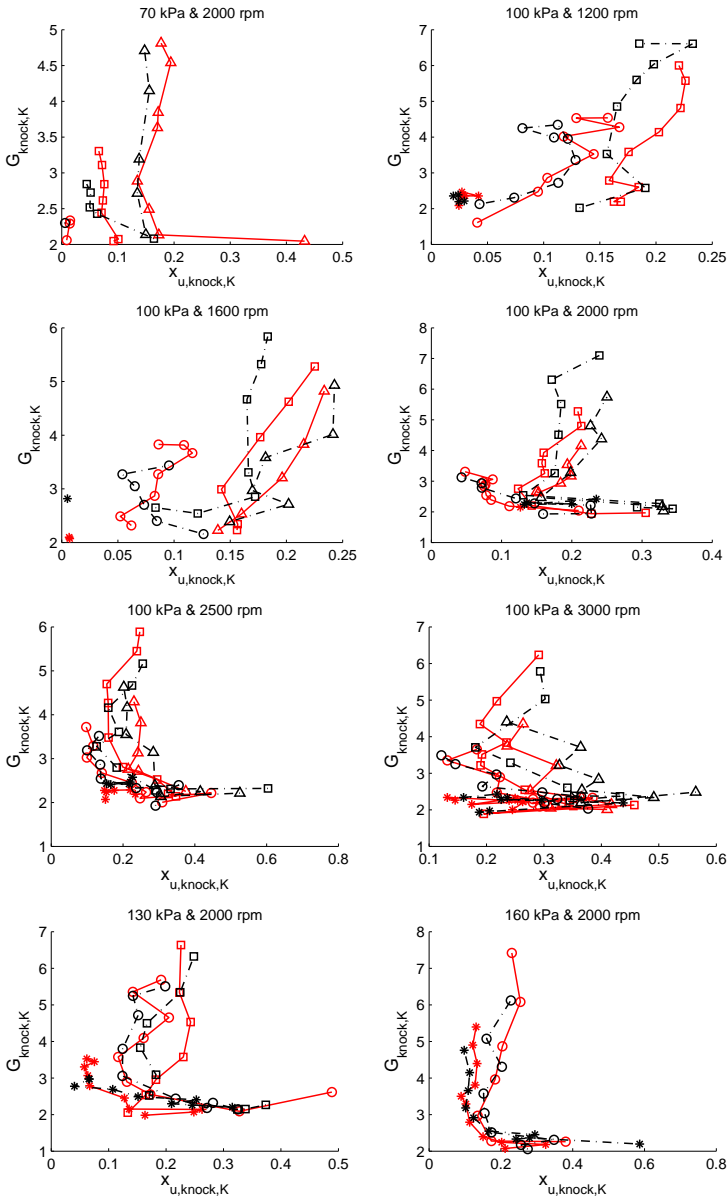
Figure 3.10: Knock intensity G_{knock} versus unburned mass fraction at knock-onset. Each marker represents a single operating point, but only cycles with detected knock is included in the mean values. The correlation coefficient has wide-spread values in the range -0.5 to 0.6 for the different operating points, and its average value for all the operating points is ≈ 0. No correlation is found between the two properties.
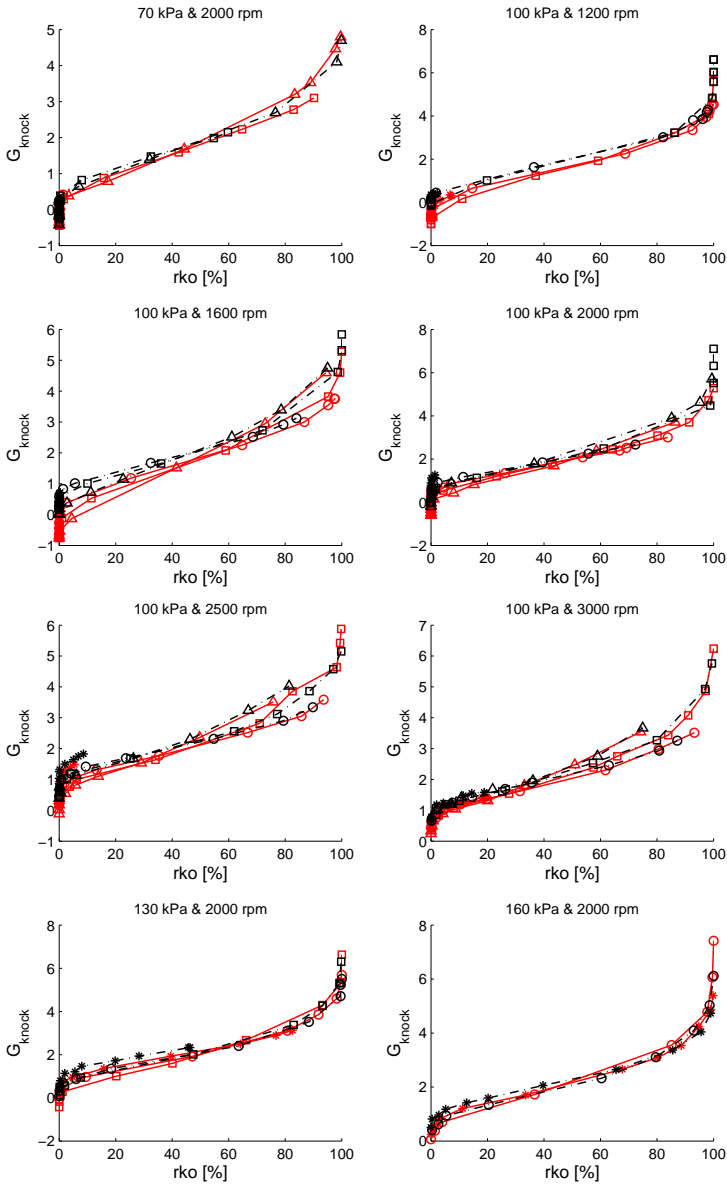
Figure 3.11: Knock intensity G_{knock} versus rate of knock occurrence (rko). All 500 cycles are included in the mean value of each operating point. There is an almost linear relation between the two properties. The bended curve segments in the beginning and end of each plot is explained by the limited number of cycles—rko can never be higher than 100% or lower than 0%. The correlation coefficient is 0.93–0.98 for the operating points in the figure, including both the linear part and the values in the bended curve segments.
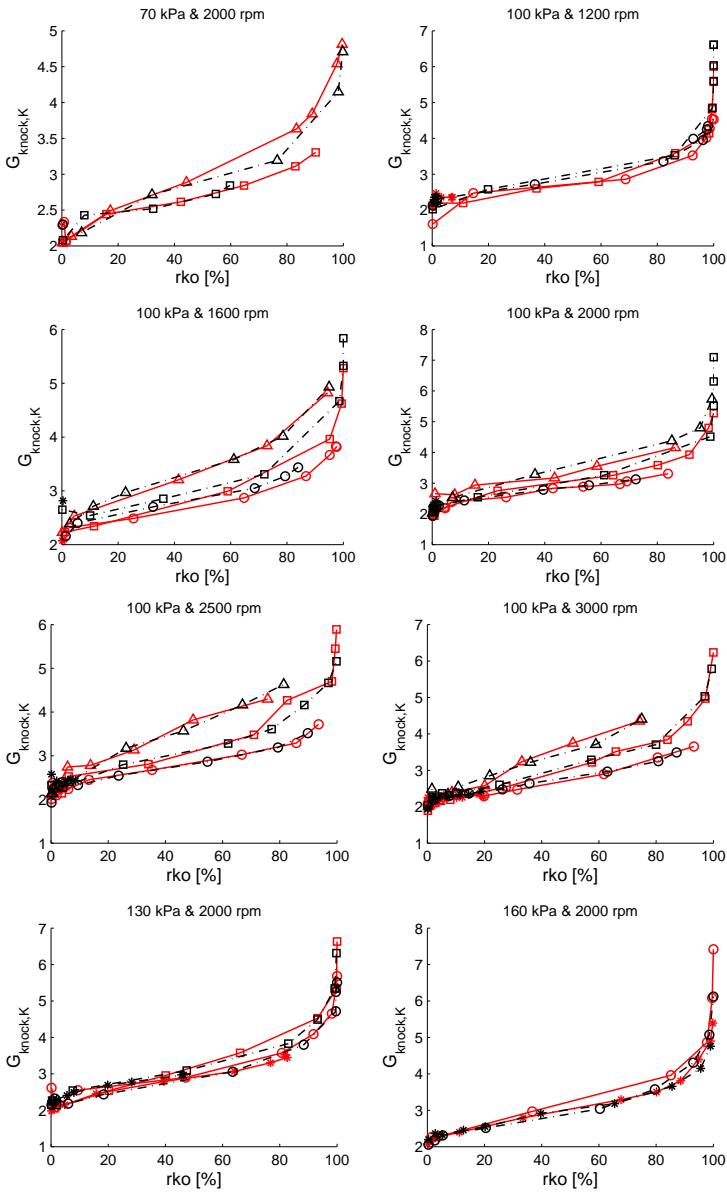
Figure 3.12: Knock intensity G_{knock} versus rate of knock occurrence (rko). Only cycles with detected knock are included in the mean value of G_{knock}. There is still an almost linear relation between the two properties, but the slope depends on compression ratio and speed and load point. The correlation coefficient is 0.88–0.94 for the operating points in the figure.

occurrence, is that in an operating point with low probability of auto-ignition it is required that the phasing of the combustion profile to piston movement provides a high peak pressure, and that inhomogeneities in mixture and temperature are distributed such that reaction promoting conditions coincide in some location of the combustion chamber. As an example, Hajireza et al. (2000) showed that inhomogeneities in the air fuel ratio as small as 0.001 in the mole fraction of n-heptane can lead to hot-spot autoignition onset. If an auto-ignition occurs on these conditions, it is reasonable to believe that the burn speed after combustion is lower for this cycle than for a cycle in another operating point, for which the gas is auto-ignited even though the mixture and temperature field is more evenly distributed. A lower burn speed results in less pressure unbalance and therefore smaller oscillations.

The value of rko depends on the choice of knock detector threshold, since if the threshold is set to a low value more knocks are detected, and vice versa. The values of $G_{\mathrm{knock}i}$ in Figure 3.8 indicate that it is possible to lower the threshold significantly without risking false alarm. Figure 3.13 shows the relation between G_{knock} and rko for 3 different thresholds, where $h = 400 \cdot 10^6$ is the threshold that is used in the rest of the figures. These plots show that the bended curve segments in the beginning and end of the curves depend on threshold, as well as the slope of the middle part of the curve. This was expected, since more/less knocks are detected. However, the correlation between knock intensity and rate of knock occurrence is evident for all three choices of thresholds.

3.5   Conclusions

From the results in this chapter, as well as the previous chapter 2, it is concluded that the words angle at knock-onset should be used with the utmost care. In the knock intensity region that is of importance for knock control, the results show that many cycles include multiple knock-onsets and/or undertake a gradual increase in amplitude during several crank angle degrees.

Keeping this in mind, the unburned mass fraction at knock-onset is estimated, and its correlation to knock intensity investigated. The results show weak correlation on individual cycle basis, good correlation on mean value basis when all cycles are included, and no correlation on mean value basis when only the cycles with detected knock are included. A strikingly good correlation is instead found between knock intensity and the rate of knock occurrence. The relation is close to linear for all the investigated speed and load points, compression ratios and the two types of fuel. This correlation also explains the correlation between knock intensity and the unburned mass fraction on mean value basis.

The knock intensity measure that is proposed and used in the investigation is named the logarithmic normalised knock energy. Usage of logarithm makes the values of the intensity measure more manageable than conventional measures such as IMPO and MAPO, since the mean oscillation amplitude shows an
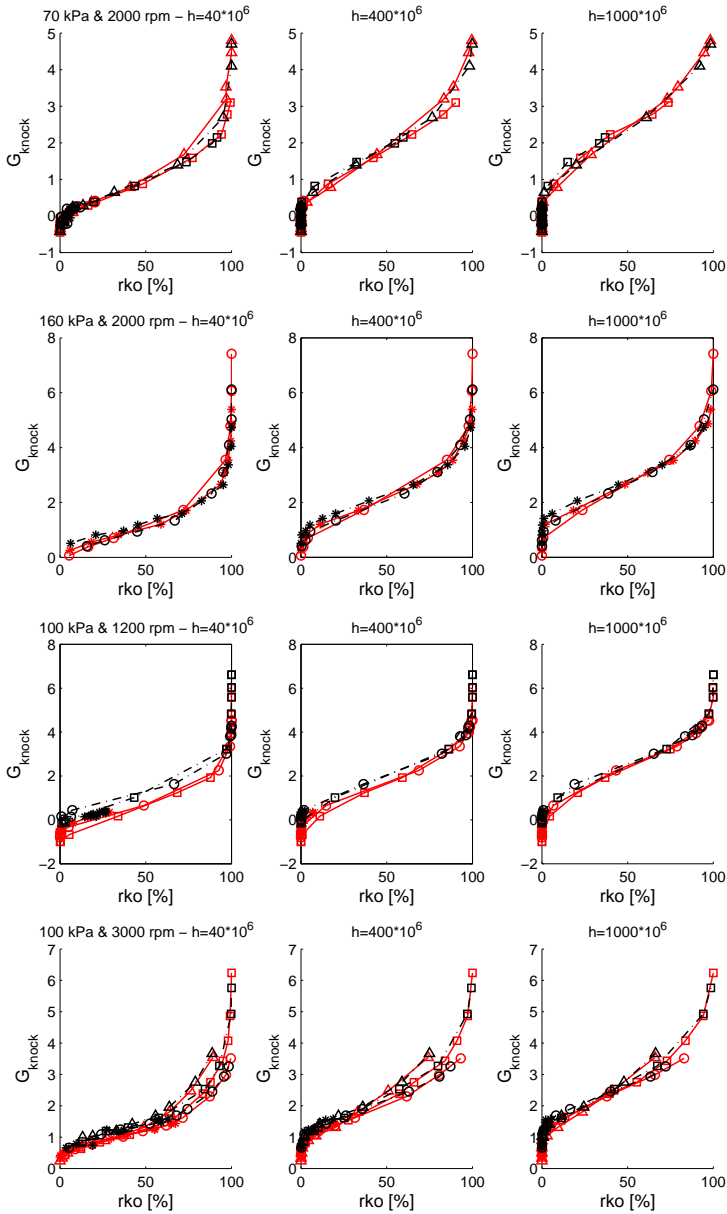
Figure 3.13: Knock intensity G_{knock} versus rate of knock occurrence (rko), for 3 different values on the knock detector threshold h. All 500 cycles are included in the mean value of each operating point. The bended curve segments in the beginning and end of the curves and the slopes of the curves change with the choice of threshold value. However, the relation remains clear and almost linear in the middle part of the curve for all 3 choices of threshold value.

exponential growth with ignition angle. The normalisation provides that the knock intensity is approximately 0 at no knock and > 0 for cycles with knock. Another attractive property is that its distribution in an operating point is approximately Gaussian at high and medium knock intensities. At low knock intensities, the distribution of the noise interacts with the knock distribution, which makes the combined distribution oblique.

A knock controller can use feedback on rate of knock occurrence instead of knock intensity and vice versa, since the knock intensity and rate of occurrence are highly correlated. A large number of engine cycles are needed to determine the knock intensity with high accuracy. The results from this investigation open up the possibility to combine rate of knock occurrence and knock intensity in order to reduce the required number of engine cycles.

Models intended to be used in knock control or in the design phase of the knock control algorithm should focus on the probability of knock occurrence, rather than predicting the angle at knock-onset.

Part II

Engine modelling

4

A NEW FORMULATION OF MULTI-ZONE COMBUSTION ENGINE MODELS

This chapter is based on Nilsson and Eriksson (2001).

Cylinder pressure simulation is an important tool when developing and evaluating new engine concepts and control strategies. Cylinder pressure models are derived from the first law of thermodynamics that connects the thermodynamic properties such as pressure and temperature to the engine revolutions. These models have been developed with different complexity and are used in a wide range of applications from analysis of engine data from test-benches to predicting the performance of new engine concepts. Many of the models are currently too complex to be implemented directly in engine management systems and are mainly used in laboratories and for off-line simulations. However, the computational power of the computerised control systems is steadily increasing and will in the foreseeable future enable real-time implementations of these models. This opens up possibilities for direct monitoring and control of the combustion process.

Here, a new formulation of zero-dimensional multi-zone models is developed and described. The model is: a) zero-dimensional since it does not take spatial variations in the zones into account, b) multi-zone since the cylinder is divided into a number of zones. These are homogeneous and have their individual thermodynamic properties. It should be mentioned that the underlying structure of the model is the same as most other models presented in the literature, so the model is not new in itself; instead, it is the formulation that is new. A general model structure is formulated that relies on a set of differential algebraic equations that are easy to solve. The selected formulation also results in models that are easy to scale, i.e. add and remove zones, and to increase complexity, which is a result of the selected structure.

A wide variety of models have been described in the literature (Ramos, 1989; Keating, 1993; Turns, 2000), and the user of the model can choose among a number of models of varying complexity and select the model best suited for the application. This possibility is further enhanced with the new formulation. In addition, this chapter also shows how to handle a number of practical problems that arise when the general model formulation is used in simulations.

4.1   The multi-zone combustion model

Consider a system with N zones, where $N \geq 1$. The whole system has a certain volume, pressure and mass (V, p, and m). Each zone i has its own volume, temperature, mass (V_i, T_i, and m_i) and gas composition. The state of each zone is described by p, T_i, and V_i, where the intensive properties p and T_i give the thermodynamic state and the extensive property V_i gives the size. The additional information contained in m_i can be used for checking consistency. The mass of a zone can easily be determined by integrating the mass flows in and out of the zone. The changes in the remaining thermodynamic state quantities (p, T_i and V_i, $i = 1, 2, \ldots, N$) are unknown and are to be determined.

The model is based on the following assumptions: The pressure is homogeneous throughout the system. Each zone is a well-stirred tank that is either

a reactor or an adiabatic mixer. The change in system volume and the mass transfer dm_{ij} from a source j to a zone i are known. The system is quasi-static, meaning that the system follows a path of equilibrium states, and in particular all reacting zones are in chemical equilibrium. The thermodynamic state equation

$$pV_i = m_i\, R_i(p, T_i)T_i \tag{4.1}$$

is valid, where R_i is the mass specific gas constant.

The system consists of N zones. Therefore we know that the sum of all V_i, $i = 1, 2, \ldots, N$, must be the same as the volume of the whole system, i.e.

$$\sum_i V_i = V \tag{4.2}$$

This gives the following relation for the volume differentials

$$\sum_i dV_i = dV \tag{4.3}$$

The energy balance equation for zone i is given by (Sonntag et al., 1998)

$$dU_i = -dQ_i - dW_i + \sum_j h_{ij}dm_{ij} \tag{4.4}$$

where dQ_i is the heat transfer from the zone, dW_i the work done by the gas which is $dW_i = pdV_i$, and h_{ij} the enthalpy of the gas that enters the zone—or leaves if dm_{ij} is negative. The internal energy is

$$dU_i = m_i\, du_i + \sum_j u_i dm_{ij} \tag{4.5}$$

Since the gas composition is not necessarily fixed, du_i depends on the state variables temperature and pressure

$$du_i(p, T_i) = \left(\frac{\partial u_i}{\partial p}\right)_{T_i} dp + \left(\frac{\partial u_i}{\partial T_i}\right)_p dT_i \tag{4.6}$$

The first law applied to a quasi-statistic process yields the relation (Reif, 1965)

$$dU_i = T_i\, dS_i - p\, dV_i$$

as a consequence of the second law of thermodynamics. Using this equation, the first term in (4.6) can be rewritten, using first the Maxwell relations and then the thermodynamic state equation:

$$\left(\frac{\partial u_i}{\partial p}\right)_{T_i} = T_i \left(\frac{\partial s_i}{\partial p}\right)_{T_i} - p\left(\frac{\partial v_i}{\partial p}\right)_{T_i} =$$

$$= -T_i\left(\frac{\partial v_i}{\partial T_i}\right)_p - p\left(\frac{\partial v_i}{\partial p}\right)_{T_i} =$$

$$= -\frac{T_i^2}{p}\left(\frac{\partial R_i}{\partial T_i}\right)_p - T_i\left(\frac{\partial R_i}{\partial p}\right)_{T_i} \tag{4.7}$$

The second term in (4.6) is

$$\left(\frac{\partial u_i}{\partial T_i}\right)_p = \left(\frac{\partial h_i}{\partial T_i}\right)_p - R_i - T_i\left(\frac{\partial R_i}{\partial T_i}\right)_p \tag{4.8}$$

where the enthalpy change is $\left(\frac{\partial h_i}{\partial T_i}\right)_p = c_{p,i}$ (Kittel and Kroemer, 1980). Equation (4.4) together with (4.5), (4.6), (4.7), and (4.8) give

$$pdV_i + c_i dp + d_i dT_i = -dQ_i + \sum_j (h_{ij} - h_i + R_i T_i) dm_{ij} \tag{4.9}$$

where

$$c_i = -m_i T_i \left(\frac{T_i}{p}\left(\frac{\partial R_i}{\partial T_i}\right)_p + \left(\frac{\partial R_i}{\partial p}\right)_{T_i}\right)$$

$$d_i = m_i \left(c_{p,i} - R_i - T_i\left(\frac{\partial R_i}{\partial T_i}\right)_p\right)$$

The ideal gas law in differentiated form gives the last equation needed to get an unambiguous equation system:

$$pdV_i + a_i dp + b_i dT_i = RT \sum_j dm_{ij} \tag{4.10}$$

where

$$a_i = V_i \left(1 - \frac{p}{R_i}\left(\frac{\partial R_i}{\partial p}\right)_{T_i}\right)$$

$$b_i = -m_i \left(R_i + T_i\left(\frac{\partial R_i}{\partial T_i}\right)_p\right)$$

Equation (4.3), (4.9), and (4.10) make up a system of $2N+1$ algebraic differential equations. In these equations, the right hand side of the equality signs are known, while the differentials on the left hand side are to be determined. The differentials on the left hand side are linear in the unknowns, and the system can thus be expressed as

$$\mathbb{A}dx = \mathbb{B} \tag{4.11}$$

where dx is a vector containing all the unknown differentials. Selecting dx to

$$dx = [dp \; dV_1 \; dT_1 \; \ldots \; dV_N \; dT_N]^T$$

yields the following $\mathbb{A}$ and $\mathbb{B}$ matrices:

$$\mathbb{A} = \begin{pmatrix} 0 & 1 & 0 & \ldots & 1 & 0 \\ a_1 & p & b_1 & \ldots & 0 & 0 \\ c_1 & p & d_1 & \ldots & 0 & 0 \\ \vdots & \vdots & \vdots & \ddots & \vdots & \vdots \\ a_N & 0 & 0 & \ldots & p & b_N \\ c_N & 0 & 0 & \ldots & p & d_N \end{pmatrix}$$

$$
\mathbb{B} = \begin{pmatrix}
dV \\
R_1 T_1 \sum_i dm_{1i} \\
-dQ_1 + \sum_i (h_{1i} - h_1 + R_1 T_1) dm_{1i} \\
\vdots \\
R_N T_N \sum_i dm_{Ni} \\
-dQ_N + \sum_i (h_{Ni} - h_N + R_N T_N) dm_{Ni}
\end{pmatrix}
$$

The state variable differentials dx are determined by solving the system of linear equations (4.11). The state variables can thereafter be calculated by numerical integration.

4.1.1   Existence of a solution and uniqueness

To be able to solve (4.11), the determinant of $\mathbb{A}$ has to fulfil $\det \mathbb{A} \neq 0$. The determinant of $\mathbb{A}$ is

$$
\det \mathbb{A} = p^{N-1} \sum_{i=1}^{N} \left((c_i b_i - a_i d_i) \prod_{j \neq i} (d_j - b_j) \right) \tag{4.12}
$$

which is proved in Appendix C. Inserting the expressions for a_i, b_i, c_i and d_i and neglecting the partial derivatives of R_i yields the relation

$$
\det \mathbb{A} = -p^{N-1} \prod_{i=1}^{N} m_i \cdot \sum_{j=1}^{N} \left(V_j c_{v,j} \prod_{k \neq j} c_{p,k} \right) \tag{4.13}
$$

Under these conditions there exists a unique solution to the system of linear equations if and only if all $m_i \neq 0$, $i = 1, 2, \ldots, N$, since there is always at least one $V_i \neq 0$. Necessary conditions for the existence of a unique solution when the partial derivatives of R_i are *not* neglected, adds the requirement that there should be at least one $f_i \neq 0$, $i = 1, \ldots, N$, where f_i is defined as

$$
f_i = 2T_i \left(\frac{\partial R_i}{\partial T_i} \right)_p + \frac{T_i^2}{R_i} \left(\frac{\partial R_i}{\partial T_i} \right)_p^2 - c_{v,i} + \frac{c_{p,i}\, p}{R_i} \left(\frac{\partial R_i}{\partial p} \right)_{T_i} \tag{4.14}
$$

4.2   Simulation aspects

There are some special cases that must be handled before equation system (4.11) can be used in a simulation. The problems are:

1. Non-existing zones – In the beginning of the combustion simulation, one or more zones may be non-existing. For example, there exist no burned gas zone before any gas has been combusted.

2. Ill-conditioned $\mathbb{A}$ matrix

3. Accuracy limitations due to finite precision arithmetic

4. Big relative errors in V_i and m_i, due to accumulation of calculation errors

Solutions to these problems for fixed gas composition are discussed below. The procedures can in most cases easily be extended to cover variable gas composition as well.

4.2.1   Empty zones – Initialising a new zone

One question is what the temperature of a new zone i is when $m_i \to 0^+$, which is for example the case at the start of combustion. Another problem when dealing with empty zones is to determine its state variable differentials, since the equation system can not be completely solved when $\mathbb{A}$ is singular.

Initial temperature   The question about the initial temperature can be answered simply by studying the energy balance (4.4) and the ideal gas law (4.10) for zone i. At the initial state $m_i = V_i = 0$. Assuming that $dQ_i = 0$ and $dR_i = 0$, it follows that

$$p dV_i + 0 \cdot dp + 0 \cdot dT_i = -0 + \sum_j (h_{ij} - h_i + R_i T_i) dm_{ij} \qquad (4.15)$$

and

$$p dV_i + 0 \cdot dp + 0 \cdot dT_i = R_i T_i \sum_j dm_{ij} \qquad (4.16)$$

Contradictory to the assumption, it can be expected that dQ_i has an initial value $\neq 0$, but its contribution during the initial simulation step has a negligible effect after a few simulation steps.

Combining equation (4.15) and (4.16) gives

$$\begin{array}{c} R_i T_i \sum_j dm_{ij} = \sum_j (h_{ij} - h_i + R_i T_i) dm_{ij} \\ \Updownarrow \\ \sum_j (h_{ij} - h_i) dm_{ij} = 0 \end{array} \qquad (4.17)$$

To make this true for all mass flows, h_{ij} has to be equal to h_i as long as $dm_{ij} \neq 0$. Therefore, the initial temperature can be found by solving the equation $h_i(T_{i,init}) = h_{ij}(T_j)$, which is the same as the adiabatic flame temperature. However, it may be the case that $h_{ij} = h_i$ can not be solved analytically. The Newton-Raphson method can then be used:

$$(T_i)_{n+1} = (T_i)_n - \frac{f((T_i)_n)}{f'((T_i)_n)}$$

where

$$\begin{aligned} f((T_i)_n) &= h_i((T_i)_n) - h_{ij}(T_j) \\ f'((T_i)_n) &= c_{p,i}((T_i)_n) \end{aligned} \qquad (4.18)$$

Solving the initial equation system   In Section 4.1.1 it was shown that equation system (4.11) has no solution if one (or more) m_i is equal to 0. This is the case when a new zone is initiated. To get the simulation started, a smaller set of equations are used in the first simulation step. Combining the two rows in (4.11) that describe the behaviour of zone i by eliminating dT_i gives

$$(d_i - b_i)\, p\, dV_i + (a_i d_i - b_i c_i)\, dp =$$
$$- b_i\, dQ_i + b_i \sum_j (h_{ij} - h_i)\, dm_{ij} + (d_i - b_i) \sum_j R_i T_i dm_{ij} \quad (4.19)$$

Knowing that

$$\frac{d_i - b_i}{m_i} = c_{p,i}$$

$$\frac{a_i d_i - b_i c_i}{m_i} = 0, \quad m_i \to 0^+ \quad (4.20)$$

$$h_{ij} = h_i, \qquad m_i \to 0^+$$

and assuming that $dQ_i = 0$, equation (4.19) can be rewritten to

$$p\, dV_i = R_i T_i \sum_j dm_{ij} \quad (4.21)$$

The two rows for zone i in the equation system are now replaced with (4.21). This results in a solvable system with $2N$ equations.

The temperature of the zone in the next simulation step is received by the other state variables together with the ideal gas law.

4.2.2   Ill-conditioned $\mathbb{A}$ matrix—Adaptive scaling

There are large differences in magnitudes between the elements in the $\mathbb{A}$ matrix, since the pressure and temperature values are much greater than the volume and mass values. This makes scaling of the state variables necessary. By a fixed scaling, the equation system will be solvable in most cases, but there is still a risk of getting a matrix that is so badly conditioned that the numerical solution to $\mathbb{A}x = \mathbb{B}$ will be highly unreliable. A better way to handle this is to use a scaling that adapts to the size of the state variables.

The pressure and temperatures change with about the same speed, and the volume and mass in each zone are highly correlated. An example of a feasible scaling is therefore

$$
\begin{array}{llll}
p' & = s_p p & dp' & = s_p\, dp \\
T' & = s_p T & dT' & = s_p\, dT \\
V_i' & = s_i V_i & dV_i' & = s_i\, dV_i \\
m_i' & = s_i m_i & dm_i' & = s_i\, dm_i
\end{array}
\quad (4.22)
$$

where s_p and s_i are scaling factors determined in such a way that $p' = 1$ and $m_i' = k_i$, $i = 1, 2, \ldots, N$, in each step. It can be shown that using this scaling

has the same effect as multiplying the left hand side of each row in equation system (4.11) except the very first, with a scaling factor $(s_p s_i)$. The rows in $\mathbb{B}$ are therefore to be multiplied with the same scaling factors. The first row of the equation system is rewritten in the following way:

$$\sum_{i=1}^{N} \frac{1}{s_i} dV_i' = dV$$

The scaled state variables dx' are determined by solving the resulting equation system $\mathbb{A}' dx' = \mathbb{B}'$. Thereafter, dx' are transformed back to dx.

4.2.3   Finite precision – Exclusion of zones

If a zone is very small, it is difficult for the solver to handle the calculations correctly. For example, the outcome of the calculation of $1 - \epsilon$ is set to 1 even though $|\epsilon| > 0$, if ϵ is a sufficiently small number. One of the consequences is that the mass of a zone might be set to zero even if $m_i \neq 0$.

A zone with no mass is the same as a non-existing zone, and according to Section 4.2.1 the $\mathbb{A}$ matrix is singular. Thus, the equations for the zone have to be excluded from the equation system. This is done by removing the two rows and two columns referring to the zone in the $\mathbb{A}$ matrix, the two rows in the $\mathbb{B}$ vector, and dV_i and dT_i from the list of differentiated state variables in dx.

4.2.4   Accumulated faults – Consistency equations

The model consists of a set of differential equations that has to be solved numerically. There are several methods to do this, but regardless how well the chosen method performs, it will never be completely accurate. Tiny local errors in each step may result in a great relative global fault in the end, if the variable concerned decreases to a small value. A way of avoiding drifting of variables without reducing the time step, is to check the variables consistency and correct them if needed.

By using the ideal gas law, and knowing that the sum of all zone volumes is the same as the cylinder volume, the following equations are derived that can be used to check the consistency

$$
\begin{aligned}
p &= \frac{m_1 R_1 T_1 + \ldots + m_N R_N T_N}{V} \\
V_1 &= \frac{m_1 R_1 T_1}{p} \\
&\vdots \\
V_N &= \frac{m_N R_N T_N}{p}
\end{aligned}
\tag{4.23}
$$

4.3 Usage of model in other phases than the combustion phase

The presented multi-zone combustion model has a structure that is very flexible. With none or minor changes it can be used to describe other phases than the combustion phase. For example, the compression and expansion phase can be simulated by applying the model to a system where the mass transport from the unburned zone (zones) to the burned zone (zones) is set to 0. Since the burned zone does not exist before the ignition, the rows and columns representing this zone are not included in (4.11) during the compression phase. The rows and columns are added to the system at the ignition, and the zone is initiated according to the discussion in Section 4.2.1.

The gas exchange phase can be described with the multi-zone model as well. This can be done by dividing the system into a set of sub-systems, that are represented by physical units like the cylinders and manifolds. The mass transports through the ports are described by dm_{ij}. During the gas exchange phase there is no combustion, but the gas composition will change due to that burned gas leaves the cylinders and are replaced by unburned gas.

4.4 Illustration of concept

To illustrate the simulation procedure, a model of a simple system is implemented and executed. The example is a two-zone system with fixed gas composition, no heat transfer and constant mass.

In this two-zone system, the cylinder gas is divided into two zones; unburned (u) and burned (b) gas. The two zones are considered fully separate, and may therefore have different compositions as well as temperature. The system has only one mass flow; the mass transport from the unburned to the burned zone. The gas is combusted at the moment when it leaves the unburned zone and enters the burned zone, which means that $h_{ub} = h_{bu} = h_u$. Also changes in gas composition due to pressure and temperature are neglected. The gas that enters the burned zone adopts the same composition as the gas already in the zone, which gives that $dR_u \equiv 0$ and $dR_b \equiv 0$.

The multi-zone model can be transformed into the following equation system, consistent with the described two-zone system:

$$\begin{cases} dV_u + dV_b & = dV \\ V_u dp + p\,dV_u - m_u R_u dT_u & = R_u T_u\,dm_{ub} \\ p\,dV_u + m_u c_{v,u}\,dT_u & = (h_{ub} - u_u)\,dm_{ub} \\ V_b dp + p\,dV_b - m_b R_b dT_b & = R_b T_b\,dm_{bu} \\ p\,dV_b + m_b c_{v,b}\,dT_b & = (h_{bu} - u_b)\,dm_{bu} \end{cases} \qquad (4.24)$$

4.4.1   Simulation set-up and initialisation

The two-zone model is implemented and simulated in the crank angle domain. The mathematical tool used in the simulation is MATLAB 5.3. For the numerical solution to the differential equation (4.11) the MATLAB built-in function 'ode15s' is used, which is an implicit ordinary differential equation solver suitable for stiff problems. Chemical properties, such as enthalpy, specific heat and molecular mass, are provided by the chemical equilibrium program package CHEPP (Eriksson, 2004).

   The mass transport from the unburned to the burned gas is

$$\frac{dm_{bu}}{d\theta} = -\frac{dm_{ub}}{d\theta} = (m_u + m_b)\frac{dx_\mathrm{b}}{d\theta} \tag{4.25}$$

where x_b is the mass fraction burned, described by the Wiebe function (Vibe, 1967)

$$x_\mathrm{b}(\theta) = 1 - e^{-a\left(\frac{\theta - \theta_\mathrm{ign}}{\Delta\theta_\mathrm{b}}\right)^{m+1}} \tag{4.26}$$

The ignition angle θ_ign is set to $20°$ before top dead centre. Since the simulation of this two-zone system is only intended to illustrate the simulation procedure, no effort is put on calibrating the model parameters a, m and $\Delta\theta_b$ of the Wiebe function. Instead, approximative values of the flame development angle $\Delta\theta_d$ and the rapid burn angle $\Delta\theta_b$ are used. An initial pressure of 50 kPa is used, and for these conditions the burn angles were found to be $\Delta\theta_d \approx 23°$ and $\Delta\theta_b \approx 17°$ in Eriksson (1999b). The Wiebe parameters are determined from

$$m = \frac{\ln\left(\frac{\ln(1-0.1)}{\ln(1-0.85)}\right)}{\ln\Delta\theta_\mathrm{d} - \ln(\Delta\theta_\mathrm{d} + \Delta\theta_\mathrm{b})} - 1 \tag{4.27}$$

$$a = -\ln(1-0.1)\left(\frac{\Delta\theta}{\Delta\theta_\mathrm{d}}\right)^{m+1} \tag{4.28}$$

   It is also assumed that all fuel becomes completely combusted. The mass fraction burned at exhaust valve opening is therefore $x_\mathrm{b} = 100\%$. Both the heat transfer between the zones and to the surroundings are neglected, as well as the residual gases. The unburned zone contains a stochiometric mixture of iso-octane and air. The burned gas consists of 14.0% H_2O, 12.5% CO_2, and 73.5% N_2. The heat capacity and enthalpy depend solely on temperature and not pressure, which is a consequence of the fixed gas composition assumption.

Simulation procedure   The ode-solver calls the subroutine with values of x, and these are used to calculate $\frac{dx}{d\theta} = \mathbb{A}^{-1}(x)\mathbb{B}(x,\theta)$. The calculation procedure is as follows:

   1. The values of p, T_i and V_i comes from the numerical solver and are used in the calculation of $\mathbb{A}$ and $\mathbb{B}$ $\Rightarrow$ $\mathbb{A}$ and $\mathbb{B}$

2. The equation system (4.24) is scaled adaptively according to the method described in section 4.2.2 $\Rightarrow$ Well-conditioned $\mathbb{A}'$ and $\mathbb{B}'$

3. The equation system is solved by Gaussian elimination $\Rightarrow dx'$

4. Rescaling of $dx' \Rightarrow dx$

5. $\frac{dx}{d\theta}$ is returned to the numerical solver $\Rightarrow x$

6. When the mass of the unburned zone is small, when $(1 - x_b) < 0.05$, the value of the unburned volume is adjusted according to the discussion in Section 4.2.4:

$$V_u = \frac{m_i R_u T_u}{p}$$

Only the unburned zone exists during the compression phase, since no gas has been burned yet. The system of equations that is used to simulate this phase is therefore:

$$\begin{cases} dV_u & = dV \\ V_u dp + p\, dV_u - m_u R_u dT_u & = 0 \\ p\, dV_u + m_u c_{v,u}\, dT_u & = 0 \end{cases} \tag{4.29}$$

In the initial phase of the combustion the burned zone is still non-existing as it has no mass. The calculations are therefore carried out as described in Section 4.2.1. The initial temperature of the burned gas $T_b(\theta_{\mathrm{ign}})$ is determined by solving the equation $h_u(T_u) = h_b(T_b)$.

4.4.2 Simulation results

Figure 4.1 shows the resulting simulated cylinder pressure, together with a measured cylinder pressure trace from an engine with the same geometry as in the simulation. The engine is run at 50 kPa and the ignition angle is 20° before TDC. Naturally, there is a discrepancy between the two curves, since the simulated system contains many simplifications and that the model parameters are not calibrated to the measured pressure trace. The difference is however only one or a few bar despite all the simplifications.

At 150° after TDC, there is a pressure drop in the measured curve due to the blow down. This phase is not included in the simulation model, and therefore the pressure remains fairly constant at this angle. Figure 4.2 shows the two simulated temperatures. At about 50° after TDC, the mass of the unburned zone is so small that numerical operations can not be carried out correctly, as discussed in subsection 4.2.3. At this point, the two equations for the unburned zone are removed from equation system (4.24), leaving the equation system with only three equations—one of them being the trivial $dV_b = dV$.
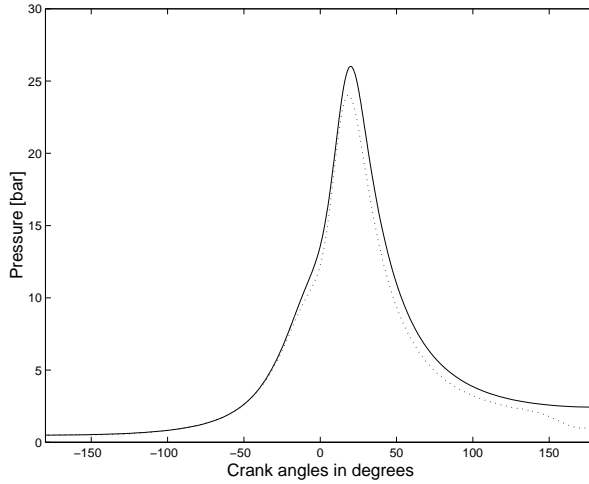
Figure 4.1: Cylinder pressure as function of crank angle. The solid line shows the result from the simulation, and the dashed line measured data from a SAAB 2.3 l naturally aspirated engine with compression ratio $r_c = 10.1$.
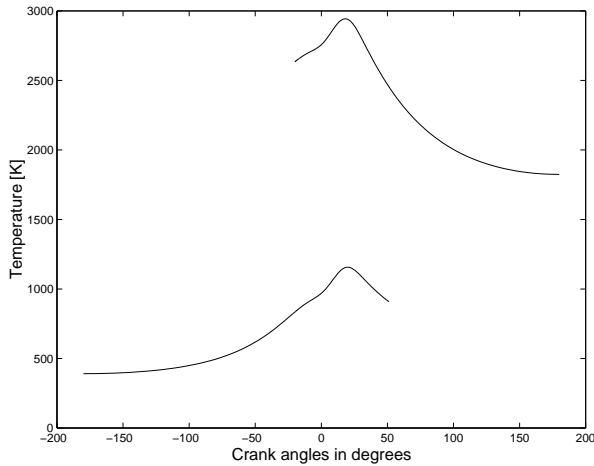
Figure 4.2: Simulation results showing burned (upper curve) and unburned gas temperatures as function of crank angle. Inlet manifold pressure was set to 50 kPa, residual gas fraction to 7% and ignition angle to 20° before TDC. The cylinder gas consists of a mixture of air and iso-octane, with normalised air-fuel ratio $\lambda = 1$. At about 50° after TDC, the unburned zone is treated as non-existing.
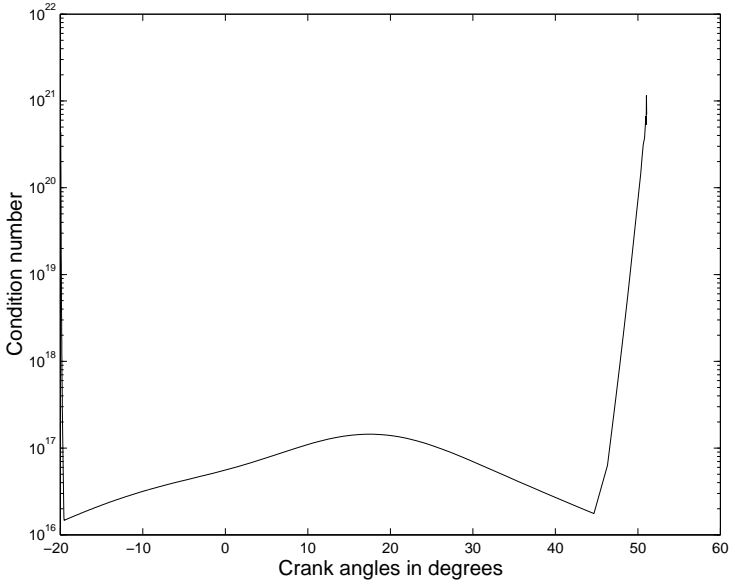
Figure 4.3: Condition number for the unscaled $\mathbb{A}$ matrix.

The importance of the adaptive scaling   The outcome of the simulation is used to illustrate the effectiveness of the adaptive scaling. Without any kind of scaling, the condition number for the $\mathbb{A}$ matrix is 10^{16} or greater, which is shown in Figure 4.3. The condition number is very high in the beginning of the combustion simulation, caused by the small value of m_b. The local maximum at $20°$ after TDC coincide with the pressure maximum. In the end of the combustion, the condition number increases rapidly again, since the mass of the unburned fuel $m_u \to 0$.

In Figure 4.4, the $\mathbb{A}$ matrix has been scaled adaptively. According to Section 4.2.2, the scaling factors should be chosen such that the pressure after scaling is $p' = 1$ and the mass $m_i' = k_i$. Four different combinations of k_i are investigated

- $k_u = k_b = 1$

- $k_u = R_u$ and $k_b = R_b$

- $k_u = c_{v,u}$ and $k_b = c_{v,b}$

- $k_u = k_b = 3000$

The results show that choosing $k_i = 1$ yields a significant reduction compared to the unscaled system. The condition number stays beneath $5 \cdot 10^7$ during the whole simulation. The choice $k_i = R_i$, which makes the b_i' values of the $\mathbb{A}$
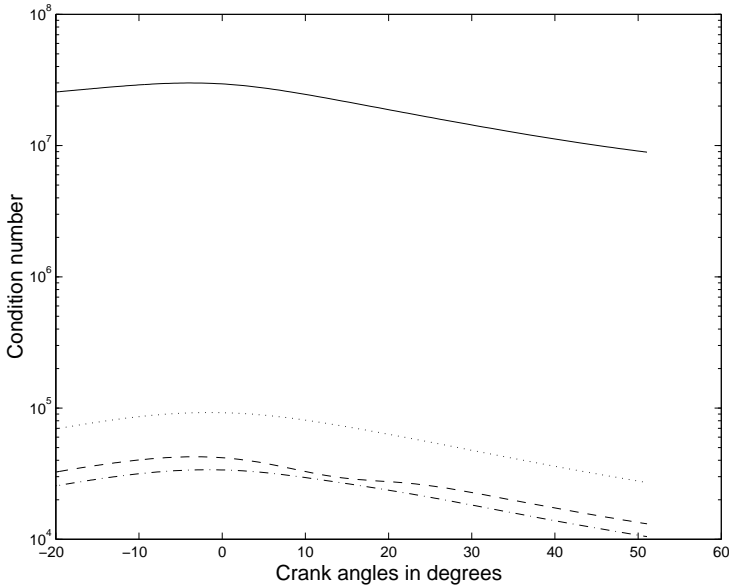
Figure 4.4: Condition number for the $\mathbb{A}$ matrix after being scaled adaptively with $k_u = k_b = 1$ (solid line), $k_u = R_u$ and $k_b = R_b$ (dotted), $k_u = c_{v,u}$ and $k_b = c_{v,b}$ (dash-dotted), and $k_u = k_b = 3000$ (dashed).

matrix equal to one, results in a greater reduction. The condition number is now less than 10^5. An even greater improvement is achieved by letting $k_i = c_{v,i}$, which makes the d_i values equal to one. For this choice of k_i the condition number stays beneath $5 \cdot 10^4$. In the two latter cases k_i has to be updated each simulation step, since the temperature and pressure changes during the simulation. However, almost as good result as for $k_i = c_{v,i}$ is achieved by the choice $k_u = k_b = 3000$.

4.5   Applications utilising the presented model

Up until now the presentation and discussion have covered the basic principles and properties of the presented modelling methodology. In particular it was shown how: 1) the $\mathbb{A}$ matrix should be scaled to preserve numerically tractable properties, 2) new zones can be initialised, 3) empty or small zones are removed and 4) how the conservation equations can be used to track and adjust the numerical errors. This shows that the modelling methodology is promising but the practical applicability must also be proved. This is done by referring to studies where this modelling methodology has been successfully applied.

The presented formulation of multi-zone models has been utilised in other

scientific works. The first three applications listed below track focus on the use of the multi-zone model during the closed part of the engine cycle, while the last one also includes the gas exchange phase.

- Brand (2005) uses the methodology to get a two zone model for NO_x prediction in SI engines.

- One sequence of applications of the modelling methodology has been directed towards investigations of ion current. Gill (2003) uses the methodology to create an object oriented simulation environment for multi-zone models where the number of zones are dynamically added to the system as the combustion progresses. Setups of up to 35 different zones were successfully implemented and tested. Claesson (2004) extends the work of Gill and uses the model structure to study the influence of different modelling assumptions on ion currents. Cedersund (2004) continues the work and contributes with and analysis of the influence of heat transfer close to the vicinity of the spark plug and its influence on the ion current.

- Nilsson and Eriksson (2004) uses the methodology for simulating motored engine cycles of the SVC engine.

- The papers (Öberg and Eriksson, 2006a,b, 2007) use the modelling methodology to investigate the gas exchange phase for variable valve timing engines. A two zone model is implemented for the high pressure part of the engine cycle, and in the gas exchange phase more zones are added to the cylinder for enabling an efficient bookkeeping of fresh gases, residual gases, and back flows.

These listed applications contribute by showing the applicability of the presented methodology.

4.6 Conclusions

A new formulation of zero-dimensional multi-zone models is presented. The formulation has a clear and simple structure which enables the user of the model to easily add and remove zones while maintaining the structure. A number of important issues that can give problems when simulating the model are also treated.

One issue is the initialisation of a new zone. The most significant example of initialisation is the initiation of the burned gas zone. It is shown how the state of the gas can be initiated in two steps, simply by studying the equations for the zone. Another issue arise due to the large differences in magnitude between the variables. This can result in numerical problems when simulating the system on a computer with finite precision. It is shown that the numerical difficulties can be avoided by proper scaling of the variables. The final issue is how faults, accumulated during the simulation, can be reduced by utilising

a set of consistency equations. For each zone one consistency equation can be formulated using the ideal gas law.

The concept is illustrated by the simulation of a simple two-zone system. The simulation is also used to indicate the strength of the adaptive scaling.

A list of scientific works shows that the methodology has been successfully applied in various applications.

TORQUE MODEL FOR A VARIABLE COMPRESSION ENGINE

This chapter is based on Nilsson et al. (2006a), Nilsson et al. (2006b), and Nilsson et al. (2008).

I_n the first chapter of this thesis it was concluded that the fuel optimal combination of compression ratio, ignition angle and air can be determined by separately maximising the engine torque for compression ratio and ignition angle at constant air mass flow, and then adjusting the air mass flow to achieve the requested torque. A change in compression ratio and ignition angle that leads to a higher torque always permits a decrease in air mass flow, and thereby the fuel consumption. As a result, a control oriented model for the engine torque is here developed by compiling a set of sub-models related to well-known physical and empirical relations.

This chapter contains a combined version of the publications Nilsson et al. (2006a), Nilsson et al. (2008), and Nilsson et al. (2006b). A model for the indicated mean effective pressure (IMEP) was first derived in Nilsson et al. (2006a). Such a model had never before been compiled and validated for variable compression engines. The IMEP model made it possible to determine the optimal combination of compression ratio and ignition angle for a given air mass flow, but not the resulting reduction in air mass flow. The parameters were identified for the OR95 data set, and the model was validated on the same data set.

The development of the IMEP model was continued in Nilsson et al. (2008) by improving the sub-model for the ignition timing efficiency. All model parameters were re-identified, but this time for the OR99 data set. The reason for choosing this data set was that the knock free region included more data around the maximum brake torque compared to the OR95 data set, which allowed for a higher accuracy in the estimation of the ignition timing efficiency parameters. The OR95 data set was then used in the validation of the IMEP model.

A model for the friction and compressor losses was added to the IMEP model in Nilsson et al. (2006b), and this made the torque model complete. The torque model made it possible to run an optimisation in all the three dimensions: compression ratio, ignition angle and air mass flow.

This chapter begins by showing results from the measurements. Engine torque contours contribute by showing how the torque depends on compression ratio and ignition angle. The IMEP model is then derived and validated. The optimal compression ratio and ignition angle are determined from the IMEP model. Next, a combined model for friction and the compressor losses are derived. The model is valid in the region where there is no or weak knock.

The aim of this work is to find a simple but powerful static torque model that provides the controller with reference values. Therefore, the final validation is a study of how much the engine efficiency at the model based reference values for compression ratio and ignition angle deviates from the actual maximum efficiency.

This work contributes by showing that this model is capable of describing the torque from a variable compression engine. Furthermore the torque model is also capable of handling different fuel qualities; the model is first tuned to a 99 octane fuel and subsequently validated and shown to hold also for a 95 octane fuel.
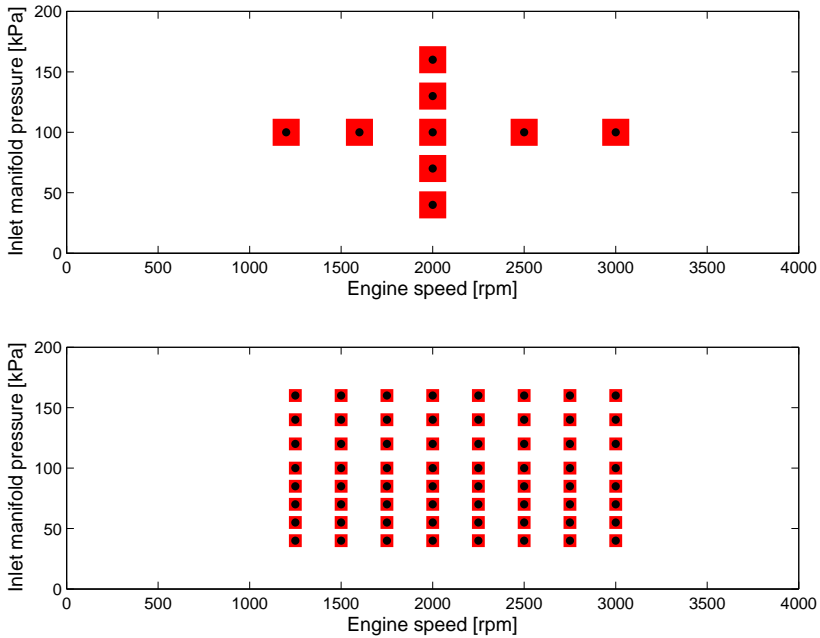
Figure 5.1: Speed and load points included in the investigation. Here the load is specified using the intake manifold pressure, since the torque will vary with ignition angle and compression ratio. Two types of data sets were collected. With both OR99 and OR95 fuel, data was collected in the 9 different speed and load points shown in the top figure. In each speed and load point several measurements were made for different combinations of compression ratio and ignition angle. Data was also collected in an 8x8 matrix for the OR99 fuel (bottom plot).

5.1 Measurements

The three data sets that are used in this investigation are the OR95, OR99, and 8x8 data sets. These are described in Appendix B, and include the speed and load points that are shown in Figure 5.1.

The OR99 data set is used for identifying the parameters in the indicated mean effective pressure part of the torque model, the 8x8 data set is used for parameter identification in the friction mean effective pressure (FMEP) model, and the OR95 data set is used for validating the resulting torque model.

5.1.1 Torque contours

Figure 5.2 shows torque contours for 4 different speed and load points. It can be seen that the efficiency increases with increasing compression ratio in most
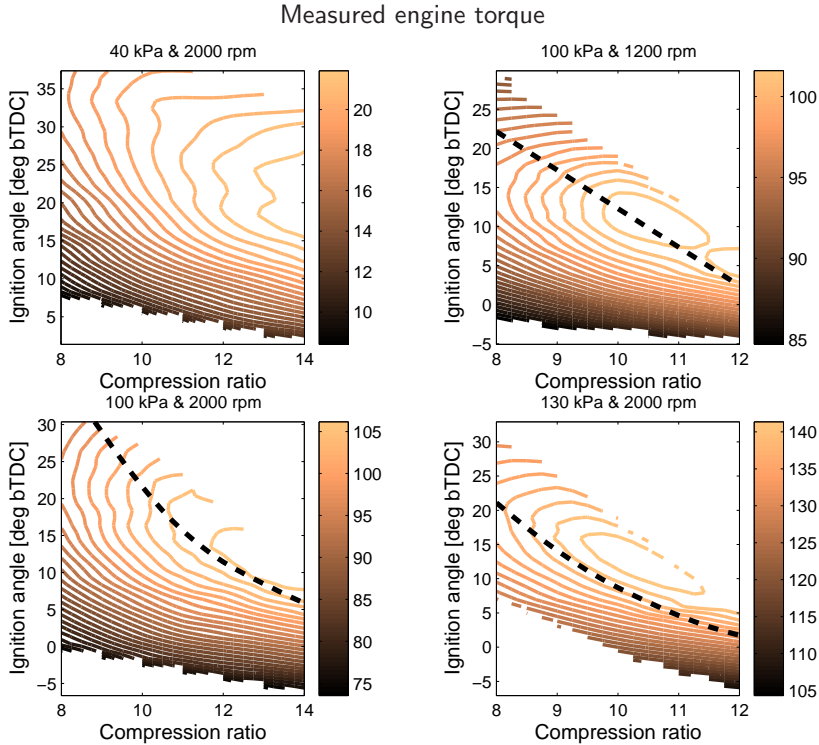
Figure 5.2: Contour plots of the measured output torque [Nm]. The knock intensity limit, defined in Section 5.1.2, is shown with a dashed line. The regions to the left and below the line is called the feasible region. In most cases the output torque increases with compression ratio, but as seen in the two rightmost figures, knock counteracts this increase and the fuel optimal compression is achieved at $r_c < 14$. (Data set: OR95)

cases. But in other cases this effect is counteracted by knock. The loss in efficiency at knocking conditions is caused by increased heat transfer due to increased convection (Grandin, 2001). An interesting observation is that even if the potentially harmful and disturbing characteristics of knock is not taken into account, the highest compression ratio is still not the best choice of reference values to the controller in some speed and load points.

The plots represent conditions with constant inlet manifold pressure and engine speed, while in the optimisation formulation (1.6) the air mass flow should be the property that is held constant when choosing compression ratio and ignition angle. However, the measurements show that for constant engine speed and inlet manifold pressure, the air mass flow is also constant (see Section 5.2.1).

5.1.2 Knock intensity

Knock intensity is here defined as the maximum signal energy in a moving window of length L samples. The measure is based on the definition of knock intensity in Kiencke and Nielsen (2000). To find the knock intensity, the cylinder pressure is first filtered through a high pass filter, $p_{cyl,HP}$, and the intensity measure is then applied:

$$I_{knock} = \frac{1}{N_{cycles}} \sum_{1}^{N_{cycles}} \left(\max_t \frac{1}{L} \sum_{k=t-L+1}^{t} p_{cyl,HP}^2[k] \right) \tag{5.1}$$

where N_{cycles} is the the number of measured cycles in an operating point. The window length is set to $L = 25$ samples. The frequency of the fundamental mode of the knock signal is about 7–8 kHz for the SVC engine, which means that the window length is set to about 2.5 knock oscillation periods.

Knock intensities for 4 different speed and load points are shown in Figure 5.3. Similar behaviours are exhibited in the remaining speed and load points — the intensity remains at the same level in an ignition angle region, followed by a sudden sharp rise when the spark timing is advanced. The intensity limit I_{limit} is set to $0.1 \cdot 10^9$ [Pa^2]. This is motivated by that the knock intensity is low at this limit, and that the derivative of the knock intensity with respect to ignition angle is high.

Of the 388 measured operating points at OR95, 280 have a knock intensity lower than $0.1 \cdot 10^9$ [Pa^2], and are therefore judged to be in the feasible region. The OR99 data set includes 352 operating points, of which 246 have a knock intensity level below the limit. All of the operating points in the 8x8 data set are in the feasible region.

5.2 Engine torque model

We now turn to the torque model which consists of three components; gross indicated work W_{ig}, pumping work W_{pump}, and friction work W_{fric}. The brake torque is expressed as follows

$$M = \frac{W_{ig} - W_{pump} - W_{fric}}{2\pi n_r} \tag{5.2}$$

where n_r is the number of revolutions per engine cycle. For a four stroke engine n_r is equal to 2. The gross indicated work is the work produced in the high pressure part of the cycle. The pumping loss accounts for the work that is consumed during the gas exchange phase, and the friction work accounts for friction losses in the piston rings and bearings and the compressor losses. The next step is to derive models for these three components. In this section, models for the gross indicated work and pumping losses are presented, while the friction model is discussed in Section 5.4. The model parameters are identified for the OR99 data set.
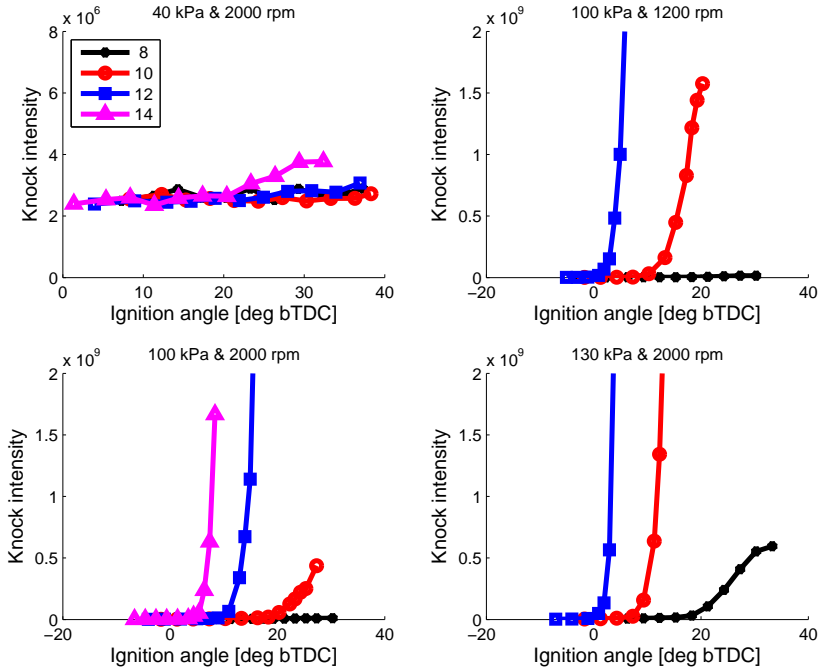
Figure 5.3: Knock intensity as function of ignition angle for four different speed and load points. The intensities are shown for different compression ratios. It is clearly seen that the intensity increases with higher compression ratios and earlier ignition. At $\{100 \text{ kPa}, 1200 \text{ rpm}\}$ and $\{130 \text{ kPa}, 2000 \text{ rpm}\}$ the knock intensity at $r_\mathrm{c} = 14$ is of such magnitude that the measurements have been terminated already at $r_\mathrm{c} = 12$. (Data set: OR95)

5.2.1 Pumping losses

The pumping losses during an engine cycle are approximately

$$W_\mathrm{pump} = V_\mathrm{D} \left(p_\mathrm{em} - p_\mathrm{im} \right) \tag{5.3}$$

Measured pumping losses are calculated from the measured cylinder pressure trace

$$W_\mathrm{pump} = - \int_{V_{180°}}^{V_{540°}} p_\mathrm{cyl} \, dV \tag{5.4}$$

and these are shown in Figure 5.4. It can be seen that the change in PMEP as function of p_im is linear, but due to the moment of inertia of the moving gas and cylinder-to-cylinder interaction, the decrease in PMEP is less than what is predicted by (5.3). Therefore, the following model is proposed

$$W_\mathrm{pump} = V_\mathrm{D} \left(p_\mathrm{em} - k_\mathrm{pp} \, p_\mathrm{im} - k_\mathrm{p0} \right) \tag{5.5}$$
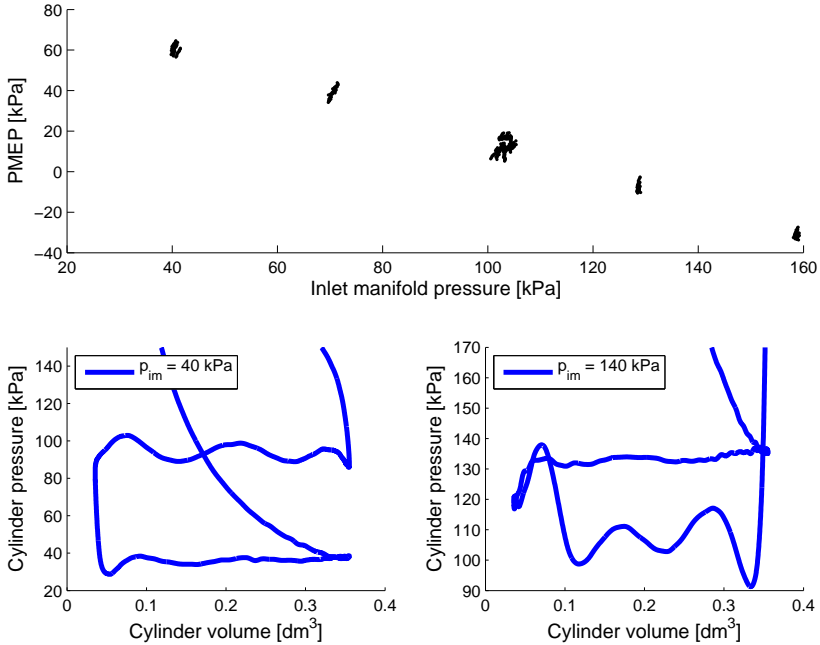
Figure 5.4: Top figure: Measured PMEP as function of measured inlet manifold pressure. Bottom figure: Cylinder pressure during the gas exchange phase ($N = 2000$ rpm). Due to the moment of inertia of the moving gas and cylinder-to-cylinder interaction, the enclosed area in (5.4) differs from $V_{\mathrm{D}}(p_{\mathrm{em}} - p_{\mathrm{im}})$. By looking at the cylinder pressure traces at both high and low loads, it can be seen that at high loads some area is lost around TDC (near exhaust valve closing) compared to at low loads.

The parameters k_{pp} and k_{p0} are identified for the SVC engine with the least squares method (LSQ) to

$$
\begin{aligned}
k_{\mathrm{pp}} &= 0.83 \quad [\mathrm{Pa\ s/kg}] \\
k_{\mathrm{p0}} &= 6.9 \cdot 10^{3} \quad [\mathrm{Pa}]
\end{aligned}
$$

There is a relation between inlet manifold pressure and air mass flow, which is described in Hendricks et al. (1996)

$$
\begin{aligned}
\dot{m}_{\mathrm{air}} &= \frac{V_{\mathrm{D}} N \eta_{\mathrm{vol}}}{R\, T_{\mathrm{im}} n_{\mathrm{r}}} p_{\mathrm{im}} \\
\eta_{\mathrm{vol}} p_{\mathrm{im}} &= a_1\, p_{\mathrm{im}} + a_0
\end{aligned}
$$

These two equations are compiled to the following model for p_{im}

$$p_{im}(\dot{m}_{air}, N, T_{im}) = \frac{1}{a_1} \left(\frac{n_r R T_{im}}{V_D N} \dot{m}_{air} - a_0 \right) \qquad (5.6)$$

The inlet manifold temperature depends on operating point. In the OR99 data set the temperature span is 305–340 K. Since a small error in T_{im} is expected to have only a small effect on the calculated torque (5.2), the inlet manifold temperature is set constant. Its value is set to 320 K, which is the mean value of the OR99 data set. The parameters a_0 and a_1 are identified with LSQ to

$$\begin{aligned}
a_1 &= 0.89 \\
a_0 &= -9.0 \cdot 10^3 \quad [Pa]
\end{aligned}$$

A validation of the model against measurements is shown in the top plot of Figure 5.5. It can be seen that model (5.6) describes the inlet manifold pressure with high accuracy. The root mean square error (RMSE) between model and measurements is only 1.4 kPa.

A model for the exhaust manifold pressure based on air mass flow is presented in Eriksson et al. (2002), where the pressure difference over the manifold is proportional to the quadratic function of the air mass flow. This gives the following model:

$$p_{em} = b_2 \dot{m}_{air}^2 + b_0 \qquad (5.7)$$

where b_0 is the ambient pressure. As there is no information about the ambient pressure in the data sets, the parameter b_0 is here treated as an empirical constant. The model parameters b_0 and b_2 are identified with LSQ to

$$\begin{aligned}
b_2 &= 4.63 \cdot 10^6 \quad [Pa\ s^2/kg^2] \\
b_0 &= 102 \cdot 10^3 \quad [Pa]
\end{aligned}$$

A comparison between the model and measurements is shown in the bottom plot of Figure 5.5, where the RMSE is 0.72 kPa.

Equations (5.5), (5.6) and (5.7) give the resulting model for the pumping losses

$$W_{pump} = V_D \left(b_2 \dot{m}_{air}^2 - k_{pp} \frac{R T_{im} n_r}{a_1 V_D N} \dot{m}_{air} - \left(k_{p0} + b_0 - \frac{a_0}{a_1} \right) \right) \qquad (5.8)$$

A comparison between measured and modelled pumping losses is shown in Figure 5.6, where the resulting RMSE for PMEP is 2.5 kPa. This error can be considered small compared to the IMEP levels in the engine operating range where knock is a limitation, see for example Figure 5.10.
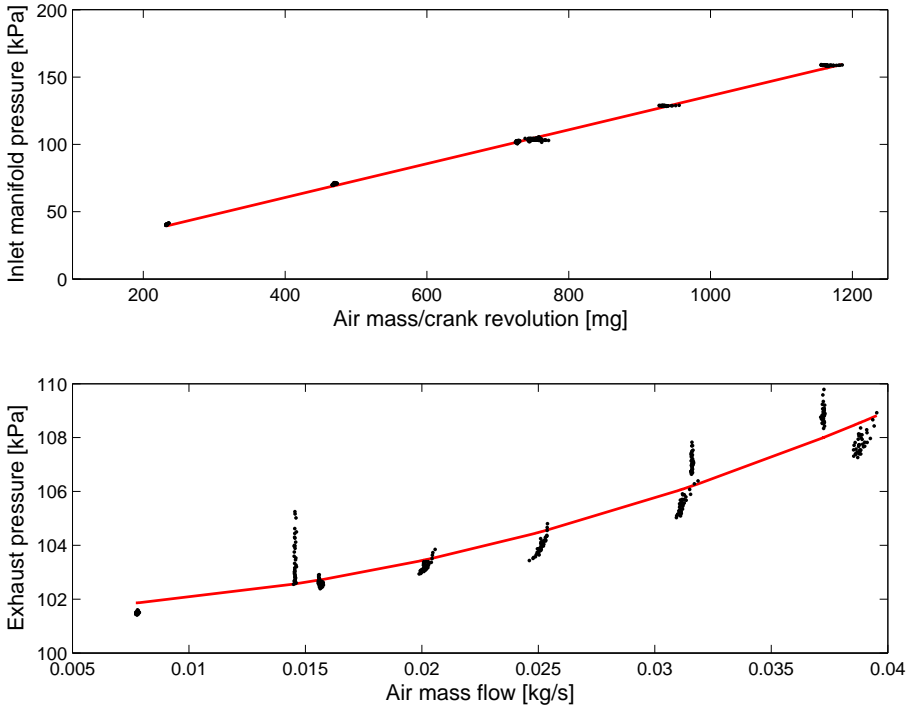
Figure 5.5: Top: Inlet manifold pressure model (5.6). Bottom: Exhaust manifold pressure model (5.7). The dots show the individual measurements and the line represents the model. The number of samples is 352. (Data set: OR99)
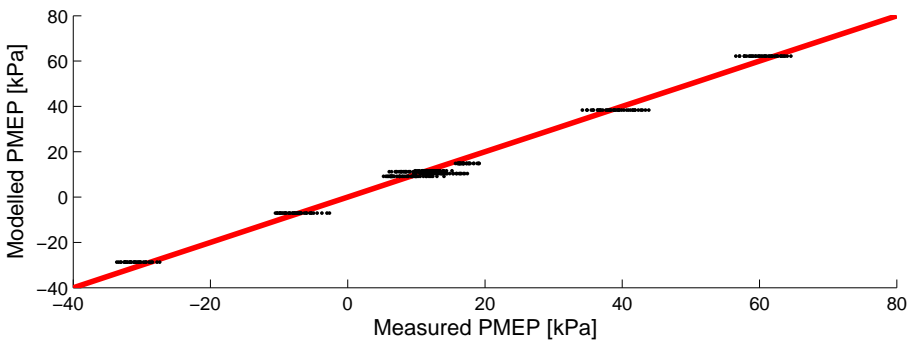
Figure 5.6: Modelled pumping losses (5.8) versus measured pumping losses (5.4). The data set used is OR99, and the number of data points is 352.

5.2.2 Gross indicated work

The gross indicated work during one engine cycle is modelled as the product between the amount of chemical energy delivered by the fuel and the gross indicated efficiency $\tilde{\eta}_{ig}$

$$W_{ig} = m_{fuel}\, q_{HV}\, \tilde{\eta}_{ig}(N, p_{im}, \theta_{ign}, r_c) \tag{5.9}$$

The gross indicated efficiency can be further developed as the efficiency of an ideal Otto cycle (Moran and Shapiro, 1998), expanded with ignition timing efficiency and losses in the combustion chamber.

$$\tilde{\eta}_{ig} = \left(1 - \frac{1}{r_c^{\gamma-1}}\right) \eta_{ig,ch}\, \eta_{ign}(\theta_{ign}) \tag{5.10}$$

where $\eta_{ig,ch}$ denotes the combustion chamber efficiency. These efficiency losses are mainly heat transfer, incomplete combustion and crevice effects. Deviations in ignition timing from MBT are included in the ignition timing efficiency η_{ign}.

In Figure 5.7 the product $\eta_{ig,ch}\, \eta_{ign}$ is shown. The product between the efficiencies is determined from measurements by

$$\eta_{ig,ch}\, \eta_{ign} = \frac{W_{in} - W_{pump}}{m_{fuel}\, q_{HV} \left(1 - \frac{1}{r_c^{\gamma-1}}\right)} \tag{5.11}$$

where W_{in} is the net indicated work

$$W_{in} = \oint p_{cyl}\, dV \tag{5.12}$$

and the pumping losses are calculated using equation (5.8). The fuel parameters q_{HV} and γ, as well as $(A/F)_S$ in (1.4), are unknown and can not be identified from the measurements. Instead properties of iso-octane is used

$$
\begin{aligned}
q_{HV} &= 44.6 \quad [\text{MJ/kg}] \\
\gamma &= 1.3 \\
(A/F)_S &= 15
\end{aligned}
$$

It can be observed from Figure 5.7 that the curves follow about the same path as long as there is no knock, even though the different compression ratios are shown in each speed and load point. The operating point that has the highest spread is the low load point at 40 kPa, where there is a small deviation between the curves. This operating point has the highest margin to the knock limit. When knock is present, the increased heat transfer counteracts the better phasing of the cylinder pressure curve. This can be seen in the figure, especially at the speed and load point $\{100\ \text{kPa}, 2000\ \text{rpm}\}$. It should be noted that the load point at 40 kPa is actually not in the scope of this work, due to its low knock intensity. As stated in Section 1.5, at loads where the optimal choice of
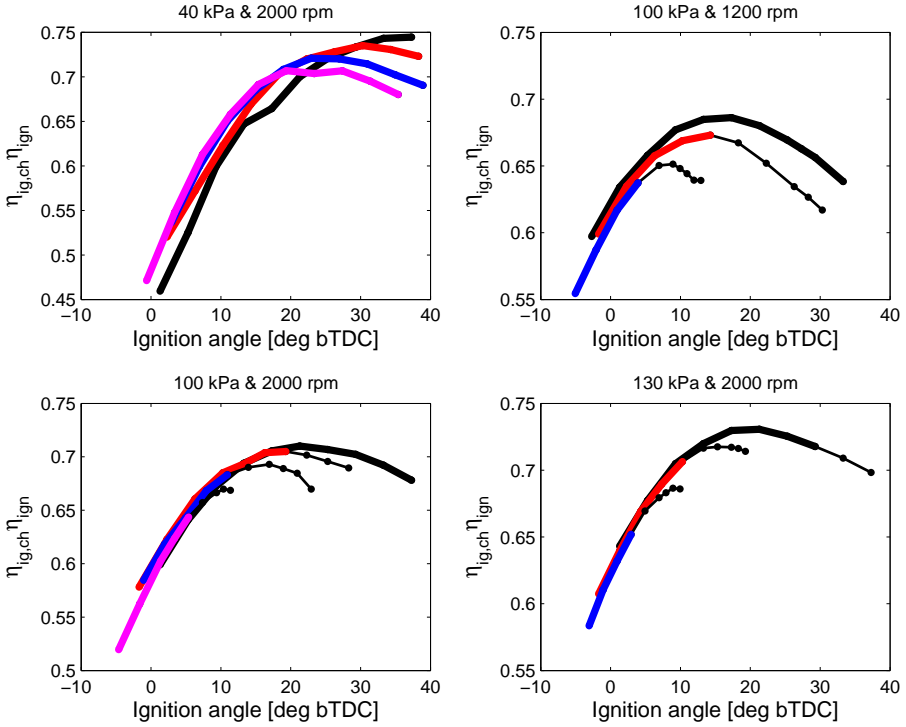
Figure 5.7: $\eta_{\mathrm{ig,ch}}\,\eta_{\mathrm{ign}}$ curves. The curves include data from the different compression ratios ($r_{\mathrm{c}} = 8, 10, 12, 14$). Data from operating points with knock intensities greater than I_{limit} are marked with thin lines and dots. The curves follow approximately the same path in each speed and load point, as long as there is no knock. But when knock is present in a curve, it deviates from the others due to the higher amount of heat transfer. (Data set: OR99)

compression ratio is the maximum possible irrespectively of ignition angle, a conventional maximum brake torque controller can be used. Nevertheless, this load point is included in this work since it is interesting to see if the torque model is valid also for low loads.

The curve shape of the ignition timing efficiency can be described with a third order polynomial of $\theta_{\mathrm{ign}} - \theta_{\mathrm{opt}}$, where θ_{opt} is the optimal ignition for non-knocking conditions

$$\eta_{\mathrm{ign}} = 1 - C_{\mathrm{ign},2}\,(\theta_{\mathrm{ign}} - \theta_{\mathrm{opt}})^2 + C_{\mathrm{ign},3}\,(\theta_{\mathrm{ign}} - \theta_{\mathrm{opt}})^3 \qquad (5.13)$$

The parameters $C_{\mathrm{ign},2}$ and $C_{\mathrm{ign},3}$ are determined by solving a linear least square

problem to

$$
\begin{aligned}
C_{\mathrm{ign},2} &= 0.25 \cdot 10^{-3} \quad [\mathrm{deg}^{-2}] \\
C_{\mathrm{ign},3} &= 5.1 \cdot 10^{-6} \quad [\mathrm{deg}^{-3}]
\end{aligned}
$$

According to the discussion in Section 1.4.1, the model has to be valid only in the region where the knock intensity is $\leq I_{\mathrm{limit}}$. Therefore, only operating points with knock intensities lower than $0.1 \cdot 10^9$ Pa^2 are used in the parameter estimation. The combustion chamber efficiency $\eta_{\mathrm{ig,ch}}$ is assumed to be constant, and is identified to

$$
\eta_{\mathrm{ig,ch}} = 0.72
$$

By studying the first and second derivative of (5.13) it can be seen that θ_{opt} is indeed the maximum of (5.13). Solving $\frac{\mathrm{d}\eta_{\mathrm{ign}}}{\mathrm{d}\theta_{\mathrm{ign}}} = 0$ gives that $\theta_{\mathrm{ign}} = \theta_{\mathrm{opt}}$ is one of two solutions. The second derivative at this ignition angle is

$$
\frac{\mathrm{d}^2 \eta_{\mathrm{ign}}}{\mathrm{d}\theta_{\mathrm{ign}}^2}(\theta_{\mathrm{opt}}) = -2C_{\mathrm{ign},2} < 0
$$

which tells that θ_{opt} is the maximum.

The optimal spark timing θ_{opt} in (5.13) depends on the speed and load point. A simple model for the optimal ignition is

$$
\theta_{\mathrm{opt}} = c_0 + c_{p_{\mathrm{im}}} \frac{1}{p_{\mathrm{im}}} + c_N N \quad [\mathrm{deg\ bTDC}] \tag{5.14}
$$

The model parameters are identified with LSQ to:

$$
\begin{aligned}
c_0 &= 5.62 \quad [\mathrm{deg}] \\
c_{p_{\mathrm{im}}} &= 5.4 \cdot 10^5 \quad [\mathrm{deg} \cdot \mathrm{Pa}] \\
c_N &= 0.28 \quad [\mathrm{deg} \cdot \mathrm{s}]
\end{aligned}
$$

which results in an RMSE of 0.46°. A comparison between the model and the estimated values are shown in Figure 5.8. Finally, Figure 5.9 shows how well the $\eta_{\mathrm{ig,ch}}\,\eta_{\mathrm{ign}}$ model, including (5.13) and (5.14), describes the measured data.

5.3   Validation of the model for indicated work

The torque model will now be validated on the OR95 data set. A validation of the model for the indicated work is shown in Figure 5.10. The indicated mean effective pressure used in the figure is defined as

$$
\mathrm{IMEP} = \frac{W_{\mathrm{ig}} - W_{\mathrm{pump}}}{V_{\mathrm{D}}}
$$
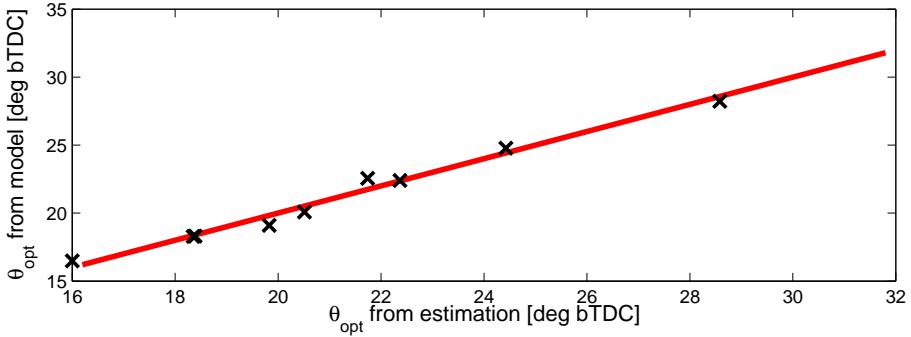
Figure 5.8: Validation of optimal ignition angle model for non-knocking conditions. The crosses represent the optimal ignition given by the model, versus the optimal ignition estimated on the measurement data. Ideally, the crosses should be placed on the straight line $(\theta_{\mathrm{opt}})_{\mathrm{model}} = (\theta_{\mathrm{opt}})_{\mathrm{estim}}$, also shown in the figure. The number of speed and load points used in the parameter estimation is 9. (Data set: OR99)

Table 5.1: RMSE for the inlet manifold pressure, exhaust manifold pressure, optimal ignition angle, PMEP and IMEP.

	RMSE OR99	RMSE OR95
p_{im}	1.4 kPa	2.4 kPa
p_{em}	0.72 kPa	1.8 kPa
θ_{opt}	0.46°	0.37°
PMEP	2.5 kPa	3.2 kPa
IMEP	24 kPa	27 kPa

The figure shows that the modelled IMEP curves coincide well with the measurements. The root mean square errors (RMSE) for the different sub-models are shown in Table 5.1. The RMSE for the OR99 data set are included in the table as a comparison, and it can be seen that the values are in the same range for both data sets.

To investigate if there are any systematic deviations between model and measurements, the correlation coefficient is studied. The correlation coefficient is defined as:

$$\rho(X,Y) = \frac{Cov(X,Y)}{\sigma(X)\sigma(Y)}$$

where σ denotes standard deviation. Let ΔIMEP be the deviation between model and measurements, that is

$$\Delta\mathrm{IMEP}(r_{\mathrm{c}}, \theta_{\mathrm{ign}}) = \mathrm{IMEP}_{\mathrm{mod}}(r_{\mathrm{c}}, \theta_{\mathrm{ign}}) - \mathrm{IMEP}_{\mathrm{meas}}(r_{\mathrm{c}}, \theta_{\mathrm{ign}}) \qquad (5.15)$$

The measured IMEP at the compression ratio r_{c} and ignition angle θ_{ign} is
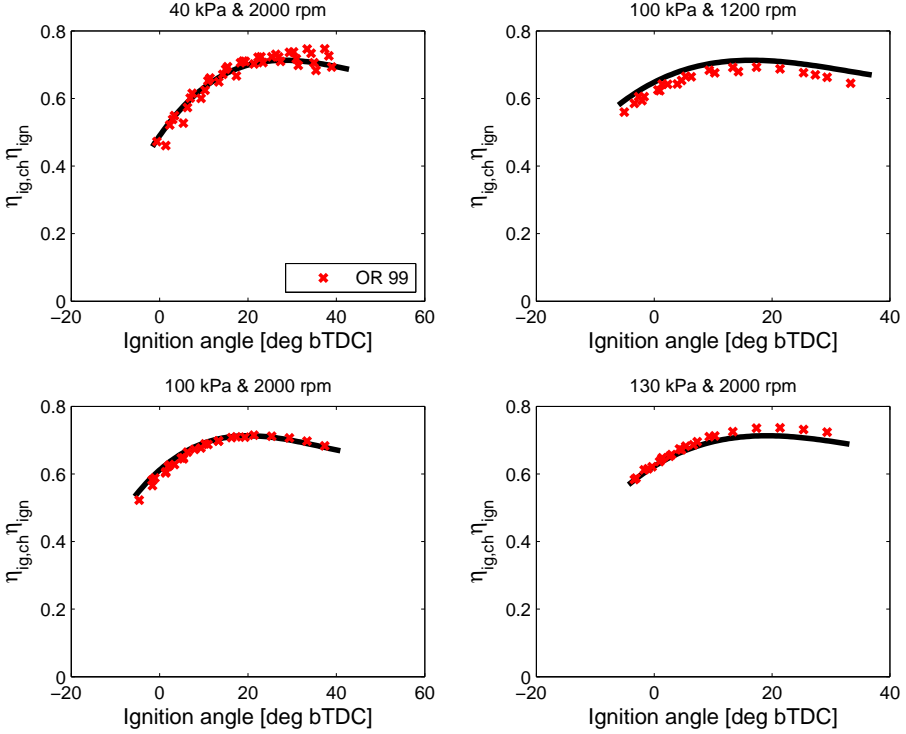
Figure 5.9: Validation of the $\eta_{\mathrm{ig,ch}}\,\eta_{\mathrm{ign}}$ model. The model is represented by the thick line, and $\eta_{\mathrm{ig,ch}}\,\eta_{\mathrm{ign}}$ from the measurements are marked with x. Only samples with sufficiently low knock intensities are shown. (Data set: OR99)

determined by linear interpolation. The correlation coefficients for $\Delta\mathrm{IMEP}$ are then:

$$
\begin{aligned}
\rho(p_{\mathrm{im}}, \Delta\mathrm{IMEP}) &= -0.05 \\
\rho(N, \Delta\mathrm{IMEP}) &= -0.59 \\
\rho(r_{\mathrm{c}}, \Delta\mathrm{IMEP}) &= 0.18 \\
\rho(\theta_{\mathrm{ign}}, \Delta\mathrm{IMEP}) &= -0.39
\end{aligned}
$$

This means that the model overestimates the output torque at low engine speeds and underestimates it at high engine speeds. The correlations are small with the smallest values for p_{im} and r_{c}, while N has the largest correlation. Taking into consideration that the model error is small and that N is constant during the optimisation, this higher correlation for N does not cause problems when searching for the optimal combination of compression ratio and ignition timing. This is further supported when studying the results in the next section.
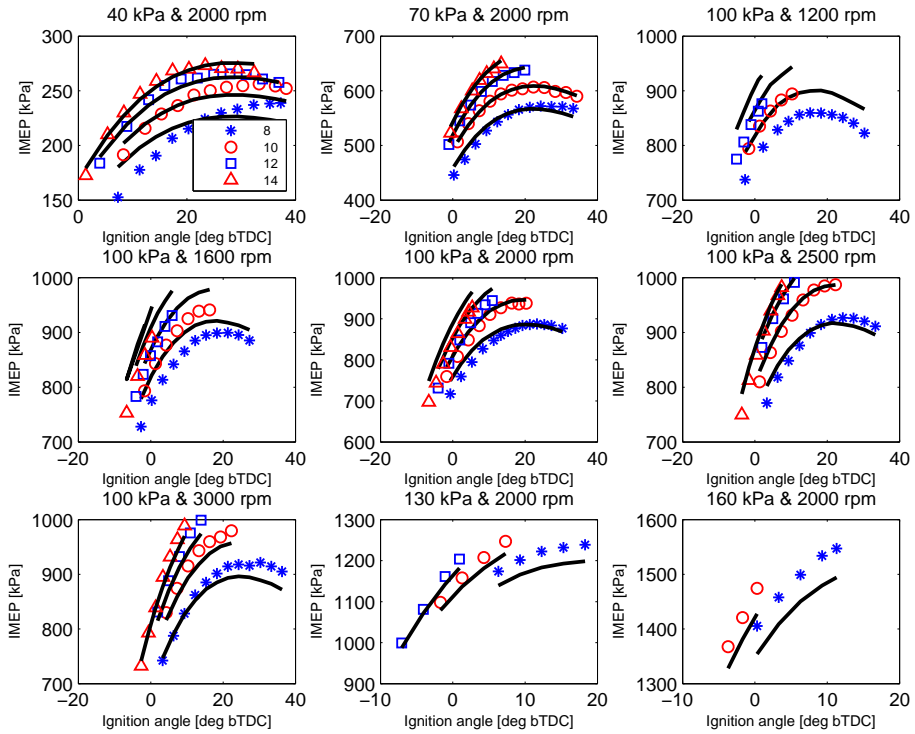
Figure 5.10: Validation of the torque model, in all investigated speed and load points. The different dot-shapes (for different compression ratios) represent the measured net indicated mean effective pressures, and the solid lines the modelled. Only samples with knock intensity lower than I_{limit} are shown. (Data set: OR95)

5.3.1 Optimal compression ratio and ignition angle

Of great importance is how well suited the model is for finding an optimal combination of compression ratio and ignition angle, and this is therefore examined here. Figure 5.11 shows modelled and measured IMEP contours. It is seen that the modelled and measured contours have approximately the same appearance within each individual load point. Also shown in the contour plots are the choices of optimal compression ratio and ignition angle, that is $\{\widehat{r_c}, \widehat{\theta_{\text{ign}}}\}$, derived from the model and measurements respectively. The distance between the actual optimal combination and the one given by the model, is not of major interest. Instead, the performance should be judged based on the difference in efficiency between these two points.

The performance of the $\{\widehat{r_c}, \widehat{\theta_{\text{ign}}}\}$ determination is shown in Table 5.4. The relative loss in IMEP due to non optimal choice is 1.1% or less. However, it
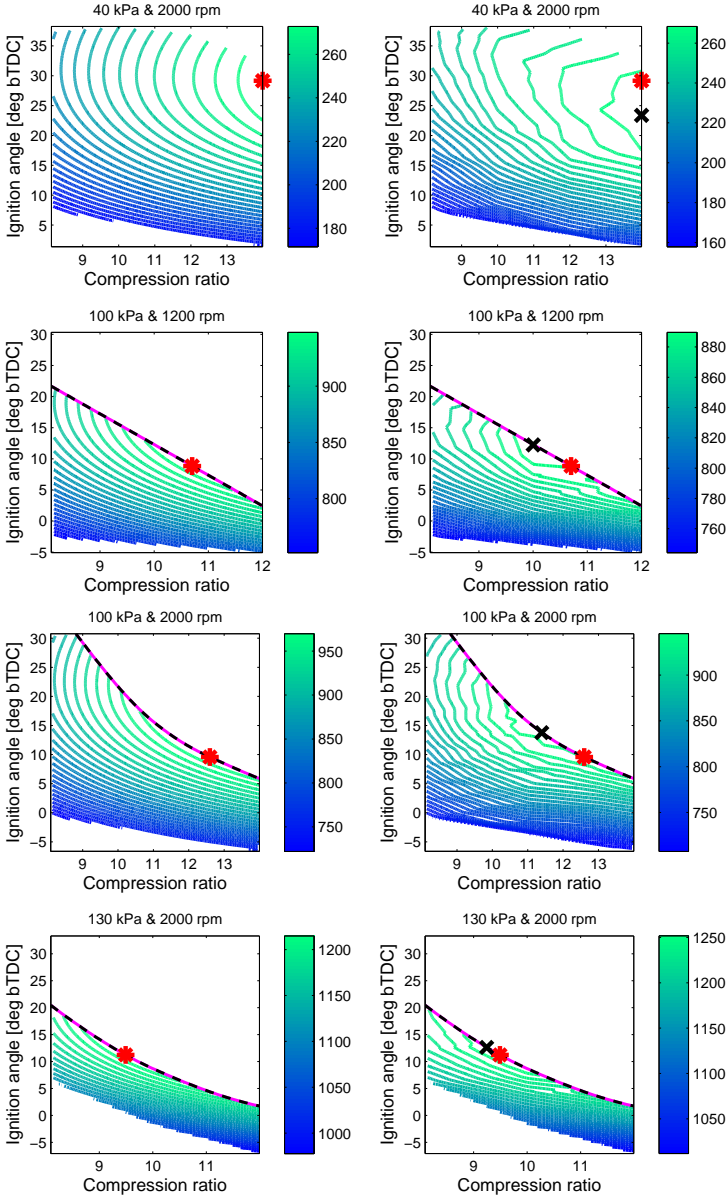
Figure 5.11: IMEP [kPa] contours. The contour plots to the left are based on the model and the ones to the right on measurements. Also shown in the plots is the optimal combination of compression ratio and ignition angle $\{\widehat{r_c}, \widehat{\theta_{ign}}\}$ according to the model, which is marked with a star. The optimal combination according to the measurements is marked with **x**. (Data set: OR95)

Table 5.2: Performance of the model when selecting the optimal $\{\widehat{r}_c, \widehat{\theta}_{ign}\}$. $\widehat{IMEP}$ represents IMEP at the optimum given by the measurements. $\widehat{IMEP}^*$ is the measured IMEP at $\{\widehat{r}_c, \widehat{\theta}_{ign}\}$ given by the model. Finally, $\Delta\widehat{IMEP}$ is the difference $\widehat{IMEP}^* - \widehat{IMEP}$. (Data set: OR95)

$\{p_{im}, N\}$	$\widehat{IMEP}$	$\widehat{IMEP}^*$	$\frac{\Delta\widehat{IMEP}}{\widehat{IMEP}}$
{ [kPa],[rpm]}	[bar]	[bar]	[%]
$\{40, 2000\}$	2.73	2.70	1.1
$\{70, 2000\}$	6.52	6.51	0.1
$\{100, 1200\}$	8.96	8.91	0.6
$\{100, 1600\}$	9.45	9.42	0.3
$\{100, 2000\}$	9.55	9.46	0.9
$\{100, 2500\}$	10.1	10.1	0.0
$\{100, 3000\}$	10.0	9.92	0.9
$\{130, 2000\}$	12.6	12.6	0.5
$\{160, 2000\}$	15.5	15.4	0.6

should be noted that the measured IMEP contains some noise, which has a slight effect on the performance measure. Finally, Table 5.3 shows the resulting effect on the efficiency. Since the net indicated efficiency is about 30–35%, the achieved efficiency is in the range 0–0.4 percentage units lower than its maximum.

5.4   Friction losses

Engine friction depends a lot on engine design and what additional parts are mounted on the engine. In particular, the model suggested below includes the compressor, and may therefore be of limited use for engines with other configurations. It is nevertheless important to have a friction model, in order to get a complete torque model.

The friction losses of the SVC engine as function of engine speed and load, are shown in Figure 5.12. The *measured* friction is calculated from measured data using

$$W_{\text{fric}} = \oint p\, dV - 2\pi n_r M_{\text{brake}} \tag{5.16}$$

which means that W_{fric} includes all engine losses that can not be seen in the cylinder pressure. The SVC engine is equipped with a mechanically driven compressor, and the power consumption of the compressor is therefore included in W_{fric}. The operating range is divided into 3 regions; one where the compressor is turned off, and two where it is turned on. If the requested inlet manifold pressure is above 1 atm, the compressor is turned on to boost the pressure. It can also be turned on as a strategy to improve the driving comfort, even though

Table 5.3: Net indicated efficiency, and loss in efficiency due to the deviation between the combination $\{\widehat{r_c}, \widehat{\theta_{\mathrm{ign}}}\}$ given by the model and given by the measurements. (Data set: OR95)

$\{p_{im}, N\}$	η_{in} [%]	$\Delta\eta_{\mathrm{in}}$ [perc. unit]
$\{40, 2000\}$	31	0.3
$\{70, 2000\}$	36	0.0
$\{100, 1200\}$	33	0.2
$\{100, 1600\}$	34	0.1
$\{100, 2000\}$	35	0.3
$\{100, 2500\}$	36	0.0
$\{100, 3000\}$	36	0.3
$\{130, 2000\}$	35	0.0
$\{160, 2000\}$	34	0.2

the inlet manifold pressure is low. This is done at engine speeds that exceed 2450 rpm. It is clearly visible in the figure that the friction losses increase when the compressor is switched on.

A widely used model for the friction work consists of a 2:nd order polynomial of engine speed (Heywood, 1988):

$$\mathrm{TFMEP} = C_1 + C_2 N + C_3 N^2 \tag{5.17}$$

The model describes the total friction where pumping losses are included

$$\mathrm{TFMEP} = \mathrm{FMEP} + \mathrm{PMEP}$$

In Heywood (1988) the following parameter values are recommended to be used at wide open throttle

$$
\begin{aligned}
C_1 &= 0.97 \\
C_2 &= 0.15/1000 \\
C_3 &= 0.05/(1000)^2
\end{aligned}
$$

where TFMEP is in [bar] and engine speed in [rpm].

The model correlated well with the friction losses of the SVC engine at 85 kPa, but does not capture the influence of load changes. Some other investigations (Inhelder, 1996; Stöckli, 1989; Patton et al., 1989) also show that the friction is slightly influenced by the engine load, e.g. due to that a higher cylinder pressure pushes the piston rings harder against the cylinder wall.

In this limited engine operating range, the change in friction due to increasing engine speed is almost linear. Thus, the following model is suggested that both take load changes and the compressor losses into account:

$$
W_{\mathrm{fric}} =
\begin{cases}
f_{\mathrm{n}1}\, N + f_{\mathrm{p}1}\, p_{\mathrm{im}} + f_{01} & \text{compressor off} \\
f_{\mathrm{n}2}\, N + f_{\mathrm{p}2}\, p_{\mathrm{im}} + f_{02} & \text{compressor on, } p_{\mathrm{im}} \gtrsim 1 \text{ atm} \\
f_{\mathrm{n}2}\, N + f_{03} & \text{compressor on, } p_{\mathrm{im}} < 1 \text{ atm}
\end{cases}
\tag{5.18}
$$
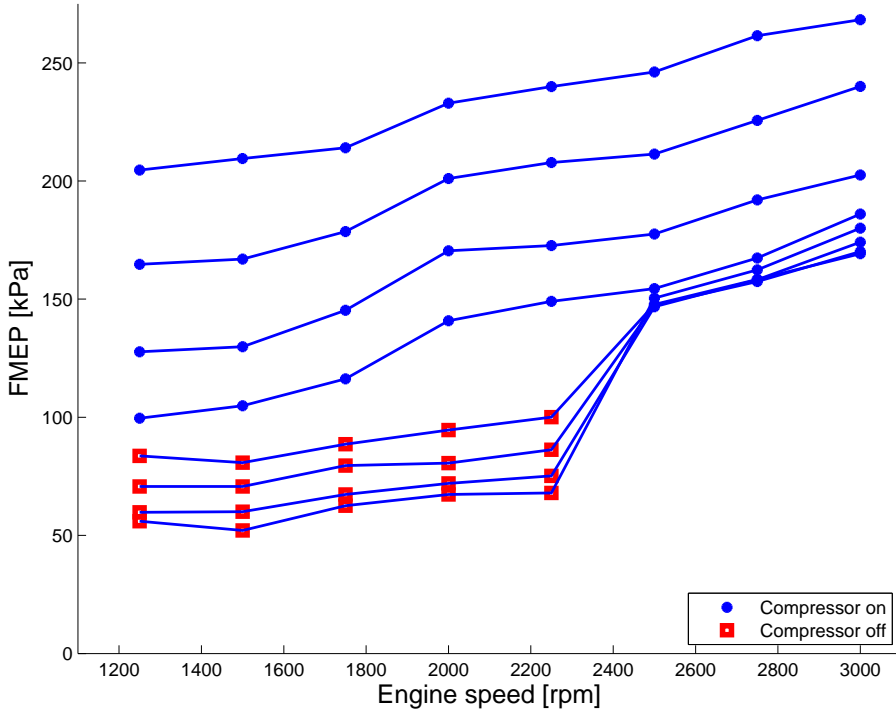
Figure 5.12: Engine friction as function of engine speed, based on the 8x8 data set in Figure 5.1. The different curves represent individual inlet manifold pressures {40,55,70,85,100,120,140,160} kPa, starting at 40 kPa at the bottom curve. Note that FMEP here also includes the compressor work.

The parameters for this specific engine are identified to

$$
\begin{aligned}
f_{N1} &= 1.6 \quad [\text{Nm} \cdot \text{s}] \\
f_{p1} &= -1.0 \cdot 10^{-3} \quad [\text{Nm/Pa}] \\
f_{01} &= 140 \quad [\text{Nm}] \\
f_{N2} &= 4.3 \quad [\text{Nm} \cdot \text{s}] \\
f_{p2} &= 2.6 \cdot 10^{-3} \quad [\text{Nm/Pa}] \\
f_{02} &= -190 \quad [\text{Nm}] \\
f_{03} &= 61 \quad [\text{Nm}]
\end{aligned}
$$

and a comparison between the model and the measured engine friction is shown in Figure 5.13.
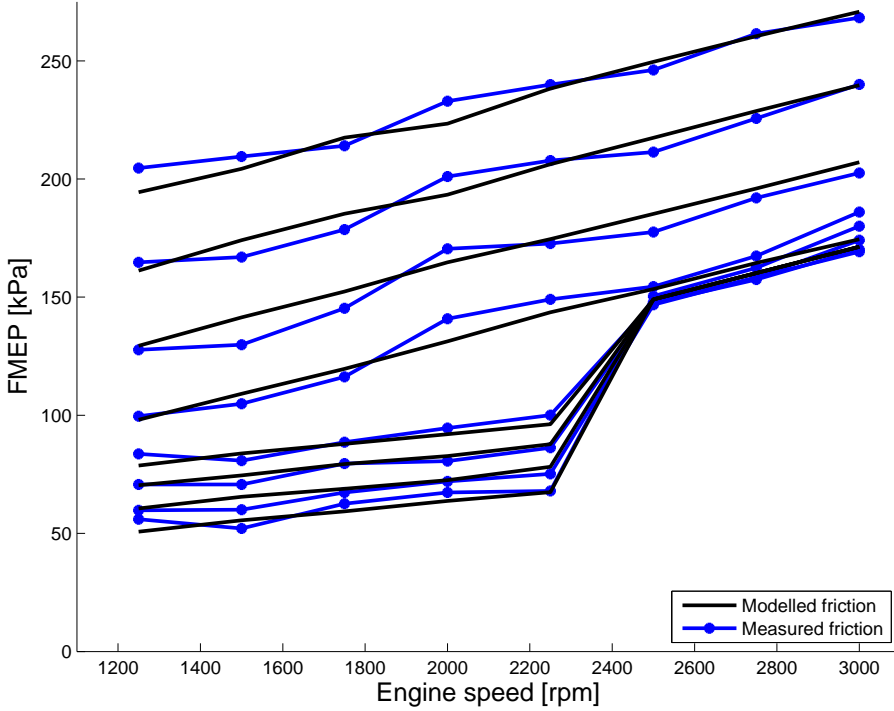
Figure 5.13: Modelled and measured friction for the 8x8 point data set.

5.5   Validation of the torque model

An additional validation is performed on the OR95 data set. The object is to investigate the validity of the resulting torque model and the assumption that the optimal choice of compression ratio and ignition angle can be found using the IMEP part of the torque model solely.

Modelled and measured BMEP are shown in Figure 5.14. The modelled BMEP curves coincide well with the measurements. The difference between measured and estimated BMEP is called ΔBMEP, that is

$$\Delta\mathrm{BMEP}(r_\mathrm{c}, \theta_\mathrm{ign}) = \mathrm{BMEP}_\mathrm{mod}(r_\mathrm{c}, \theta_\mathrm{ign}) - \mathrm{BMEP}_\mathrm{meas}(r_\mathrm{c}, \theta_\mathrm{ign}) \qquad (5.19)$$

The correlations between ΔBMEP, and p_im, N, r_c, and θ_ign are

$$
\begin{aligned}
\rho(p_\mathrm{im}, \Delta\mathrm{BMEP}) &= -0.04 \\
\rho(N, \Delta\mathrm{BMEP}) &= -0.56 \\
\rho(r_\mathrm{c}, \Delta\mathrm{BMEP}) &= -0.07 \\
\rho(\theta_\mathrm{ign}, \Delta\mathrm{BMEP}) &= 0.01
\end{aligned}
$$
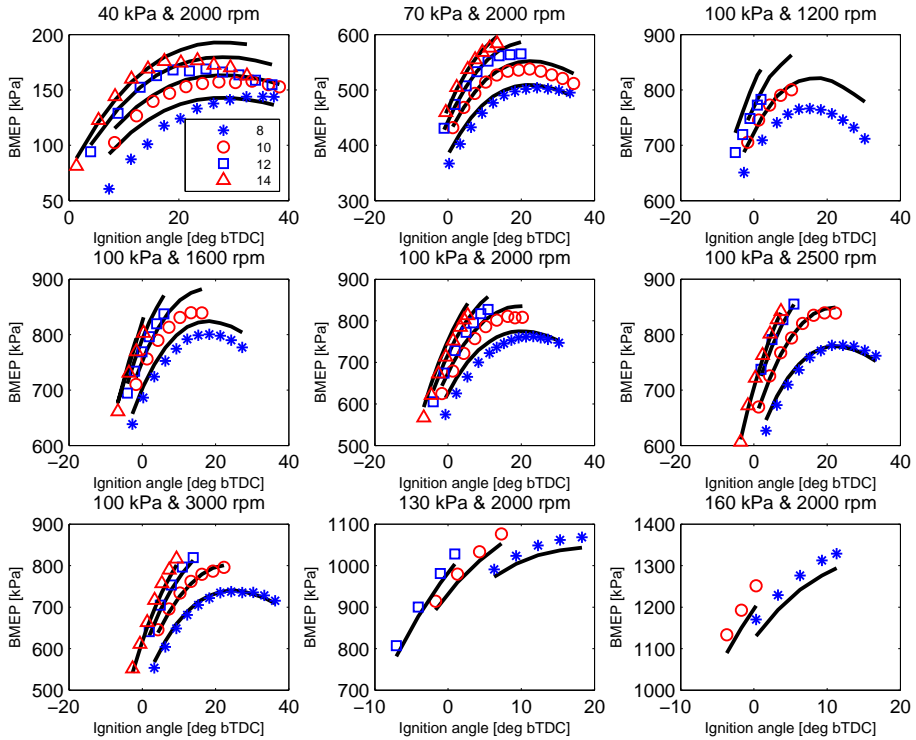
Figure 5.14: Validation of the torque model, in all investigated speed and load points. The measured BMEP is represented by different dot-shapes, depending on compression ratio, and the solid lines the modelled. Only samples in the feasible region are shown, in other words those with no or sufficiently low knock intensities. (Data set: OR95)

The correlations are small except for the engine speed. As the engine speed is constant throughout the optimisation, this correlation is not disquieting. The conclusion is that the model is a good description of the engine torque.

5.5.1   Optimal compression ratio and ignition angle

The friction model takes load and engine speed into account, while possible dependencies on compression ratio and ignition angle are ignored. To validate that this modelling assumption is appropriate, the same comparison on estimation of optimal compression ratio and ignition angle as in Section 5.3 is repeated. The modelled optimal combination of the control parameters is once again based on only the IMEP part of the torque model, but this time the measurement based estimation is from BMEP. Figure 5.15 shows modelled and measured BMEP

Table 5.4: Performance of the model when selecting the fuel optimal combination of compression ratio and ignition angle. $\Delta\widehat{BMEP}$ is defined as $\widehat{BMEP}^* - \widehat{BMEP}$, where $\widehat{BMEP}$ represents BMEP at the optimum given by the measurements, and $\widehat{BMEP}^*$ is the measured BMEP at $\{\widehat{r_c}, \widehat{\theta_{\mathrm{ign}}}\}$ given by the model. η is the engine efficiency. $\Delta\eta$ is the loss in efficiency (percentage unit) due to the deviation between the combination $\{\widehat{r_c}, \widehat{\theta_{\mathrm{ign}}}\}$ given by the model and given by the measurements. (Data set: OR95)

$\{p_{im},\ N\ \}$	$\Delta\widehat{\mathrm{BMEP}}$	η	$\Delta\eta$
{ [kPa],[rpm]}	[kPa]	[%]	[perc. unit]
$\{40,\ 2000\}$	5.6	20	0.65
$\{70,\ 2000\}$	9.2	32	0.50
$\{100,\ 1200\}$	1.1	29	0.04
$\{100,\ 1600\}$	5.9	30	0.21
$\{100,\ 2000\}$	1.0	31	0.04
$\{100,\ 2500\}$	9.4	31	0.33
$\{100,\ 3000\}$	15	29	0.53
$\{130,\ 2000\}$	1.3	31	0.04
$\{160,\ 2000\}$	1.0	30	0.02

contours. It is seen that the modelled and measured contours have about the same appearance within each individual load point. Also shown in the contour plots are the choices of optimal compression ratio and ignition angle, that is $\{\widehat{r_c}, \widehat{\theta_{\mathrm{ign}}}\}$, derived from the model and measurements respectively.

The performance of the $\{\widehat{r_c}, \widehat{\theta_{\mathrm{ign}}}\}$ estimation is shown in Table 5.4. It should be noted that the measured BMEP contains noise, which effects the performance measure slightly. The loss in engine efficiency due to non-optimal choice of compression ratio and ignition angle is between 0 and 0.7 percentage unit in all the investigated speed and load points. The greatest problem occurs at the $\{40\ \mathrm{kPa}, 2000\ \mathrm{rpm}\}$. An explanation to this can be read from Figure 5.7. It is assumed that θ_{opt} in (5.13) is independent of compression ratio, but at low inlet manifold pressures there is a dependence.

5.6   Conclusions

By a well designed controller it is possible to increase the engine efficiency. Motivated by that the greatest fuel saving is achieved by choosing the compression ratio and ignition angle that maximises the engine torque, a model for fuel optimal control of a spark-ignited variable compression engine has been derived. The main task of the model is to be suitable for determining the optimal combination of compression ratio and ignition angle. The model is valid during stoichiometric and no or low knock conditions.
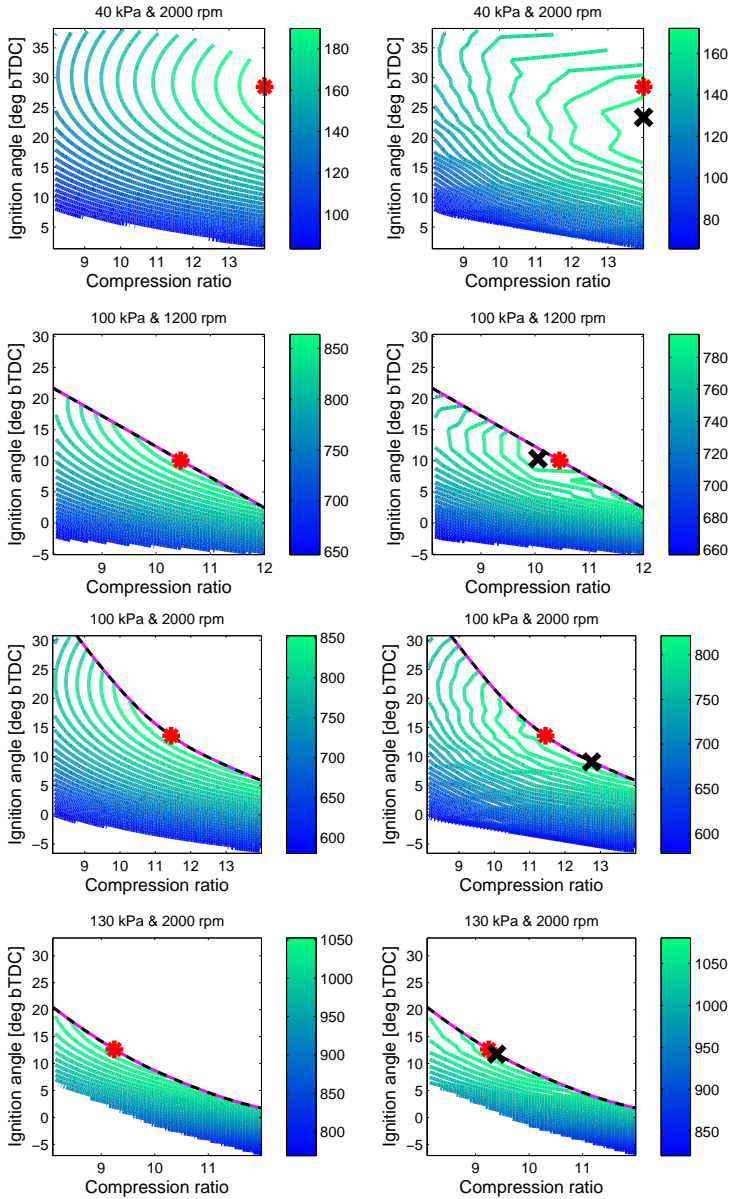
Figure 5.15: BMEP contours. The contour plots to the left are based on the model and the ones to the right on measurements. Also shown in the plots is the optimal combination of compression ratio and ignition angle $\{\widehat{r_{\mathrm{c}}}, \widehat{\theta_{\mathrm{ign}}}\}$ according to the model, which is marked with a star. The optimal combination according to the measurements is marked with **x**. (Data set: OR95)

The torque model consists of the following sub-models: Gross indicated work, pumping losses and friction work. The optimal combination of compression ratio and ignition angle is given solely by the model for gross indicated work, while all three sub-models are necessary for determining the corresponding air mass flow.

The conclusion is that the model, despite its simplicity, describes both the indicated and brake work with good accuracy. The only systematic deviation between modelled and measured IMEP and BMEP is from the engine speed, but this does not effect the performance of the task of choosing an optimal combination of compression ratio and ignition angle. It is shown that when the model is used for selecting the best choice of $\{\widehat{r_c}, \widehat{\theta_{\mathrm{ign}}}\}$ it results in an IMEP that is 0–1.2% from its maximum value for the investigated speed and load points. This corresponds to a maximum loss of 0–0.7 percentage units in total engine efficiency.

6

CONCLUSIONS

The central question in this thesis was to find the fuel optimal combination of compression ratio, ignition angle, and air mass flow for a given torque and engine speed, under the conditions that the knock intensity is sufficiently low and that the air and fuel mixture is stoichiometric. This was stated in the first chapter of the thesis, and the optimisation problem was reformulated to a problem that is easier to solve but has the same solution. The following chapters have been dedicated to the components in the optimisation problem, in particular to give tools that can be used in a fuel optimal controller and to gain knowledge about the underlying mechanisms.

Four different methods for knock detection were proposed and evaluated in Chapter 2. Three of the methods were categorised as on-line methods, and these can be used by a knock controller to get feedback on knock occurrence. One of the methods was then used in the study of relations between knock signal properties and knock occurrence in Chapter 3. This investigation gave knowledge about what physical properties a knock model, intended for control or in the design phase of a knock controller, should describe.

A new formulation of multi-zone combustion engine models was proposed in Chapter 4. One of many possible applications for a model based on this formulation is to describe the engine efficiency. Chapter 5 contributed by giving knowledge about how engine efficiency depends on compression ratio and ignition angle. A torque model was developed and validated on experimental data. This model can be used in an optimisation algorithm for finding the fuel optimal choice of compression ratio and ignition angle.

The overall conclusions of this thesis are:

- The relation between the logarithm of the normalised knock energy and the rate of knock occurrence is almost linear. This result is valid for all the investigated speed and load points, all compression ratios, and for the two investigated fuels (petrol with octane rating 95 and 99).

- The words *angle(/time) at knock-onset* should be used with great care. In the knock intensity region that is of interest for a knock controller, the high pass filtered cylinder pressure traces show signs of multiple knock-onsets and/or a gradual increase in amplitude over several oscillation periods.

- The three proposed knock detectors are robust to disturbances, and estimates the angle at knock-onset with good accuracy. From the previous conclusion it can be understood that it is a question of definition how close to the true angle at knock-onset the estimation is.

- The new formulation of multi-zone combustion engine models can be successfully used in various applications.

- The maximum efficiency is in many cases found for compression ratios lower than 14, which is the maximum compression ratio of the SVC engine, even if knock is not considered in the optimisation. This is because occurrence of engine knock decreases the engine efficiency, since the pressure oscillation increases the heat transfer.

- The torque model can be used to determine the fuel optimal choice of compression ratio and ignition angle with high accuracy. The choice made with this model resulted in an IMEP that is 0–1.2% from its maximum value in the investigated speed and load points, which corresponds to a loss in engine efficiency compared to the true optimum of at most 0.7%.

A

THE GEOMETRY OF THE SVC ENGINE

A first sketch of the SVC engine, drawn by its inventor Per Gillbrant.

This chapter is based on Nilsson (2001)

The goal of this chapter is to find an expression for the cylinder volume as function of crank angle and compression ratio for the SVC engine. The derived model is compared with a commonly used expression for the cylinder volume. It is shown that the asymmetry in the cylinder volume to crank angle curve, caused by the tilting of the engine, is hardly noticeable. However, what has to be considered is the shift in top dead centre (TDC) angle.

A.1   Engine geometry

On an SVC engine, the compression ratio can be varied between 8 and 14. The compression ratio is changed by tilting the mono head, which consists of the cylinders and cylinder head. The mono head is tilted relative to the crank case and the cylinder head is thereby moved away from the crankshaft, as can be seen in Figure A.1. The consequence is that the piston does not reach as close to the cylinder head at TDC as it had done in upright position, which leaves a greater clearance volume.

SAAB Variable Compression Engine

14:1   8:1
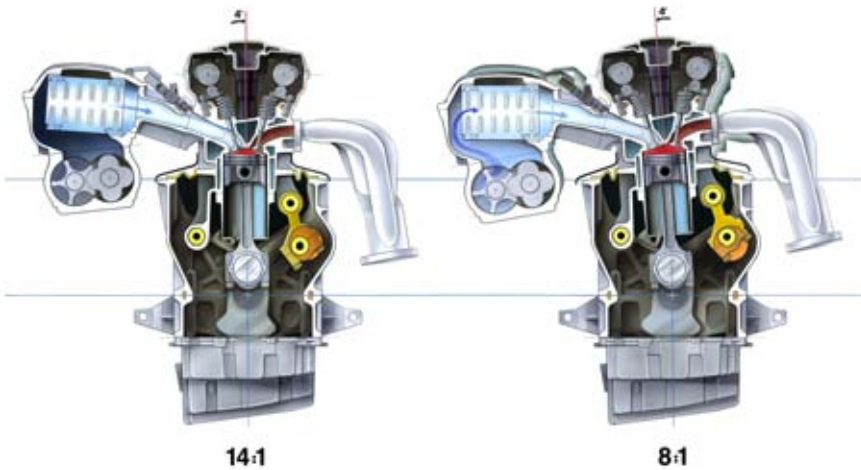
Figure A.1: The SAAB Variable Compression (SVC) engine. The compression can be changed between 8 and 14. At $r_c = 14$ the engine is in upright position, and at $r_c = 8$ the mono head is tilted.

Sketches of the SVC engine and its geometry are shown in Figure A.2, and the names of the lengths and variables are shown in Table A.1. The rotational centre O of the mono head is at a distance r from the cylinder centre. The distance x is $r + 2.2$ mm which means that there is a piston pin offset of 2.2 mm. At upright position, that is for a tilt angle of $v = 0$, the compression ratio is 14.

Note that the crank angle θ is defined as the angular distance from the vertical axis.

Table A.1: The geometry of the SVC engine

B	Cylinder bore
l	Connecting rod length
a	Crank shaft radius
O	Rotational centre of mono head
r	Distance between rotational centre and centre of cylinder
x	Horizontal distance between rotational centre and crank shaft
y	Vertical distance between rotational centre and crank shaft
θ	Crank angle
P	Distance to piston
v	Tilt angle, defined from horizontal plane
α	Angle between connecting rod and horizontal plane
x'	Intermediate variable, defined in Figure A.2

A.2 Cylinder volume

The cylinder volume is divided into two parts, the clearance volume V_c and the displacement volume. The volume as function of crank angle θ and tilt angle v is thus expressed as

$$V(\theta, v) = V_c(v) + \frac{\pi B^2}{4} \left(P(\theta_{\text{TDC}}(v), v) - P(\theta, v) \right) \quad \text{(A.1)}$$

where B is the cylinder bore, P is the distance to piston which is defined in Figure A.2, and θ_{TDC} is the crank angle at TDC. The clearance volume increases with the tilt

$$V_c(v) = V_c(0) + \frac{\pi B^2}{4} \left(P(\theta_{\text{TDC}}(0), 0) - P(\theta_{\text{TDC}}(v), v) \right) \quad \text{(A.2)}$$

The compression ratio at upright position is used as a reference for the calculation of the compression ratio at other tilt angles. From the definition of the compression ratio

$$r_c = \frac{V_{\max}}{V_{\min}}$$

the clearance volume at $v = 0$ can be determined

$$V_c(0) = \frac{\pi B^2}{4(r_c(0) - 1)} \left(P(\theta_{\text{TDC}}(0), 0) - P(\theta_{\text{BDC}}(0), 0) \right) \quad \text{(A.3)}$$
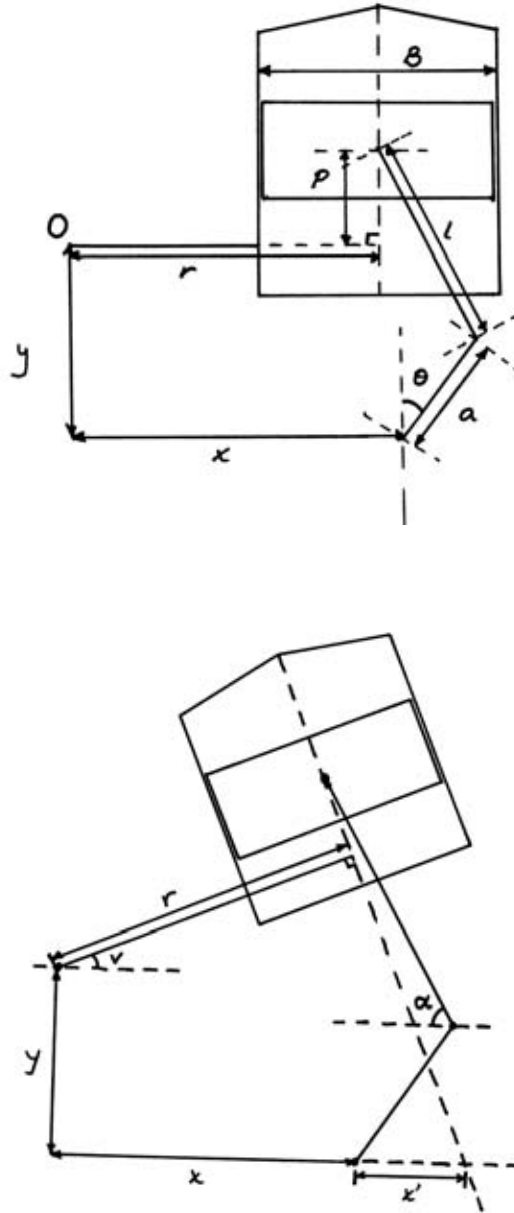
Figure A.2: Sketches of the SVC engine and its geometry. The names of the
the variables are shown in Table A.1. In the upper figure the mono head is
in its upright position ($v = 0$). Values of the dimensions was received from
GM Powertrain in Södertälje.

From Figure A.2 we get the relations (A.4) and (A.5). For intermediate steps in the derivation see Nilsson (2001).

$$P(\theta, v) = \frac{1}{\cos v} \left(a \cos \theta + l \sin \alpha(\theta, v) - y - r \sin v \right) \tag{A.4a}$$

$$\alpha(\theta, v) = \arccos \left(\frac{a}{l} \sin(v + \theta) - \frac{x'(v)}{l} \cos v \right) - v \tag{A.4b}$$

$$x'(v) = -x + r \cos v + \tan v \left(y + r \sin v \right) \tag{A.4c}$$

and also the angles for top and bottom dead centre

$$\theta_{\mathrm{TDC}}(v) = -v + \arcsin \left(\frac{x'(v)}{l + a} \cos v \right) \tag{A.5a}$$

$$\theta_{\mathrm{BDC}}(v) = \pi - v + \arcsin \left(\frac{x'(v)}{l - a} \cos v \right) \tag{A.5b}$$

The *SVC cylinder volume function* is received by collecting equations (A.1) to (A.5).

A.3 Volume function comparisons

The TDC angle changes with compression ratio, between $\theta \approx -0.5°$ at $r_c = 14$ and $\theta \approx -2.5°$ at $r_c = 8$, as shown in Figure A.3. The variation in BDC angle is much smaller, less than $0.6°$. An interesting observation is that the angle at TDC in upright position is $\neq 0$, since there is a piston pin-offset of 2.2 mm.

The most common way to model the cylinder volume is presented in Heywood (1988)

$$V(\theta, r_c) = V_c(r_c) + \frac{\pi B^2}{4} \left(l + a - s(\theta) \right) \tag{A.6}$$

where s is the distance between the crankshaft and the piston pin, that is

$$s(\theta) = a \cos \theta + \sqrt{l^2 - a^2 \sin^2 \theta} \tag{A.7}$$

The model is valid under the assumption that there is no piston pin-offset and that the engine is in upright position. This model will here be called the *standard (std) volume function*. It is interesting to see how well this simple well-known model describes the cylinder volume of the SVC engine. A comparison between the models is shown in Figure A.4. The comparison is done for the worst case scenario, that is when the compression ratio is 8.

The maximum relative difference between the models is 6%. The maximum occurs in the region close to TDC, where the cylinder volume is small, which may seem like an unfair measure of performance. Nevertheless, when modelling the region close to TDC a relative error of this magnitude may be severe, since the temperature and pressure are at their peaks and the chemical kinetics is fast.
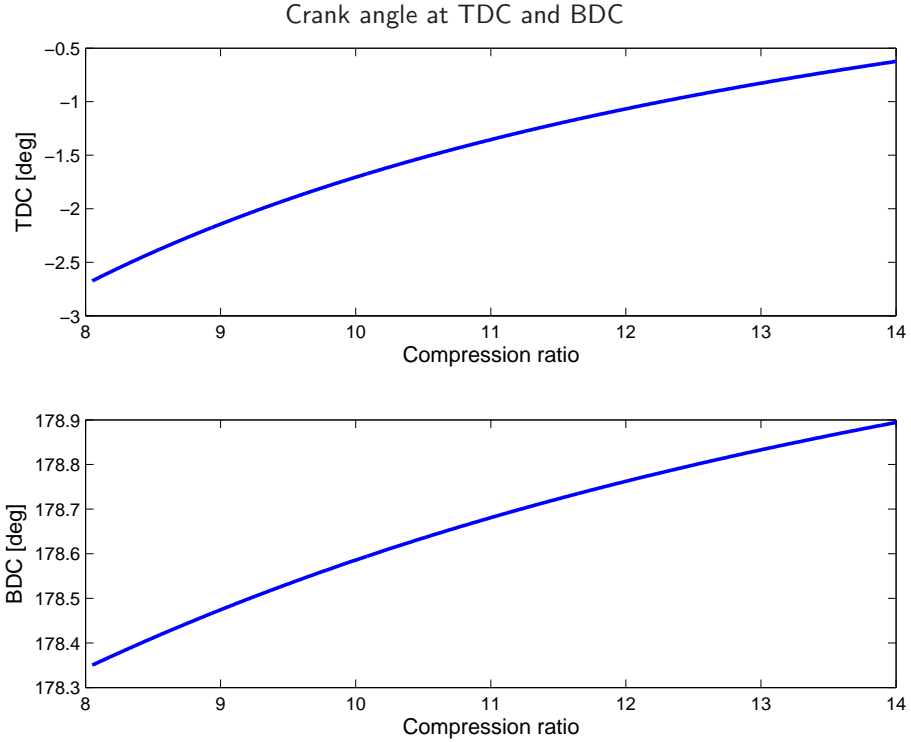
Figure A.3: The value of the crank angle at TDC and BDC changes with compression ratio, since the cylinder is slightly rotated. The figure shows the dependence of TDC and BDC on compression ratio. The crank angle is defined from a straight line parallel to the cylinder centre line, according to Figure A.2.

Visual inspection of the two curves in Figure A.4, gives that they are very similar in shapes, but phase shifted. With a simple adjustment of the crank angle, the relative deviation can be reduced about 10 times. The crank angle is adjusted so that TDC according to the standard volume function is at the actual TDC angle, that is

$$V_{\text{std}}(\theta - \theta_{\text{TDC}}) \approx V_{\text{SVC}}(\theta) \tag{A.8}$$

The result is shown in Figure A.5. Using this adjustment, the maximum relative error is 0.6% or less.

Another interesting characteristics is that at compression ratio 11.15 there exists a crank angle adjustment $\Delta\theta$ such that

$$V_{\text{std}}(\theta - \Delta\theta) \equiv V_{\text{SVC}}(\theta) \tag{A.9}$$

At this compression ratio, a line in the centre of the cylinder parallel to the cylinder walls points towards the rotational centre of the crank shaft. This is
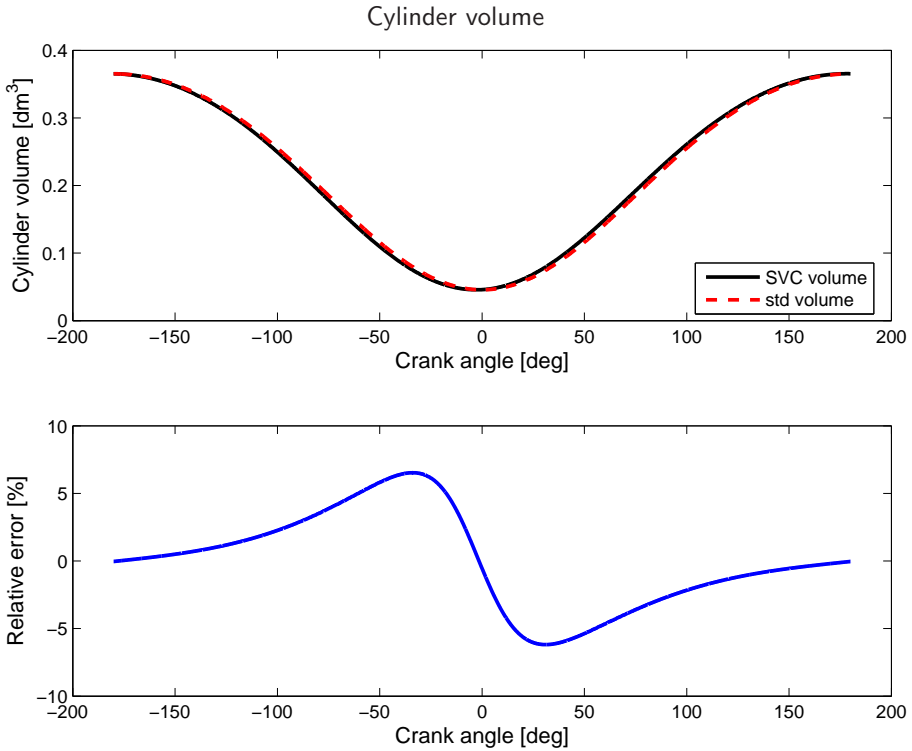
Figure A.4: Calculating the cylinder volume with the SVC volume function and the standard volume function, produces different results. The figure shows the result at $r_c = 8$. The maximum relative difference between the models are more than 6%.

possible since r in Figure A.2 is 2.2 mm shorter than x. At all other compression ratios the SVC volume function is asymmetric. Choosing the $\Delta\theta(r_c)$ that minimises the maximum relative error, the resulting maximum relative error is between 0 and 0.4%.

A.4 Conclusions

The cylinder volume as function of crank angle is close to symmetric. This makes it possible to calculate the volume with high accuracy using the standard volume function, provided that the crank angle is properly adjusted.

The most important observation is that the angle of TDC changes with compression ratio. One might suggest that the definition of the crank angle should follow the change in TDC, so that $\theta = 0$ is by definition at TDC. Since the volume to crank angle has almost exactly the same shape as the standard
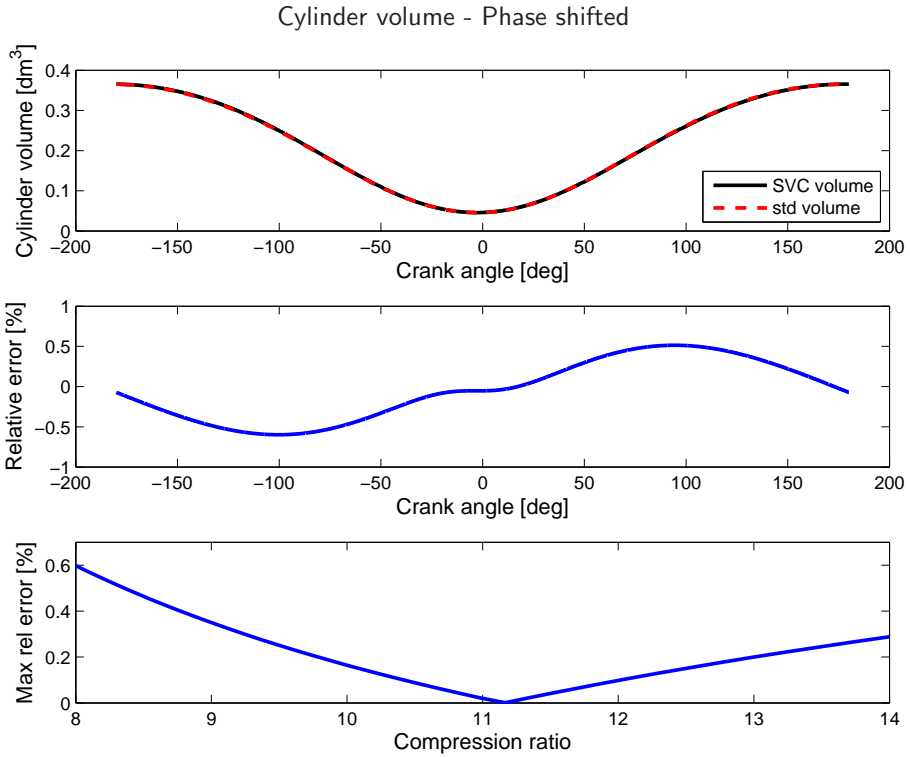
Figure A.5: By adjusting the crank angle phasing when using the standard volume function, so that the TDC angle according to the std volume function coincide with the actual TDC, the maximum error is reduced 10 times for $r_c = 8$. In the bottom plot, the maximum relative error is shown as function of compression ratio. The maximum relative error is 0.6% or less.

volume function, models derived for conventional engines will also hold for this engine, and no extra concern is needed for the shift in TDC angle. However, a 58X sensor or incremental encoder, which are mounted on the crankshaft, is unaffected by the tilt angle of the mono head. This means that TDC will move with respect to the 58X sensor and incremental encoder. Therefore, if measurement data are to be used, attention must be payed to the dependence between compression ratio and TDC angle.

B

ENGINE MEASUREMENTS
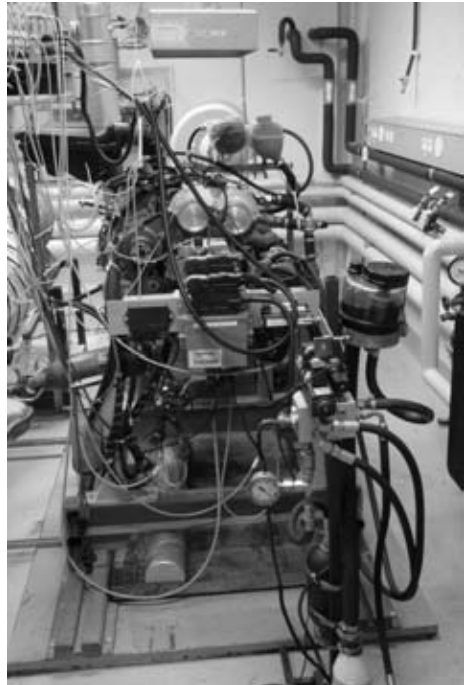
The SVC engine in Vehicular Systems engine research laboratory.

The data sets that are used in this thesis were measured in Vehicular Systems engine research laboratory. The research laboratory consists of an engine test cell and a control room. The engines in the test cell are connected to electrical dynamometers, making it possible to run the engines at specified constant load and engine speed with high accuracy. All the measurements are from the SVC engine with one exception; the cylinder pressure in Figure 4.1 was measured on a SAAB 2.3 litre naturally aspirated engine.

Two instruments are used to collect the sensor signals. These are HP E1415 and HP E1433 from Hewlett-Packard. HP E1433 is used for signals that require a very high sampling frequency of about 1 sample per crank angle degree or more. One such signal is the cylinder pressure. Engine speed, engine load, compression ratio, and air mass flow are examples of signals that do not require as high sampling frequency as the cylinder pressure. Sensors that measure these quantities are connected to the HP E1415 instrument.

B.1 Data sets

Four data sets from the SVC engine are used in the investigations:

- The knock detection data set

- The OR95 data set

- The OR99 data set

- The 8x8 data set

Here follows a description of the four data sets—the operating points included, the sensor signals, and how the measurements are performed.

In addition to these four data sets, data sets intended for calibration of the crank angle were also measured. An example of such a set is the one that is used in Figure B.3.

The knock detection data set   For evaluation of the knock detection methods in Chapter 2, cylinder pressure was measured with an asymmetrically placed flush-mounted sensor at a time-based sampling frequency of 82 kHz. The cylinder pressure sensor was a non-cooled 5 mm piezo-electric sensor from Kistler, type 6052.

Table B.1 shows the investigated engine operating points, and Table B.2 the sensor signals. The data was collected at stationary conditions. The data includes 99 consecutive cycles from each operating point.

OR95   For the validation of the torque model in Chapter 5 a data set was collected from the SVC engine running on petrol with octane rating 95. The data set is also used in the knock intensity study in Chapter 3.

Table B.1: Measured operating points (OP) in the knock detection data set, where p_{im} is inlet manifold pressure in kPa, N engine speed in rpm, r_c compression ratio, and θ_{ign} the ignition angle in degrees bTDC.

OP	p_{im}	N	r_c	θ_{ign}
1	70	1200	9	12°
2	70	1200	9	30°
3	70	1200	14	12°
4	70	1200	14	24°
5	70	2000	14	28°
6	70	3000	9	12°
7	70	3000	14	12°
8	100	1200	10	30°
9	100	1200	14	4°
10	100	2000	10	35°
11	100	2000	14	9°
12	100	3000	9	12°
13	100	3000	10	35°
14	100	3000	14	15°
15	130	2000	9	12°
16	130	2000	10	17°

Table B.2: Sensor signals in the knock detection data set. The ignition angle is read directly from the ECU, and is in other words not a true sensor signal.

Signal	Sampling frequency
Cylinder pressure	81920 Hz
Crank angle	81920 Hz
Inlet manifold pressure	10 Hz
Exhaust manifold pressure	10 Hz
Air fuel ratio	10 Hz
Compression ratio	10 Hz
Coolant temperature	10 Hz
Air mass flow	10 Hz
Engine speed	10 Hz
Ignition angle	1 sample/operating point
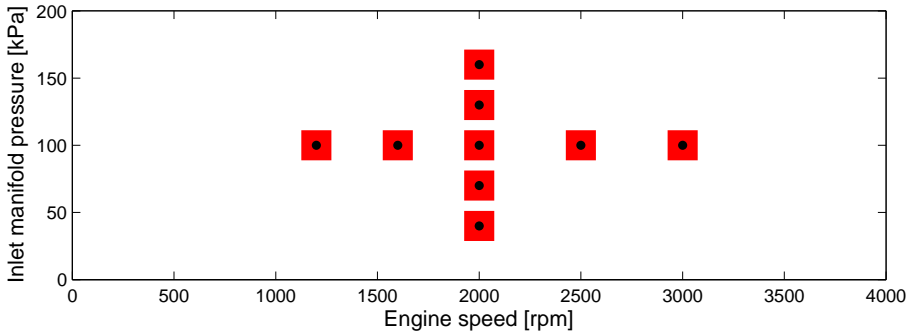
Figure B.1: The speed and load points in the OR95 and OR99 data sets. In each speed and load point several measurements were made for different combinations of compression ratio and ignition angle.

A total of 388 operating points were measured, divided into the 9 different speed and load points that are shown in Figure B.1. In each load point the compression ratio was increased as high as the the knock intensity allowed, from 8 to 14 in steps of 2. The exception was at $\{100 \text{ kPa}, 2000 \text{ rpm}\}$ where the compression ratio was increased in steps of 1. Ignition angles were chosen such that the relation between torque and ignition is captured in a neighbourhood of MBT. When the knock intensity was too high, the ignition was not advanced any further, even though MBT had not yet been reached.

In each operating point, 500 consecutive cycles were collected at stationary conditions. The sensor signals are shown in Table B.3. Cylinder pressure was measured time-based at a sampling frequency of 76800 Hz, with a flush-mounted piezoelectric pressure sensor of type Kistler 6052.

Throughout the measurements, the coolant fluid had a temperature between 85°C and 91°C, increasing almost linearly with the inlet manifold pressure p_{im}. However, in each individual load point the variation is 1°C or less.

OR99   The same measurement as for the OR95 data set was repeated, but this time with the SVC engine running on petrol with octane rating 99. This data set was used for parameter estimation in the torque model in Chapter 5 and in the knock intensity investigation in Chapter 3. The data set is also used in the illustrations of non-ideal knock traces in Figure 2.5–2.8.

The 8x8 data set   The OR95 and OR99 data sets offer a high resolution in compression ratio and ignition angle, but not in engine speed and load. To be able to describe the engine friction and the operation of the compressor, a data set containing the operating points shown in Figure B.2 was measured on the engine running on petrol with octane rating 99. A total of 64 speed and load points were measured at stationary conditions. Only one combination of

Table B.3: Sensor signals in the OR95, OR99 and 8x8 data sets. The ignition angle is read directly from the ECU.

Signal	Sampling frequency
Cylinder pressure	76800 Hz
Crank angle	76800 Hz
Inlet manifold pressure	10 Hz
Exhaust manifold pressure	10 Hz
Air fuel ratio	10 Hz
Compression ratio	10 Hz
Inlet manifold temperature	10 Hz
Exhaust manifold temperature	10 Hz
Coolant temperature	10 Hz
Air mass flow	10 Hz
Fuel injection time	10 Hz
Engine speed	10 Hz
Engine torque	10 Hz
Ignition angle	1 sample/operating point

Table B.4: The amount of air mass flow at which the compressor is turned on and off. The air mass flow is in [g/s].

Engine speed	on	off
1250	15	13
1500	18	16
1750	22	20
2000	25	22
2250	28	25
2500	–	–
2750	–	–
3000	–	–

compression ratio and ignition angle was used in each point. The compression ratio was set to 10, and the ignition angle was either set to the one chosen by the ECU, or retarded from that angle to a knock free zone. The same sensors as in the OR95 and OR99 data sets were used, see Table B.3.

To determine at what air mass flows the compressor is turned on and off, the engine was run at constant speed while the air mass flow was slowly increased or decreased. The result is shown in Table B.4. The compressor is always turned on for engine speeds of 2500 rpm or higher, irrespectively of the air mass flow.
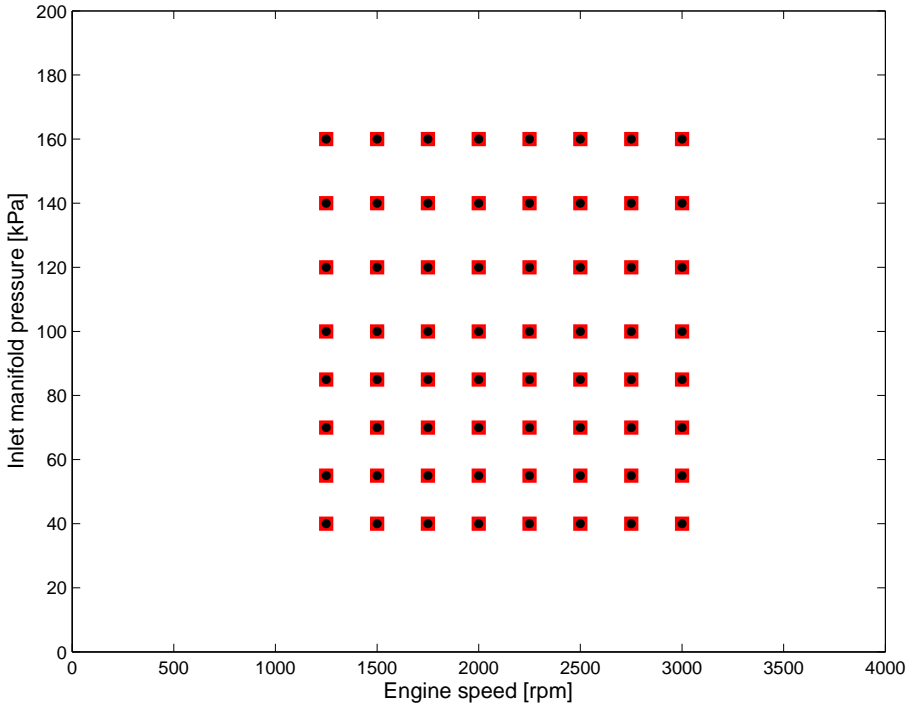
Figure B.2: The speed and load points in the 8x8 data set.

B.2   Crank angle and cylinder pressure

The output from the HP E1433 instrument is a data matrix, consisting of one column for the unconverted cylinder pressure and two columns for the signals from an incremental encoder (Leine&Linde RSI 505). The signals from the incremental encoder supplies information about the crank angle. Multiple consecutive cycles are measured in each operating point, and the data from all these cycles are collected in the same data matrix.

The incremental encoder signals are converted into crank angle, and the data is then cut into sequences of one engine cycle length, each sequence starting at the beginning of the intake stroke.

Crank angle conversion   The crank angle is determined from the signals of an incremental encoder that is mounted on the crank shaft. The encoder delivers two signals; one signal with one pulse per revolution, and one signal with multiple pulses per revolution. The multiple pulses are at equidistant angles—in these measurements with either 360 or 720 pulses per revolution.

The pulse signals are translated into crank angle in the following steps:

1. The two pulse signals are transformed into two vectors with indexes, where the indexes corresponds to the sample number where the pulses start.

2. A temporary crank angle vector is created. The length of the vector is the same as the length of the data matrix. The first element in the vector is set to 0, and at each start of a pulse in the multiple pulse signal the crank angle is increased by $\frac{1}{2}$ or 1 crank angle degree, depending on the number of pulser per revolution. Linear interpolation is used for estimating the crank angle in the region between two pulses.

3. The temporary crank angle vector is adjusted with a crank angle offset

$$\theta = \theta_{\text{temp}} + \Delta\theta \qquad (B.1)$$

The crank angle offset $\Delta\theta$ is estimated from motored cycles. The estimation is based upon Nilsson and Eriksson (2004), that compares five different methods for TDC estimation based on simulated pressure curves. Due to lack of equipment for determining the true TDC, the methods have not been validated on measured data. However, the simulation shows that the maximum cylinder pressure during a motored engine cycle occurs at approximately 0.8° before TDC, if the SVC engine is running at 1000 rpm and compression ratio 14. In Figure B.3 the crank angle at maximum cylinder pressure for different compression ratios and engine speeds are shown, along with the calculated TDC according to the SVC volume function derived in Appendix A. The crank angle offset $\Delta\theta$ is chosen such that the crank angle at maximum cylinder pressure at 1000 rpm and $r_{\text{c}} = 14$ is $\approx 0.8°$ before the calculated TDC.

Cylinder pressure offset When the membrane of the piezo-electric pressure transducer is affected by an outer force, a charge is produced inside the quartz crystal. The pressure transducer is connected to a charge amplifier, which converts the charge to a voltage. The charge amplifier has some leakage current, which causes the amplifier to drift over time. The voltage u is translated to cylinder pressure using the following expression:

$$p_{\text{cyl}}(\theta) = \underbrace{C_{\text{ch.amp.}} u(\theta)}_{p_{\text{meas}}(\theta)} + \Delta p \qquad (B.2)$$

where $C_{\text{ch.amp.}}$ is the translation factor of the charge amplifier. The value of the cylinder pressure offset Δp changes from cycle to cycle, and has therefore to be calibrated for each cycle individually.

If the cylinder gas is compressed adiabatically, the following is valid

$$p_{\text{cyl}}(\theta) = \underbrace{p_{\text{cyl}}(\theta_0) V^{\gamma}(\theta_0)}_{k} \frac{1}{V^{-\gamma}(\theta)} \qquad (B.3)$$

In the region after inlet valve and before the spark is delivered, the temperature and pressure are low compared to later in the cycle, and the heat and mass
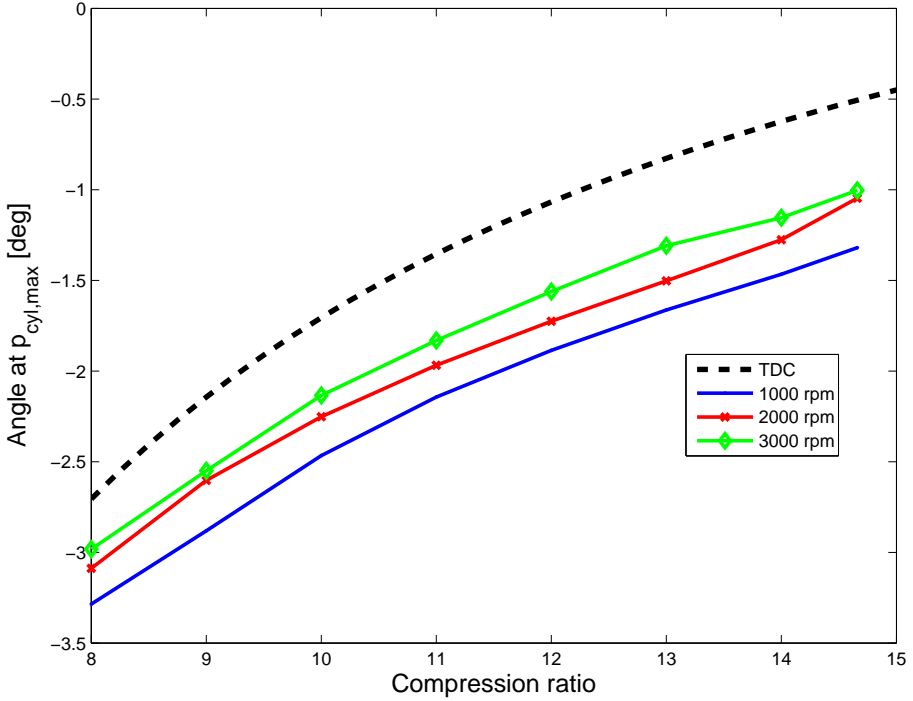
Figure B.3: Angle at cylinder pressure maximum for motored engine cycles.

losses are therefore also lower—the compression phase is close to adiabatic. This region therefore offers a good opportunity for calibration. Combining (B.2) and (B.3) gives:

$$p_{\mathrm{meas}}(\theta) = kV^{-\gamma}(\theta) - \Delta p \qquad (B.4)$$

The values of k and Δp are estimated by linear least squares. The cylinder pressure is then determined using (B.2).

The determinant of $\mathbb{A}_N$

Proposition C.1. *The determinant of $\mathbb{A}_N$ is*

$$\det \mathbb{A}_N = p^{N-1} \sum_{i=1}^{N} \left((c_i b_i - a_i d_i) \prod_{j \neq i}^{N} (d_j - b_j) \right) \tag{C.1}$$

Proof. A *minor* of order $N-1$ is defined to be the determinant of a submatrix of $\mathbb{A}_N$ obtained by striking out one row and one column from $\mathbb{A}_N$. The minor obtained by striking out the ith row and jth column is written M_{ij}. The determinant of $\mathbb{A}_N$ can then be written (Lancaster and Tismenetsky, 1984)

$$\mathcal{D}_N = \sum_{i=1}^{N} (-1)^{i+j} a_{ij} M_{ij} = \sum_{j=1}^{N} (-1)^{i+j} a_{ij} M_{ij} \tag{C.2}$$

Striking out the last column gives

$$
\mathcal{D}_N = \begin{vmatrix}
0 & 1 & 0 & 1 & 0 & \dots & 1 & 0 \\
a_1 & p & b_1 & 0 & 0 & \dots & 0 & 0 \\
c_1 & p & d_1 & 0 & 0 & & 0 & 0 \\
a_2 & 0 & 0 & p & b_2 & & 0 & 0 \\
c_2 & 0 & 0 & p & d_2 & & 0 & 0 \\
\vdots & \vdots & & & & \ddots & \vdots & \vdots \\
a_N & 0 & 0 & 0 & 0 & \dots & p & b_N \\
c_N & 0 & 0 & 0 & 0 & \dots & p & d_N
\end{vmatrix} =
$$

$$
= -b_N \begin{vmatrix}
0 & 1 & 0 & 1 & 0 & \dots & 0 & 1 \\
a_1 & p & b_1 & 0 & 0 & \dots & 0 & 0 \\
c_1 & p & d_1 & 0 & 0 & & 0 & 0 \\
a_2 & 0 & 0 & p & b_2 & & 0 & 0 \\
c_2 & 0 & 0 & p & d_2 & & 0 & 0 \\
\vdots & \vdots & & & & \ddots & \vdots & \vdots \\
c_{N-1} & 0 & 0 & p & d_2 & & d_{N-1} & 0 \\
c_N & 0 & 0 & 0 & 0 & \dots & 0 & p
\end{vmatrix} + d_N \begin{vmatrix}
0 & 1 & 0 & 1 & 0 & \dots & 0 & 1 \\
a_1 & p & b_1 & 0 & 0 & \dots & 0 & 0 \\
c_1 & p & d_1 & 0 & 0 & & 0 & 0 \\
a_2 & 0 & 0 & p & b_2 & & 0 & 0 \\
c_2 & 0 & 0 & p & d_2 & & 0 & 0 \\
\vdots & \vdots & & & & \ddots & \vdots & \vdots \\
c_{N-1} & 0 & 0 & p & d_2 & & d_{N-1} & 0 \\
a_N & 0 & 0 & 0 & 0 & \dots & 0 & p
\end{vmatrix}
$$

Seeing that the two matrices are equal to $\mathbb{A}_{N-1}$ except for the last row and column, the next step is to strike out the last column:

$$
\mathcal{D}_N = b_N \begin{vmatrix}
a_1 & p & b_1 & 0 & 0 & \dots & 0 & 0 \\
c_1 & p & d_1 & 0 & 0 & & 0 & 0 \\
a_2 & 0 & 0 & p & b_2 & & 0 & 0 \\
c_2 & 0 & 0 & p & d_2 & & 0 & 0 \\
\vdots & \vdots & & & & \ddots & \vdots & \vdots \\
c_{N-1} & 0 & 0 & 0 & 0 & \dots & p & d_{N-1} \\
c_N & 0 & 0 & 0 & 0 & \dots & 0 & 0
\end{vmatrix} - d_N \begin{vmatrix}
a_1 & p & b_1 & 0 & 0 & \dots & 0 \\
c_1 & p & d_1 & 0 & 0 & & 0 \\
a_2 & 0 & 0 & p & b_2 & & 0 \\
c_2 & 0 & 0 & p & d_2 & & 0 \\
\vdots & \vdots & & & & \ddots & \vdots \\
c_{N-1} & 0 & 0 & 0 & 0 & \dots & p & d_1 \\
a_N & 0 & 0 & 0 & 0 & \dots & 0
\end{vmatrix}
$$

$$
+ p\,(d_N - b_N)\,\mathcal{D}_{N-1} \quad \text{(C.3)}
$$

The two matrices of (C.3) are identical except for the elements in the first column of the last row, which are either c_N or a_N. Let the matrix $\mathbb{C}_N$ be the resulting matrix after striking out the last row and the first column, that is

$$
\mathbb{C}_N = \begin{pmatrix}
p & b_1 & 0 & 0 & \dots & 0 & 0 \\
p & d_1 & 0 & 0 & \dots & 0 & 0 \\
0 & 0 & p & b_2 & & 0 & 0 \\
0 & 0 & p & d_2 & & 0 & 0 \\
\vdots & \vdots & & & \ddots & \vdots & \vdots \\
0 & 0 & 0 & 0 & \dots & p & b_N \\
0 & 0 & 0 & 0 & \dots & p & d_N
\end{pmatrix} \quad \text{(C.4)}
$$

The determinant of $\mathbb{A}_N$ is then

$$\mathcal{D}_N = (b_N c_N - a_N d_N)\det\mathbb{C}_{N-1} + p\,(d_N - b_N)\,\mathcal{D}_{N-1} \tag{C.5}$$

The determinant of the matrix $\mathbb{C}$ is calculated in the same way as the determinant of $\mathbb{A}_N$:

$$\det\mathbb{C}_N = \begin{vmatrix} p & b_1 & 0 & 0 & \ldots & 0 & 0 \\ p & d_1 & 0 & 0 & \ldots & 0 & 0 \\ 0 & 0 & p & b_2 & & 0 & 0 \\ 0 & 0 & p & d_2 & & 0 & 0 \\ \vdots & \vdots & & & \ddots & \vdots & \vdots \\ 0 & 0 & 0 & 0 & \ldots & p & b_N \\ 0 & 0 & 0 & 0 & \ldots & p & d_N \end{vmatrix} =$$

$$= (d_N - b_N) \begin{vmatrix} p & b_1 & 0 & 0 & \ldots & 0 & 0 \\ p & d_1 & 0 & 0 & \ldots & 0 & 0 \\ 0 & 0 & p & b_2 & & 0 & 0 \\ 0 & 0 & p & d_2 & & 0 & 0 \\ \vdots & \vdots & & & \ddots & \vdots & \vdots \\ 0 & 0 & 0 & 0 & \ldots & d_{N-1} & 0 \\ 0 & 0 & 0 & 0 & \ldots & 0 & p \end{vmatrix} =$$

$$= p\,(d_N - b_N)\det\mathbb{C}_{N-1} = p^N \prod_{i=1}^{N}(d_i - b_i) \tag{C.6}$$

Equation (C.5) combined with (C.6) gives the following recursive expression for the determinant of $\mathbb{A}_N$:

$$\mathcal{D}_1 = b_1 c_1 - a_1 d_1 \tag{C.7}$$

$$\mathcal{D}_N = p\,(d_N - b_N)\,\mathcal{D}_{N-1} + (b_N c_N - a_N d_N)\,p^{N-1}\prod_{i=1}^{N-1}(d_i - b_i) \tag{C.8}$$

The final step in proving that $\mathcal{D}_N$ is equal to

$$\mathcal{D}_N = p^{N-1}\sum_{i=1}^{N}\left((c_i b_i - a_i d_i)\prod_{j\neq i}^{N}(d_j - b_j)\right)$$

is done by induction. It is easy to verify that (C.1) holds for $N = 1$:

$$\mathcal{D}_1 = p^0\,(c_1 b_1 - a_1 d_1)\cdot 1 = c_1 b_1 - a_1 d_1 \tag{C.9}$$

which is consistent with (C.8). Assume that (C.1) holds for $N = k - 1$, the determinant of $\mathbb{A}_N$ for $N = k$ is then:

$$\mathcal{D}_k = p\,(d_k - b_k)\mathcal{D}_{k-1} + (b_k c_k - a_k d_k)\,p^{k-1}\prod_{j=1}^{k-1}(d_j - b_j) =$$

$$= p(d_k - b_k)p^{k-2}\sum_{i=1}^{k-1}\left((c_i b_i - a_i d_i)\prod_{j\neq i}^{k-1}(d_j - b_j)\right) +$$

$$+ (b_k c_k - a_k d_k)\,p^{k-1}\prod_{j=1}^{k-1}(d_j - b_j) \quad \text{(C.10)}$$

Expanding this expression gives

$$\mathcal{D}_k = p^{k-1}\left[\sum_{i=1}^{k-1}\left((c_i b_i - a_i d_i)\prod_{j\neq i}^{k}(d_j - b_j)\right) + (b_k c_k - a_k d_k)\prod_{i=1}^{k-1}(d_i - b_i)\right] =$$

$$= p^{k-1}\left[\sum_{i=1}^{k}\left((c_i b_i - a_i d_i)\prod_{j\neq i}^{k}(d_j - b_j)\right)\right] \quad \text{(C.11)}$$

which is the same as (C.1). The theorem of induction together with (C.9) and (C.11) gives that (C.1) is valid for all N. ∎

Finally, the definitions of a_i, b_i, c_i and d_i from Section 4.1, that is

$$
\begin{aligned}
a_i &= V_i\left(1 - \tfrac{p}{R_i}\left(\tfrac{\partial R_i}{\partial p}\right)_{T_i}\right)\\
b_i &= -m_i\left(R_i + T_i\left(\tfrac{\partial R_i}{\partial T_i}\right)_p\right)\\
c_i &= -m_i T_i\left(\tfrac{T_i}{p}\left(\tfrac{\partial R_i}{\partial T_i}\right)_p + \left(\tfrac{\partial R_i}{\partial p}\right)_{T_i}\right)\\
d_i &= m_i\left(c_{p,i} - R_i - T_i\left(\tfrac{\partial R_i}{\partial T_i}\right)_p\right)
\end{aligned}
\quad \text{(C.12)}
$$

are inserted into (C.1). This results in the following expression for the determinant:

$$\det \mathbb{A}_N = -p^{N-1}\prod_{i=1}^{N}m_i \cdot \sum_{j=1}^{N}\left(V_j f_i \prod_{k\neq j}c_{p,k}\right)$$

$$\text{where} \quad f_j = 2T_j\left(\frac{\partial R_j}{\partial T_j}\right)_p + \frac{T_j^2}{R_j}\left(\frac{\partial R_j}{\partial T_j}\right)_p^2 - c_{v,j} + \frac{c_{p,j}\,p}{R_j}\left(\frac{\partial R_j}{\partial p}\right)_{T_j}$$

$$\text{(C.13)}$$

Bibliography

V. Arrigoni, G. Cornetti, B. Gaetani, and P. Ghezzi. Quantitative systems for measuring knock. *Proc Instn Mech Engrs*, 186:572–583, 1972.

P. W. Atkins. *The Elements of Physical Chemistry*. Oxford University Press, 2000. ISBN 0-19-879290-5.

J. Auzins, H. Johansson, and J. Nytomt. Ion-gap sense in missfire detection, knock and engine control. *SAE SP-1082*, (SAE Technical Paper Series No. 950004):21–28, 1995.

R. K. Barton, S. S. Lestz, and L. C. Duke. Knock intensity as a function of engine rate of pressure change. *SAE Technical Paper Series No. 700061*, 1970.

M. Basseville and I.V. Nikiforov. *Detection of Abrupt Changes*. PTR Prentice-Hall, Inc, 1993. ISBN 0-13-126780-9.

D. R. Blackmore and A. Thomas. *Fuel Economy of the Gasoline Engine*. Redwood Burn Limited, 1977.

C.A. Blunsdon and J.C. Dent. The simulation of autoignition and knock in a spark ignition engine with disk geometry. *SAE Technical Paper Series No. 940524*, 1994.

Christoph Bollig, Hans-Joerg Hermanns, Torsten Schelhase, and Frank Widmann. Combustion engine having a variable compression ratio. US Patent 5595146, January 21 1997.

D. Brand. *Control-Oriented Modeling of NO Emissions of SI Engines.* PhD thesis, ETH, Swiss Federal Institute of Technology, 2005.

G. Brecq, J. Bellettre, and M. Tazerout. A new indicator for knock detection in gas SI engines. *International Journal of Thermal Sciences*, 42:523–532, 2003.

Michael F. J. Brunt, Christopher R. Pond, and John Biundo. Gasoline engine knock analysis using cylinder pressure data. *SAE Technical Paper Series No. 980896*, 1998.

Klaas Burgdorf and Jerzy Chomiak. A new knock form - an experimental study. *SAE Technical Paper Series No. 982589*, 1998.

Klaas Burgdorf and Ingemar Denbratt. Comparison of cylinder pressure based knock detection methods. *SAE Technical Paper Series No. 972932*, 1997.

Klaas Burgdorf and Anders Karlström. Using multi-rate filter banks to detect internal combustion engine knock. *SAE Technical Paper Series No. 971670*, 1997.

D. F. Caris and E. E. Nelson. A new look at high compression engines. *SAE Technical Paper Series No. 590015*, 1959.

Lewis Carroll. *Alice's Adventures in Wonderland.* 1865.

S. Carstens-Behrens and J. F. Bohme. Fast knock detection using pattern signals. *IEEE International Conference on Acoustics, Speech, and Signal Processing*, 5:3145–3148, 2001.

S. Carstens-Behrens, M. Urlaub, J.F. Böhme, J. Förster, and F. Raichle. FEM approximation of internal combustion chambers for knock investigations. *SAE Technical Paper Series No. 2002-01-0237*, 2002.

George Casella and Roger Berger. *Statistical Inference.* Duxbury, 1990.

Gunnar Cedersund. System identification of nonlinear thermochemical systems with dynamical instabilities. Technical report, Department of Electrical Engineering, 2004. LiU-TEK-LIC-2004:36, Thesis No. 1107.

M. D. Checkel and J. D. Dale. Testing a third derivative knock indicator on a production engine. *SAE Technical Paper Series No. 860028*, 1986.

M. D. Checkel and J. D. Dale. Pressure trace knock measurement in a current s. i. production engine. *SAE Technical Paper Series No. 890243*, 1989.

Jerzy Chomiak and Jonas Sköld. Fuel effects on energy release and knock parameters in a si engine. *SAE Technical Paper Series No. 952404*, 1995.

Kwang Min Chun and John B. Heywood. Characterization of knock in a spark-ingition engine. *SAE Technical Paper Series No. 890156*, 1989.

Daniel Claesson. Improved experimental agreement of ionization and pressure peak location by adding a dynamical NO-model. Master's thesis, Linköpings Universitet, SE-581 83 Linköping, 2004.

James Ryland Clarke and Rodney John Tabaczynski. Internal combustion engine with adjustable compression ratio and knock control. US Patent 6135086, October 24 2000.

Enrico Corti and Davide Moro. Knock indexes thesholds setting methodology. *SAE Technical Paper Series No. 2007-01-1508*, 2007.

J. S. Cowart, J. C. Keck, J. B. Heywood, C. K. Westbrook, and W. J. Pitz. Engine knock predictions using a fully-detailed and a reduced chemical kinetic mechanism. *Twenty-Thirc Symposium (International) on Combustion*, 1990.

P. M. Dimpelfield and D. E. Foster. The prediction of auto ignition in spark-ignited engine. *SAE Technical Paper Series No. 841337*, 1984.

A. M. Douaud and P. Eyzat. Four-octane-number method for predicting the anti-knock behaviour of fuels and engines. *SAE Technical Paper Series No. 780080*, 1978.

H. Drangel and R. Reinmann. The variable compression (SVC) and the combustion control (SCC) - two ways to improve fuel economy and still comply with world-wide emission requirements. *SAE Technical Paper Series No. 2002-02-0996*, 2002.

Christel Elmqvist, Fredrik Lindström, Hans-Erik Ångström, Börje Grandin, and Gautam Kalghatgi. Optimizing engine concepts by using a simple model for knock prediction. *SAE Technical Paper Series No. 2003-01-3123*, 2005.

Lars Eriksson. *Spark Advance Modeling and Control*. PhD thesis, Linköping University, May 1999a.

Lars Eriksson. Spark advance for optimal efficiency. *SAE Technical Paper Series No. 99-01-0548*, 1999b.

Lars Eriksson. CHEPP - A chemical equilibrium program package for Matlab. *SAE Technical Paper Series No. 2004-04-0066*, 2004.

Lars Eriksson, Lars Nielsen, Jan Brugård, Johan Bergström, Fredrik Pettersson, and Per Andersson. Modeling and simulation of a turbo charged SI engine. *Annual Reviews in Control*, 26(1):129–137, 2002.

Olof Erlandsson, Gunnar Lundholm, Fredrik Söderberg, and Bengt Johansson. Demonstrating the performance and emission characteristics of a variable compression ratio, alvar-cycle engine. *SAE Technical Paper Series No. 982682*, 1998.

C.B.P. Finn. *Thermal Physics.* Stanley Thornes Ltd, second edition edition, 1998. ISBN 0-7487-4379-0.

John Fitton and Roy Nates. Knock erosion in spark-ignition engines. *SAE Technical Paper Series No. 962102*, 1996.

X. Gao, R. Stone, C. Hudson, and I. Bradbury. The detection and quantification of knock in spark ignition engines. *SAE Technical Paper Series No. 932759*, 1993.

J. A. Gatowski, E. N. Balles, K. M. Chun, F. E. Nelson, J. A. Ekchian, and J. B. Heywood. Heat release analysis of engine pressure data. *SAE Technical Paper Series No. 841359*, 1984.

Johan Gill. A java package for simulation of combustion engines. Master's thesis, Linköpings Universitet, SE-581 83 Linköping, 2003.

Irvin Glassman. *Combustion.* Academic Press, 1996. ISBN 0-12-285852-2.

Adina Elena Gogan. Application of improved modeling approaches for investigation of engine knock. Technical report, Department of Heat and Power Engineering, 2002.

Börje Grandin. *Knock in Gasoline Engines - The effects of mixture composition on knock onset and heat transfer.* PhD thesis, Chalmers University of Technology, 2001.

Fredrik Gustafsson. *Adaptive Filtering and Change Detection.* Wiley, 2000.

Fredrik Gustafsson, Lennart Ljung, and Mille Millnert. *Signalbehandling.* Number 91-44-01709-X. Studentlitteratur, second edition, 2001.

Shahrokh Hajireza, Bengt Sundén, and Fabian Mauss. Effect of inhomogeneities in the end gas temperature field on the autoignition in si engines. *SAE Technical Paper Series No. 2000-01-0954*, 2000.

Elbert Hendricks, Alain Chevalier, Michael Jensen, Spencer C. Sorenson, Dave Trumpy, and Joe Asik. Modeling of the intake manifold filling dynamics. *SAE Technical Paper Series No. 960037*, 1996.

J. B. Heywood. *Internal Combustion Engine Fundamentals.* McGraw-Hill series in mechanical engineering. McGraw-Hill, 1988. ISBN 0-07-100499-8.

C. Hudson, X. Gao, and R. Stone. Knock measurement for fuel evaluation in spark ignition engines. *The Science and Technology of Fuel and Energy*, 80: 395–407, 2001.

N. Härle and J.F. Böhme. Detection of knocking for spark ignition engines based on structural vibrations. *Acoustics, Speech and Processing, IEEE International Conference*, 12:1744–1747, 1987.

J. Inhelder. *Verbrauchs- und Schadstoffoptimiertes Ottomotor-Aufladekonzept.* PhD thesis, Swiss Federal Institute of Technology, Zürich, Diss. ETH No. 11948, 1996.

Eugene L. Keating. *Applied Combustion.* Number ISBN 0-8247-8127-9. Marcel Dekker, INC, 1993.

Uwe Kiencke and Lars Nielsen. *Automotive Control Systems For Engine, Driveline, and Vehicle.* Springer-Verlag, 2000.

Masao Kinoshita, Akinori Saito, Kazuhisa Mogi, and Kouichi Nakata. Study on ion current and pressure behaviour with knocking in engine cylinder. *JSAE Review*, 21:483–488, 2000.

Charles Kittel and Herbert Kroemer. *Thermal Physics.* W. H. Freeman and Company, second edition edition, 1980. ISBN 0-7167-1088-9.

Marcus Klein, Lars Eriksson, and Ylva Nilsson. Compression estimation from simulated and measured cylinder pressure. *SAE 2002 Transactions Journal of Engines, 2002-01-0843*, 111(3), September 2003.

Peter Kreuter, Peter Heuser, and Joachim Reinicke-Murmann. The meta VVH system – a continuously variable valve timing system. *SAE Technical Paper Series No. 980765*, 1998.

G. König and C. G. W. Sheppard. End gas autoignition and knock in a spark ignition engine. *SAE Technical Paper Series No. 902135*, 1990.

T. L. Lai. Sequential changepoint detection in quality control and dynamical systems. *Journal of the Royal Statistical Society. Series B (Methodological)*, 57(4):613–658, 1995.

Peter Lancaster and Miron Tismenetsky. *The Theory of Matrices.* Academic Press, second edition edition, 1984. ISBN 0-12-435560-9.

Dan Lazarescu, Vasilte Lazarescu, and Michaela Ungureanu. Knock detection based on power spectrum analysis. *IEEE International Symposium on Signals, Circuits and Systems*, 2:701–704, 2005.

W. R. Leppard. Individual-cylinder knock occurence and intensity in multi-cylinder engines. *SAE Technical Paper Series No. 820074*, 1982.

S. C. Li and F. A. Williams. NOx formation in two-stage methane-air flames. *Combustion and Flame*, 118(3):399–414, 1999.

S. C. Li, F. A. Williams, and K. Gebert. A reduced reaction mechanism for predicting knock in dual-fuel engines. *SAE Technical Paper Series No. 2000-01-0957*, 2000.

J. C. Livengood and P. C. Wu. Correlation of autoignition phenomena in internal combustion engines and rapid compression machines. *Fifth Symposium (International) on Combustion*, pages 347–356, 1955.

G. Lorden. Procedures for reacting to a change in distribution. *The Annals of Mathematical Statistics*, 1971.

Khaled Loubar, Jerome Bellettre, and Mohand Tazerout. Unsteady heat transfer enhancement around an engine cylinder in order to detect knock. *Journal of Heat Transfer*, 127:278–286, 2005.

D. Lyon. Knock and cyclic dispersion in a spark ignition engine. *I Mech E Conference Publications*, pages 105–115, 1986.

Thomas Tsoi-Hei Ma. Engine with variable compression ratio. US Patent 5791302, August 11 1998.

Rudolf R. Maly, Rupert Klein, Norbert Peters, and Gerhard König. Theoretical and experimental investigation of knock induced surface destruction. *SAE Technical Paper Series No. 902135*, 1990.

MCE-5. *DVD: Automobile 2008-2012 — The great challenges of the Variable Compression Ratio*. MCE-5 Development SA, `http://www.mce-5.com/`, 21 Avenue Georges Pompidou, F-69486 LYON Cedex 03, FRANCE, 2004.

Michael J. Moran and Howard N. Shapiro. *Fundamentals of engineering thermodynamics*. Johan Wiley & Sons, third edition edition, 1998. ISBN 0-471-97960-0.

Katsuya Moteki, Shunichi Aoyama, Kenshi Ushijima, Ryousuke Hiyoshi, Shinichi Takemura, Hiroya Fujimoto, and Takayuki Arai. A study of variable compression ratio system with a multi-link mechanism. *SAE Technical Paper Series No. 2003-01-0921*, 2003.

Jeffrey D. Naber, Jason R. Blough, Dave Frankowski, Monroe Goble, and John E. Szpytman. Analysis of combustion knock metrics in spark-ignition engines. *SAE Technical Paper Series No. 2006-01-0400*, 2006.

Ylva Nilsson. Cylinder volume function for SVC engines. Technical report, Department of Electrical Engineering, 2001. LiTH-R-2408 – http://www.fs.isy.liu.se/Publications/.

Ylva Nilsson and Lars Eriksson. A new formulation of multi-zone combustion engine models. In *Karlsruhe, Germany, IFAC Workshop: Advances in Automotive Control*, 2001.

Ylva Nilsson and Lars Eriksson. Detecting TDC position using symmetry and other methods. *SAE Technical Paper Series No. 2004-01-1458*, 2004.

Ylva Nilsson and Erik Frisk. Detecting knock in spark ignited engines. In *16:th IFAC World Congress in Prag*, July 2005.

Ylva Nilsson, Lars Eriksson, and Martin Gunnarsson. A model for fuel optimal control of a spark-ignited variable compression engine. *SAE Technical Paper Series No. 2006-01-0399*, 2006a.

Ylva Nilsson, Lars Eriksson, and Martin Gunnarsson. Modelling for fuel optimal control of SI VCR engines. In *Proceedings of New Trends in Engine Control, Simulation and Modelling*, IFP, Rueil-Malmasison, France, 2006b.

Ylva Nilsson, Lars Eriksson, and Martin Gunnarsson. Torque modelling for optimising fuel economy in variable compression engines. *International Journal of Modelling, Identification and Control (IJMIC)*, 3(3), 2008.

Toru Noda, Kazuya Hasegawa, Masaaki Kubo, and Teruyuki Itoh. Development of transient knock prediction technique by using a zero-dimensional knocking simulation with chemical kinetics. *SAE Technical Paper Series No. 2004-01-0618*, 2004.

Per Öberg and Lars Eriksson. Control oriented modeling of the gas exchange process in variable cam timing engines. In *SAE Technical Paper Series No. 2006-01-0660*, 2006a.

Per Öberg and Lars Eriksson. Control oriented gas exchange models for CVCP engines and their transient sensitivity. *Oil & Gas Science and Technology - Rev. IFP*, New Trends on Engine Control, Simulation and Modelling, 2007.

Per Öberg and Lars Eriksson. Control oriented gas exchange models for CVCP engines and their transient sensitivity. In *Proceedings of New Trends in Engine Control, Simulation and Modelling*, IFP, Rueil-Malmasison, France, 2006b.

K. J. Patton, R. G. Nitschke, and J. B. Heywood. Development and evaluation of a friction model for spark-ignition engines. *SAE Technical Paper Series No. 890836*, 1989.

J. I. Ramos. *Internal Combustion Engine Modeling*. Number ISBN 0-89116-157-0. Hemisphere Publishing Corporation, 1989.

F. Reif. *Fundamentals of statistical and thermal physics*. McGraw-Hill series in fundamentals of physics. McGraw-Hill, 1965. ISBN 07-051800-9.

Martyn Roberts. Benefits and challenges of variable compression ratio. *SAE Technical Paper Series No. 2003-01-0398*, 2003.

SAAB Automobile AB. Nytt, unikt motorkoncept ger ökad prestanda och lägre bränsleförbrukning: SAAB variable compression engine. *SAAB Automobile AB Information 00/02*, 29 February 2000.

Bahman Samimy and Giorgio Rizzoni. Engine knock analysis and detection using time-frequency analysis. *SAE Technical Paper Series No. 960618*, 1996.

K. Sawamoto, Y. Kawamura, T. Kita, and K. Matsushita. Individual cylinder knock control by detecting cylinder pressure. *SAE Technical Paper Series No. 871911*, 1987.

Patric Soltic. *Part-Load Optimized SI Engine Systems*. PhD thesis, Swiss federal Institute of technology in Zürich, November 2000.

Richard E. Sonntag, Claus Borgnakke, and Gordon J. Van Wylen. *Fundamentals of Thermodynamics*. Number ISBN 0-471-18361-X. John Wiley & Sons, 5 edition, 1998.

Hakan Serhan Soyhan, Per Amnéus, Terese Løvas, Daniel Nilsson, Peter Maigaard, Fabian Mauss, and Cem Sorusbay. Automatic reduction of detailed chemical reaction mechanisms for autoignition under si engine conditions. *SAE 2000 Transactions, Journal of Fuels and Lubricants*, 109:1435–1444, 2000.

M. Stöckli. Reibleistung von 4-Takt Verbrennugnsmotoren. Technical report, Internal report of the Laboratory of Internal Combustion Engines, Swiss Federal Institute of Technology, Zürich, 1989.

R. Stone. *Introduction to Internal Combustion Engines*. SAE International, third edition, 1999. ISBN 0-7680-0495-0.

G. Strang and T. Nguyen. *Wavelets and Filter Banks*. Wellesley MA: Wellesley-Cambridge Press, 1996.

Stephen R. Turns. *An Introduction to Combustion – Concepts and Applications*. Number ISBN 0-07-114783-7 in Mechanical Engineering Series. McGraw Hill, second edition, 2000.

T. H. Valtadoros, V. W. Wong, and J. B. Heywood. Engine knock characteristics at the audible level. *SAE Technical Paper Series No. 910567*, 1991.

I. Vibe. Halbempirische formel für die verbrennungsgesschwidigkeit. *Verlag der Akademie der Wissenschaften der UdSSR – Moscow*, 1967.

R. Worret, S. Bernhardt, F. Schwarz, and U. Spicher. Application of different cylinder pressure based knock detection methods in spark ignition engines. *SAE Technical Paper Series No. 2002-01-1668*, 2002.

Andy D. B. Yates, André Swarts, and Carl L. Viljoen. Correlating auto-ignition delays and knock-limited spark advance data for different types of fuel. *SAE Technical Paper Series No. 2005-01-2083*, 2005.

Linköpings Studies in Science and Technology
Department of Electrical Engineering
Dissertations, Vehicular Systems

No. 7   *Fault Isolation in Distributed Embedded Systems*
        Jonas Biteus, Disseration No. 1074, 2007

No. 6   *Design and Analysis of Diagnosis Systems Using Structural Mehods*
        Mattias Krysander, Dissertation No. 1033, 2006

No. 5   *Air charge Estimation in Turbocharged Spark Ignition Engines*
        Per Andersson, Dissertation No. 989, 2005

No. 4   *Residual Generation for Fault Diagnosis*
        Erik Frisk, Dissertation No. 716, 2001

No. 3   *Model Based Fault Diagnosis: Methods, Theory, and Automotive Engine Applications*, Mattias Nyberg, Disseration No. 591, 1999

No. 2   *Spark Advance Modeling and Control*
        Lars Eriksson, Dissertation No 580, 1999

No. 1   *Driveline Modeling and Control*
        Magnus Pettersson, Dissertation No. 484, 1997